Magnetoresistive Sensors for Industrial Positioning Applications

Guilherme Afonso Custódio Brites

Thesis to obtain the Master of Science Degree in

Engineering Physics

Supervisor(s): Prof. Susana Isabel Pinheiro Cardoso de Freitas

Examination Committee

Chairperson: Prof. Carlos Manuel Dos Santos Rodrigues da Cruz
Supervisor: Prof. Susana Isabel Pinheiro Cardoso de Freitas
Member of the Committee: Dr. Rita Joana dos Santos Macedo

October 2021

À minha família...

Acknowledgments

Agradeço em primeiro lugar à minha orientadora de dissertação, Professora Susana Cardoso de Freitas. Agradeço não só a permanente disponibilidade e ajuda durante a elaboração da dissertação, mas também todo o conhecimento que me tem vindo a transmitir durante o meu percurso no Mestrado e que despertou o meu interesse nesta área. Agradeço também ao Instituto Superior Técnico, e em particular a todos os professores que acompanharam o meu percurso até aqui.

Um grande obrigado a todos os colegas e técnicos do INESC-MN, por toda a ajuda que me deram durante a elaboração da dissertação e por todo o tempo que disponibilizaram. Um agradecimento especial à Catarina Janeiro por toda a ajuda durante o processo de fabricação, ao Pedro Araújo por toda a ajuda e partilha de conhecimento sobre sensores AMR e não só, e à Sofia Abrunhosa por estar sempre disponível a resolver qualquer dúvida ou questão e ajudar em tudo o que fosse preciso.

Um muito obrigado especial à Joana Miguel, pelo apoio sempre presente, dedicação incondicional e paciência inesgotável.

Por último, agradeço à minha família, à minha mãe Maria do Céu, ao meu pai Jorge, e aos meus irmãos Vasco e Henrique, por toda a ajuda, paciência e confiança, e por todos os conselhos que me guiaram pelos melhores caminhos até aqui. Obrigado!

Resumo

Em muitas indústrias diferentes existe hoje em dia uma grande procura competitiva por sistemas de posicionamento de tamanho e custo reduzido, capazes de funcionar em condições adversas, ainda assim com resultados precisos. Sensores de Magnetoresistência Anisotrópica (AMR) fornecem uma solução de baixo custo e consumo energético, sendo usados em encoders lineares com precisão de μm. Estes sensores são facilmente produzidos em massa e podem ser utilizados em diversas aplicações, sendo capazes de funcionar em ambientes sujos, ao contrário dos encoders ópticos.

Para estudar a utilização dos sensores AMR em aplicações industriais de posicionamento, foram fabricados sensores no INESC-MN, utilizando dois materiais diferentes para buffer, Ta e NiFeCr, sendo o núcleo do sensor um filme fino de Permalloy (NiFe). Foi estudado o efeito de annealing nas propriedades estruturais e magnéticas dos sensores, com annealing feito a $350°$C. O annealing teve um efeito total, estruturalmente, ao final de uma hora, e melhorias no rácio de AMR também foram verificadas, tendo-se obtido valores até 3.04%, em sensores fabricados com um buffer de NiFeCr.

Os sensores funcionam em pontes Wheatstone completas, fornecendo sinais fortes o suficiente para não necessitarem de amplificação, com amplitudes até $40mV$. Um setup de scanning foi modificado no INESC-MN, com a adição de uma placa de aquisição com a eletrónica adequada para medir o sinal à saída das pontes. Com o setup implementado é possível identificar problemas comuns como a desigualdade e desvios das pontes, tornando-o uma ferramenta importante para determinar a qualidade dos sensores.

Palavras-chave: Magnetoresistência Anisotrópica, Sensores AMR, Pontes de Wheatstone, Microfabricação, Encoders Lineares

Abstract

Across many different industries there is nowadays a very large competitive demand for positioning systems with reduced size and cost, that can operate in harsh conditions, while still providing accurate results. Anisotropic Magnetoresistive (AMR) sensors provide a simple, low cost and low power consumption solution, being used in linear encoders accuracy down to the μm. These sensors are easily mass produced and can be used in a wide range of applications, being able to function in dirty environments, unlike their optical counterparts.

To study the use of AMR sensors in industrial positioning applications, sensors were fabricated at INESC-MN, using two different buffer materials, Ta and NiFeCr, with the core of the sensor being a thin film of Permalloy (NiFe). The effect of annealing on the structural and magnetic properties of the sensors was studied, with annealing done at $350°$C. The annealing has its full effect, structurally, after one hour of annealing, and improvements in AMR were also verified, with AMR ratios up to 3.04%, on sensors fabricated with a NiFeCr buffer.

The sensors function in full Wheatstone bridges, providing large signals that require no amplification, with amplitudes up to the $40mV$. A scanning setup was modified at INESC-MN, with the addition of a custom acquisition board with the proper electronics in place to measure the full bridge outputs. With the implemented scanner setup, it is possible to identify common issues such as bridge mismatches and offsets, making it an important tool for determining the quality of the produced sensors.

Keywords: Anisotropic Magnetoresistance, AMR Sensors, Wheatstone Bridges, Microfabrication, Linear Encoders

Contents

Acknowledgments . . . v
Resumo . . . vii
Abstract . . . ix
List of Tables . . . xv
List of Figures . . . xvii
Nomenclature . . . xxi

1 Introduction **1**
1.1 Motivation . . . 1
1.2 State of the Art . . . 2
1.2.1 Magnetic sensors . . . 2
1.2.2 Magnetic encoders . . . 2
1.3 Objectives and Deliverables . . . 3
1.4 Dissertation Outline . . . 4

2 Theoretical Background **5**
2.1 Ferromagnetic Materials . . . 5
2.1.1 Ferromagnetism . . . 5
2.1.2 Ferromagnetic hysteresis loop . . . 5
2.1.3 Magnetic anisotropy . . . 6
2.2 Anisotropic Magnetoresistance . . . 7
2.3 Magnetic scale . . . 10
2.4 AMR sensors for positioning . . . 14
2.4.1 Materials . . . 14
2.4.2 Geometry . . . 14
2.4.3 Configuration . . . 15
2.5 Incremental Linear Encoders . . . 17

3 Sensor fabrication techniques and characterization methods **19**
3.1 Fabrication . . . 19
3.1.1 Ion Beam Deposition and Ion Beam Milling . . . 19
3.1.2 Sputtering Deposition and Etching . . . 20

3.1.3 Reactive Ion Etching . . . 21
3.1.4 Lithography . . . 21
3.1.5 Magnetic Annealing . . . 24
3.2 Characterization . . . 25
3.2.1 X-ray Diffractometry . . . 25
3.2.2 Transfer Curve . . . 26
3.2.3 Scanner Performance . . . 30

4 Implementation **37**
4.1 Fabricated Samples . . . 37
4.1.1 Unpatterned Samples . . . 37
4.1.2 Patterned Samples . . . 37
4.2 Fabrication Process . . . 38
4.2.1 Sensor Deposition - Ion Beam Deposition . . . 38
4.2.2 Sensor Definition - Lithography (DWL) . . . 39
4.2.3 Material Removal (Sensor) - Ion Beam Milling . . . 40
4.2.4 Passivation . . . 41
4.2.5 Vias Definition - Lithography (DWL) . . . 41
4.2.6 Vias Opening - Reactive Ion Etching . . . 42
4.2.7 Contact Definition - Lithography (DWL) . . . 42
4.2.8 Contact Deposition - Metallization . . . 43
4.2.9 Material Removal (Contacts) - Lift-off . . . 43
4.2.10 Passivation . . . 44
4.2.11 Pads Definition - Lithography . . . 45
4.2.12 Pads Opening - Reactive Ion Etching . . . 45
4.2.13 Magnetic Annealing - Optional . . . 46
4.3 Possible Issues - DWL vs Hard Mask: Uniformity . . . 46

5 Results and analysis **49**
5.1 X-Ray diffraction . . . 49
5.1.1 Diffraction peaks . . . 50
5.1.2 Grain size . . . 53
5.1.3 Inter-planar distance . . . 54
5.1.4 Summary . . . 54
5.2 Transfer Curves . . . 55
5.2.1 Manual Measurement Setup . . . 55
5.3 DWL vs Hard Mask - Uniformity . . . 61
5.4 Positioning . . . 63

6 Conclusions **75**

6.1 Achievements 75

6.2 Future Work 76

Bibliography **77**

A Process Runsheet **79**

A.1 Runsheet 79

B Acquisition Board **85**

B.1 PCB and switch/jumper combination table 85

List of Tables

1.1 Summary of different magnetic and magnetoresistive sensors and their main characteristics. Adapted from [2], page 517. 2

3.1 Value of components used in the electrical simulation. 33

4.1 Composition of the layers of the different unpatterned test samples. 37

4.2 Composition of the layers of the different patterned test samples. 38

4.3 Parameters of the magnetic annealing. 38

5.1 Duration of the annealings for the unpatterned samples. 50

5.2 X-Ray diffraction results of samples Ta(50), NiFeCr(50), NiFeCr(100) and NiFeCr(150). . 55

5.3 Parameters used for the 140Oe Setup transfer curve measurements for samples Ta(50), NiFeCr(50), NiFeCr(100), NiFeCr(150). 55

5.4 Transfer curve results of samples Ta(50), NiFeCr(50), NiFeCr(100) and NiFeCr(150). . . . 56

5.5 Transfer curve results of samples Ta(50), NiFeCr(50), NiFeCr(100) and NiFeCr(150). . . . 58

5.6 Transfer curve results of samples Ta(50), NiFeCr(50), NiFeCr(100) and NiFeCr(150). . . . 59

5.7 Parameters used in the auto-prober setup transfer curve measurements for the 6 inch wafers. 62

5.8 Parameters used in the auto-prober setup transfer curve measurements for the 6 inch wafers. 62

5.9 Equivalent resistance values, for the devices from samples Ta(50), NiFeCr(50), Ta(30)+NiFeCr(300). 67

5.10 Average values of period, phase and phase difference of the positioning error, for the devices from samples Ta(50), NiFeCr(50) 70

List of Figures

1.1 Representation of magnetic scales, for incremental and absolute positioning. From [1, 9]. 3

2.1 Generic magnetization response to an external magnetic field, along the field's direction. . 6
2.2 Graphical representation of the magnetization's inversion due to an applied external magnetic field. 8
2.3 Graphical representation of relevant parameters for AMR effect calculations. 8
2.4 Example transfer curves for an AMR sensor. 10
2.5 Representation of the directions for the two dimensional model. 11
2.6 Geometry for the calculation of the magnetic field generated by a magnetic scale. 11
2.7 Magnetic field components generated by a generic magnetic scale. 12
2.8 Direction of the magnetic field generated by the magnetic scale. 13
2.9 Vectorial plot of the magnetic field generated by a magnetic scale. 13
2.10 Example of meander structure of AMR sensors. 14
2.11 Schematic representation of a strip of the AMR meander. 15
2.12 Full bridge with four varying components. 15
2.13 Two full bridges with four varying components each, with a shared bias. 16
2.14 Device and sensor placement over a magnetic scale. 17
2.15 Compact arrangement of AMR sensors in a linear positioning device with one full bridge. 18
2.16 Compact arrangement of AMR sensors in a linear positioning device with two full bridges. 18

3.1 Schematic representation of an IBD/IBM system in Z configuration. 20
3.2 Schematic representation of a sputtering system in a vertical configuration. 21
3.3 Schematic representation of the photo-resist coating process. 22
3.4 Schematic representation of the DWL and Hard mask exposure processes. 23
3.5 Schematic representation of the etching and lift-off lithography processes. 23
3.6 Representation of the non inverted and inverted masks. The regions highlighted in red contain the resist. Adapted from [21]. 24
3.7 Example of a magnetic annealing cycle. 24
3.8 X-ray diffraction principle. 25
3.9 Picture of the diffractometer. 26
3.10 Representation of the key properties extracted from the transfer curve. 28

3.11 Manual measurement setup used to measure transfer curves. 29
3.12 Auto-prober setup used to measure transfer curves. 30
3.13 Electric circuit equivalent to the two probe measurement. 30
3.14 Setup for scanner tests. 31
3.15 Electric circuit of the differential amplifier. 32
3.16 Electric circuit used in the simulation. 34
3.17 Results of the simulation of the differential amplifier circuit applied to the bridge outputs. . 34
3.18 Simulation results evidencing the match between the signals V_{outx} and $V_{x+} - V_{x-}$. 35
3.19 Acquisition board for the scanner setup. 35
3.20 Example of polar plots of the bridge outputs and identifiable issues. a) Offset error. b) Amplitude mismatch. c) Phase mismatch. d) Signal-shape error. 36

4.1 Schematic of the fabricated sample after the sensor deposition. 39
4.2 Schematic of the fabricated sample after the sensor definition lithography. 39
4.3 Example of an alignment mark used in lithographies after the first. 40
4.4 Schematic of the fabricated sample after the sensor level etching. 40
4.5 Picture of one of the test samples after milling. 41
4.6 Schematic of the fabricated sample after the first passivation. 41
4.7 Schematic of the fabricated sample after the vias definition lithography. 42
4.8 Schematic of the fabricated sample after the vias opening by RIE. 42
4.9 Picture of one of the test samples after RIE for vias opening. 42
4.10 Schematic of the fabricated sample after the contact definition lithography. 43
4.11 Schematic of the fabricated sample after the contact deposition. 43
4.12 Schematic of the fabricated sample after the contact lift-off. 44
4.13 Picture of one of the test samples after contact lift-off. 44
4.14 Schematic of the fabricated sample after the final passivation. 45
4.15 Picture of one of the test samples after the second passivation. 45
4.16 Schematic of the fabricated sample after the pads opening lithography. 45
4.17 Schematic of the fabricated sample after the pads opening RIE. 46
4.18 Picture of one of the test samples after RIE for pad opening. 46
4.19 Example of a sensor definition flaw resulting from the DWL lithography step. 47

5.1 Representation of the *fcc* structure. 49
5.2 Evolution of X-ray diffraction peaks of sample Ta(50) with cumulative annealing time. . . . 50
5.3 Evolution of X-ray diffraction peaks of sample NiFeCr(50) with cumulative annealing time. 51
5.4 Evolution of X-ray diffraction peaks of sample NiFeCr(100) with cumulative annealing time. 51
5.5 Evolution of X-ray diffraction peaks of sample NiFeCr(150) with cumulative annealing time. 52
5.6 Evolution of the peaks' positions and FWHM with cumulative annealing time, for all samples. 52
5.7 Evolution of the grain size of all samples with cumulative annealing time. 53
5.8 Evolution of the inter-planar distance of all samples with cumulative annealing time. . . . 54

5.9 Transfer curves of samples Ta(50), NiFeCr(50), NiFeCr(100) and NiFeCr(150) with no annealing. 56
5.10 Transfer curves of the four samples before and after annealing at 350°C for 2 hours. . . . 57
5.11 Transfer curves of samples Ta(50), NiFeCr(50), NiFeCr(100) and NiFeCr(150) with annealing. 58
5.12 Transfer curves of all samples with annealing with annealing. 59
5.13 MR measurement results. 60
5.14 R_{min} measurement results. 60
5.15 H_c measurement results. 61
5.16 FWHM measurement results. 61
5.17 Histograms of R_{min} and MR measurements on 6" wafers, using two different lithography techniques for the definition of the sensor level. 63
5.18 Polar plots ($Bridge2\, vs\, Bridge1$) of sample Ta(50) at different flying heights. 64
5.19 Polar plots ($Bridge2\, vs\, Bridge1$) of sample NiFeCr(50) at different flying heights. 64
5.20 Polar plots ($Bridge2\, vs\, Bridge1$) of sample Ta(30)+NiFeCr(300) at different flying heights. 65
5.21 Evolution of the offset of both bridges of each device with increasing flying height. 66
5.22 Equivalent resistance measured between V_{out1+} and GND. 66
5.23 Evolution of the phase difference with increasing flying height for the three tested samples. 67
5.24 Amplitudes of both bridges of the each device, as function of the flying height. 68
5.25 Amplitude difference between bridges of the same device, as function of the flying height. 69
5.26 Positioning error using devices from sample Ta(50) at the first three flying heights, $d = 0.2mm$, $d = 0.4mm$, $d = 0.6mm$. 69
5.27 Polar plot of measurements with the devices from samples Ta(50) and NiFeCr(50) with maximum positive and negative error zones highlighted. 71
5.28 Position calculated using equation 2.13 and the bridges' outputs, for the three tested samples, at flying heights $d = 0.2mm$ (a) and $d = 0.2mm$ (b). 72
5.29 Evolution of the normalized amplitude with increasing flying height. 73
5.30 Evolution of the maximum positive and negative positioning errors with increasing flying height. 74

Nomenclature

Greek symbols

α Angle of external magnetic field.

θ Angle of magnetization.

Roman symbols

H_c Coercivity.

M_r Magnetic remanence.

M_s Spontaneous magnetization.

M_sat Saturation magnetization.

MR Magnetoresistance ratio.

Subscripts

$+$ Positive terminal.

$-$ Negative terminal.

$\|$ Parallel component.

$\perp$ Perpendicular.

i, j, k Computational indexes.

in Input terminal.

n Normal component.

out Output terminal.

t Tangencial component.

x, y, z Cartesian components.

Chapter 1

Introduction

Almost every industry of the present day requires accurate solutions for metrology and positioning. There are several techniques that can be used, using different devices working under different physical principles, each having their own strengths and weaknesses. They aim, however, towards the same goal: accurate and reliable positioning with high resolution. The suitability of each device will vary on the requirements of the task (type of environment, minimum resolution, among others), but this also shows versatility is of some value, meaning the device can be used in a widespread range of situations. The focus of this thesis will be the study of magnetoresistive sensors for industrial positioning applications.

1.1 Motivation

There is a very large competitive demand for devices that have reduced size and cost and that can operate in harsh conditions, while still providing accurate results. One of the most commonly used solutions is optical devices, which guarantee high resolution and accuracy, but require bigger and more expensive equipment to operate in dirty environments, for example. Magnetoresistive (MR) devices have a clear advantage over optical devices in this sense [1]. These MR devices can be used in encoding and can be produced with micrometric (and even nanometric) sizes. They are easily mass produced with low costs and are highly sensitive to weak magnetic fields. The operation of these sensors is also unaffected by the presence of water, oils, or dust, unlike the optical devices.

Anisotropic magnetoresistive (AMR) sensors have a very simple structure, made from ferromagnetic materials, such as iron (Fe), nickel (Ni), or more commonly of alloys composed of these metals, such as Permalloy ($Ni_{0.8}Fe_{0.2}$), resulting in low production costs. AMR sensors have a very low power consumption and offer sensitivity to magnetic fields down to the nT [2][3]. Paired with a magnetic tape these sensors can be used for positioning applications in any industry, providing a low cost, yet accurate and reliable solution, offering spatial resolution down to the μm [1].

1.2 State of the Art

The applications of magnetic and magnetoresistive sensors are very broad and they are present in many industries. For example, vehicle detection or measuring rotation speeds and angles, positions or lengths and even electrical currents. These measurements using magnetoresistive sensors, however, are generally indirect. The sensors themselves only give information about surrounding magnetic fields, which then needs to be processed to obtain the relevant parameters [4].

Driving this field forward is the necessity to reduce the size, cost and power consumption, without hindering, or sometimes even increasing, the sensitivity, accuracy, resolution and reliability of measurements. Two other important aspects are to ensure the devices maintain proper functioning under harsh conditions and that they are compatible with common electronic equipment or other devices. Magnetoresistive sensors nowadays deliver in both these aspects.

1.2.1 Magnetic sensors

These sensors have evolved greatly in the past decades due to the progress in micro and nanofabrication, since the devices are comprised of single or multi-layer thin film structures. The most simple ones, with a single magnetic layer are the Planar Hall Effect (PHE) sensors and the Anisotropic Magnetoresistive (AMR) sensors, but there are more elaborate devices with multi-layer structures of more complex and diverse materials, making use of Giant Magnetoresistance (GMR) and Tunneling Magnetoresistance (TMR) effects. Nonetheless, there is still room for improvement and optimization of the sensors to each specific application. An ideal sensor does not exist and depending on the application the optimal sensor may differ. In table 1.1, below, some properties of various types of sensors are presented.

Magnetic Sensor	**Principle**	**Detects**	**Field(T)**	**Noise/**$\sqrt{Hz}$
Search coil	Faraday's Law	$d\Phi/dt$	$10^{-10} - 10^{2}$	100nT
Fluxgate	Saturable ferromagnet	$d\Phi/dt$	$10^{-10} - 10^{-3}$	10pT
PHE	Anomalous Hall Effect	H	$10^{-9} - 10^{-3}$	10nT
AMR	Spin-orbit scattering	H	$10^{-9} - 10^{-3}$	10nT
GMR	Spin accumulation	H	$10^{-9} - 10^{-3}$	10nT
TMR	Tunneling	H	$10^{-9} - 10^{-3}$	1nT
SQUID	Flux quantization	Φ	$10^{-15} - 10^{-2}$	1fT

Table 1.1: Summary of different magnetic and magnetoresistive sensors and their main characteristics. Adapted from [2], page 517.

Some of the largest AMR coefficients recorded are around 6%, in Ni_xFe_{1-x} alloys [5].

1.2.2 Magnetic encoders

Magnetic encoders are devices capable of converting magnetic measurements into measurements of position, angle, speed and distance; typically composed of two elements: a magnetic sensor and a magnetic scale [6]. The scale will have a signature magnetic code which the sensor will measure to generate the required information. Encoders come in various forms, making them a flexible solution,

suitable to many different problems. The encoders can be linear, ring shaped, inserted in or around a shaft or axis, and they can also be found in integrated circuits [7]. This type of solution can also be found in gears, for rotation speed measurements or gear tooth proximity.

Linear encoders can be used for positioning and can work in two different ways: they can be incremental or absolute [8]. Incremental linear positioning is the simplest form, being advantageous for it, yet having some disadvantages of its own. An incremental scale has a simple alternating magnetization code (more information on the scales is given in section 2.3). This produces a simple sinusoidal magnetic field for the sensor to detect, but as the name indicates, it can only be used to measure an increment or change in the position. If, for example, there is a power outage or something that forces the system to shut down, once it reboots, the incremental encoder cannot give its absolute position, it must start from a new reference. And that is where the absolute encoder has an edge. The absolute encoder can be used to determine the position of the sensor (and thus the system it is attached to) at any time, even after a reboot of the system. This, however, requires a much more complex magnetic scale that produces a specific signature magnetic field which the sensor can detect to determine its absolute position [8]. These encoders can be found in industries such as agriculture, surveillance cameras, medicine, electric motors, robotics and green energy [7].

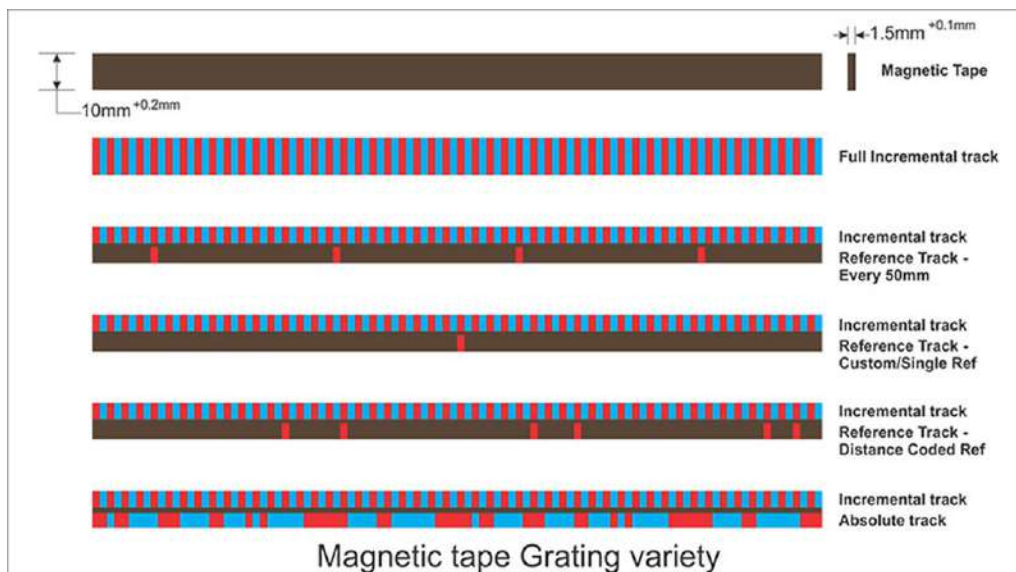

Figure 1.1: Representation of magnetic scales, for incremental and absolute positioning. From [1, 9].

1.3 Objectives and Deliverables

For this dissertation, AMR sensors will be explored to better suit specific industrial positioning applications, mainly for linear encoders. Two materials will be tested for the buffer layer of the sensor: Ta and NiFeCr, Ta being the baseline for comparison. Besides the influence of using a different material, different buffer thicknesses will be tested, as well as the consequence of magnetic annealing of the sensors. The magnetic response of the sensors will be characterized and later the performance on a linear positioning system will be tested, in an attempt to find a correlation between the magnetic properties and the

positioning specifications. The sensors were manufactured at INESC-MN, where a strong knowledge on fabrication and characterization of Magnetoresistive sensors in general served the purposes of this thesis perfectly. With the work done for this dissertation this knowledge will be furthered, regarding AMR sensors specifically, in terms of the use of NiFeCr as a buffer material, the effects of annealing, and with a characterization setup adapted specifically for positioning devices using these sensors, making it possible to evaluate their quality in this particular application.

1.4 Dissertation Outline

In chapter 2 ferromagnetic materials and their relevant properties are briefly explained, followed by the theoretical background of the anisotropic magnetoresistance effect in thin films. The properties of a magnetic scale are also explained. Joining the topics of ferromagnetic materials and the anisotropic magnetoresistive effect, the theory on AMR sensors for positioning is given as well. Finally, an explanation on how all of this information combined gives rise to the incremental linear encoder.
Chapter 3 gives insight on the fabrication techniques and characterization methods used during this dissertation, while chapter 4 describes how the fabrication techniques were implemented in order to make the test samples, which are also described in this chapter.
In chapter 5 the results of all the characterization and tests are presented, and the conclusions are given in chapter 6.

Chapter 2

Theoretical Background

This chapter is divided into three main sections, each explaining the theory behind the main aspects of the dissertation: ferromagnetic materials, physical principle of AMR, incremental linear encoder operation and sensor fabrication.

2.1 Ferromagnetic Materials

2.1.1 Ferromagnetism

In the absence of external magnetic fields, the magnetic dipoles of the atoms or molecules of a ferromagnetic material will spontaneously align in a random direction, due to a strong, long-range ordering of the magnetic moments [10]. Over small areas, these atoms or molecules will all align in the same direction, and these small areas are known as (magnetic) domains. The direction of the magnetization in these domains is such, that generally, the overall resulting magnetization is zero, in order to minimize the magnetostatic energy of the material [11].

When a external magnetic field is applied, the magnetic moments will try to align with the direction of the field, undoing the domains and thus the material acquires magnetization. If the magnetic field is strong enough, the magnetic moments in all the domains align with its direction and the material becomes fully magnetized in this direction [11].

However, it is not necessary that the magnetization is null in the absence of an external magnetic field. When this external field is removed, the material may retain some magnetization, along the direction of this field. This property varies between materials and it is known as magnetic remanence, M_r, with symbol σ.

2.1.2 Ferromagnetic hysteresis loop

The ferromagnetic hysteresis loop describes the response of the magnetization to the applied external magnetic field. It is nonlinear and irreversible [2]. In figure 2.1 a generic hysteresis loop is plotted,

$M(H)$, along with a schematic representation of the micromagnetic domains and with the relevant parameters that can be observed pointed out in the correct place.

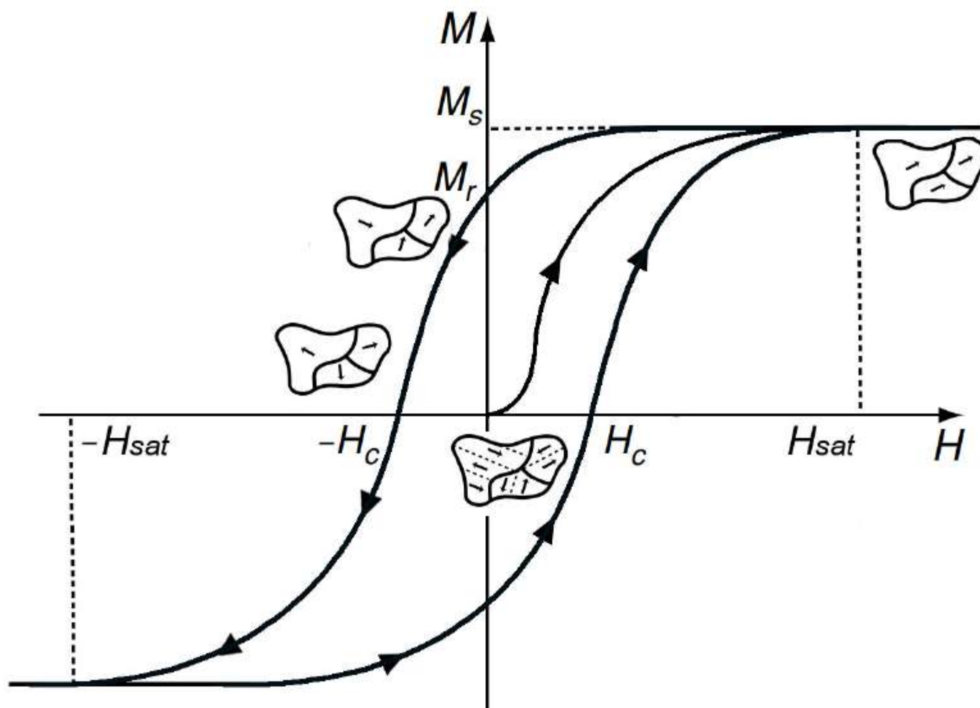

Figure 2.1: Generic magnetization response to an external magnetic field, along the field's direction. Relevant parameters are pointed out in the plot: coercivity, H_c, spontaneous magnetization M_s and magnetic remanence, M_r. A schematic representation of the micromagnetic domains in each stage of the curve can also be observed. Adapted from [2].

A magnetic field is applied to a sample in a certain direction, ranging from $H = 0$, to $H = H_{max}$, then to $H = -H_{max}$ and finally back to $H = H_{max}$, thus completing a full loop. With a sample in virgin state, starting from $H = 0$, the micromagnetic domains are arranged in order to minimize the magnetostatic energy of the sample, so there is no magnetization, $M = 0$. As the magnetic field's strength increases, the magnetization grows along its direction, because the domains are aligning with that direction.[2] At some point the magnetization will maximize, on what is known as the spontaneous (or saturation) magnetization, $M = M_s$. Decreasing the field back to zero gives us the magnetic remanence, $M = M_r$, of the material: the magnetization retained by the material once there no longer is an external magnetic field [12]. Lastly, the final property, the coercivity, H_c is defined as the magnetic field strength required to bring the magnetization back to zero $M = 0$. The process of magnetization is irreversible, although it is possible to demagnetize, just not following the same curve as when the sample goes from a virgin state to the magnetized state, hence the irreversibility of the process.

2.1.3 Magnetic anisotropy

An anisotropic material has properties that depend on direction. For this dissertation, the concern is magnetic anisotropy and its sources. The different types of anisotropy described below will give the

ferromagnetic material's energetically favorable/unfavorable axes for the magnetization to lay on, known as the easy and the hard axes. The easy axis is the preferential direction the magnetization will take in the absence of an external magnetic field. The hard axis is the direction that requires the most magnetostatic energy to align the magnetization of the material with. The different sources of anisotropy can work together, reinforcing these axes, or against each other, nullifying the effects [10] [11]. This tendency to align in a certain direction can be expressed in an energy density term, given as:

$$E = K_{eff} \sin^2 \theta \tag{2.1}$$

where K_{eff} is the effective anisotropy constant, and θ is the angle between the magnetization and the easy direction [12]. Thus, this energy is zero when the two are parallel, and maximum when they are perpendicular, i.e., when the magnetization is parallel to the hard axis. In result, the parameters that describe the magnetization process become functions of direction [10].

Magnetocrystalline anisotropy

This is an intrinsic property of the material, originating from a spin-orbit-lattice coupling, an interaction between the magnetic moments and the crystal-field present due to the crystalline phase of the material. This property implies that the magnetization process will differ if the field is applied along different crystallographic directions [2].

Shape or magnetostatic anisotropy

Shape anisotropy originates from the demagnetization field. After magnetizing a material, a magnetic field emerges within the material, which can be interpreted as a result of a distribution of free-poles in the material. This magnetic field always opposes the magnetization, hence the name. The distribution of the charges depends largely on the shape of the material, if it does not have the same length in every direction, the demagnetization field will also not be the same in every direction [2].

Induced anisotropy

Anisotropies can be induced in a material through several processes, such as a deposition under a magnetic field, annealing or applying uniaxial stress. These anisotropies are therefore not intrinsic to the materials, but rather a manipulation of the material properties [2].

AMR sensors typically make use of shape anisotropy, which is reinforced throughout the fabrication process in some steps, as will be made clear in chapter 3.

2.2 Anisotropic Magnetoresistance

The Anisotropic Magnetoresistance effect was first discovered in 1857 by Lord Kelvin, but it was not until the decade of 1960 that significant progress was made in developing and applying this discovery,

due to the progress of technology in fabrication of thin film devices [5, 13]. This effect has its origins in magnetotransport, more specifically in spin-orbit coupling, resulting from the difference in the s-d electron scattering cross section when the current direction is varied with respect to the orientation of the magnetically aligned atoms [11]. Briefly, the resistance of the material will vary, depending on the angle between the directions of electrical current and the magnetization. It is also known that the direction of the magnetization depends on the direction and strength of an applied external field. Since the resistance is then correlated with that external magnetic field, the term $magnetoresistive$ can be applied, which simply describes a material whose resistance is a function of an external magnetic field [14]:

$$R \equiv R(H_{ext}) \tag{2.2}$$

The magnitude of the magnetoresistive effect can be calculated using equation (2.3) [14]:

$$MR = \frac{R_{max} - R_{min}}{R_{min}} = \frac{\Delta R}{R_{min}} \tag{2.3}$$

A simple way to describe and understand the AMR effect is through the Stoner-Wohlfarth model. In figures 2.2 and 2.3, respectively, the change in the direction of the magnetization is shown, as well as all the relevant parameters for calculations of the AMR effect using this model.

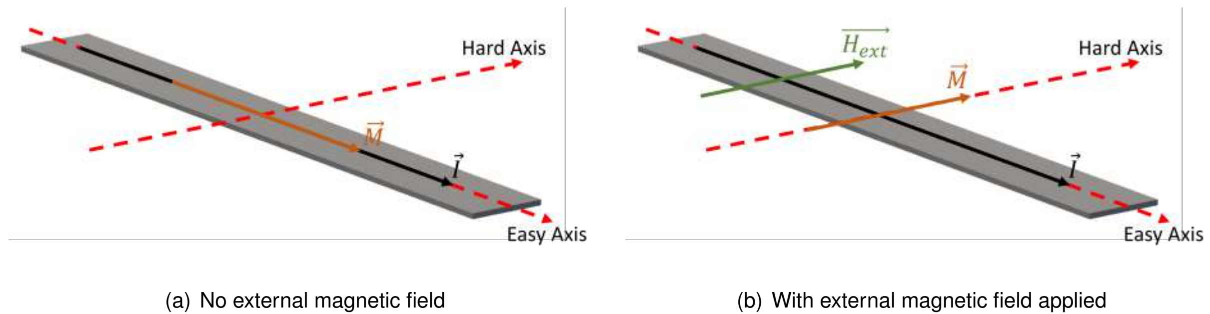

(a) No external magnetic field

(b) With external magnetic field applied

Figure 2.2: Graphical representation of the magnetization's inversion due to an applied external magnetic field.

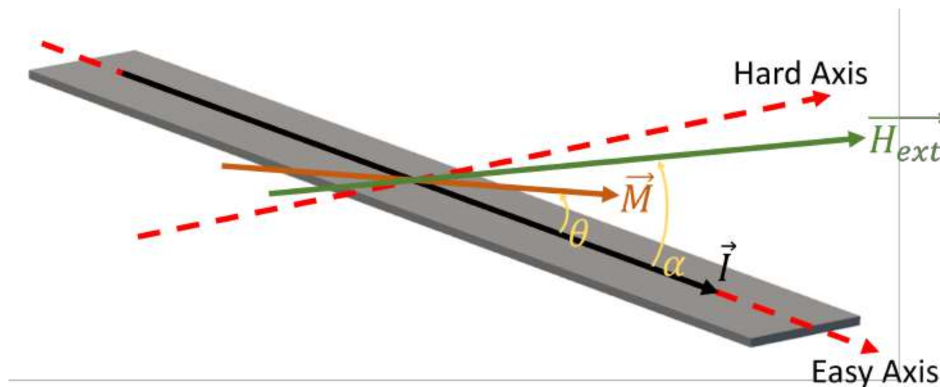

Figure 2.3: Graphical representation of relevant parameters for AMR effect calculations, in a generic magnetic volume. Notice the angles θ between M and the easy axis, and α between H and the easy axis.

A thin film of ferromagnetic material has anisotropies that give rise to an easy and hard magnetic axis, as explained in section 2.1.3. The easy axis is the direction the magnetization will favour when there is no external magnetic field and the hard axis is perpendicular to that axis. Usually, in thin films, and such is the case in AMR sensors, these axes are in the plane of the film, due to a strong shape anisotropy. The magnetization will favour the easy direction and the hard direction can be considered the sensitive direction, since applying a magnetic field parallel to the easy axis will yield no change in the device, because the magnetization will not change orientation. The resistivity of the device can be defined as a function of the angle θ between I and M as such:

$$\rho(\theta) = \rho_\perp + (\rho_\parallel - \rho_\perp)\cos^2\theta = \rho_\perp + \Delta\rho\cos^2\theta \tag{2.4}$$

Where $\rho_\perp = \rho(90°)$ and $\rho_\parallel = \rho(0°)$ [15]. The resistivity, and hence the device's resistance and output voltage, will have its maximum when $\theta = 0°$, when the magnetization and the electrical current are parallel. And so the minimum occurs when the magnetization and the electrical current are perpendicular, $\theta = 90°$. This can rewritten in terms of resistance:

$$R(\theta) = R_{min} + \Delta R\cos^2\theta \tag{2.5}$$

A solution can be derived for θ by minimizing the total magnetic energy of the layer:

$$E_T(\theta) = K_u sin^2\theta - \mu_0 M_s H_{ext} cos(\alpha - \theta) \tag{2.6}$$

Where K_u is the uniaxial anisotropy constant of the thin film, with which the anisotropy field can be written as $H_k = \frac{2K_u}{\mu_0 M_s}$ and $H_\parallel = H_{ext}\cos\alpha$, $H_\parallel = H_{ext}\sin\alpha$. If the field is strong enough to saturate the device, the magnetization will acquire the direction of the magnetic field. In such case, $\theta = \alpha$, making possible then to measure the direction of the magnetic field, in the plane of the sensor. In figure 2.4 the typical transfer curve is plotted in terms of resistance and MR ratio, R(H) and MR(H), with a magnetic field applied perpendicularly to the magnetic easy axis. The resistance is at a maximum when there is no magnetic field applied, meaning the electrical current is parallel to the easy axis of the sensor. The data for the curve was obtained at INESC-MN.

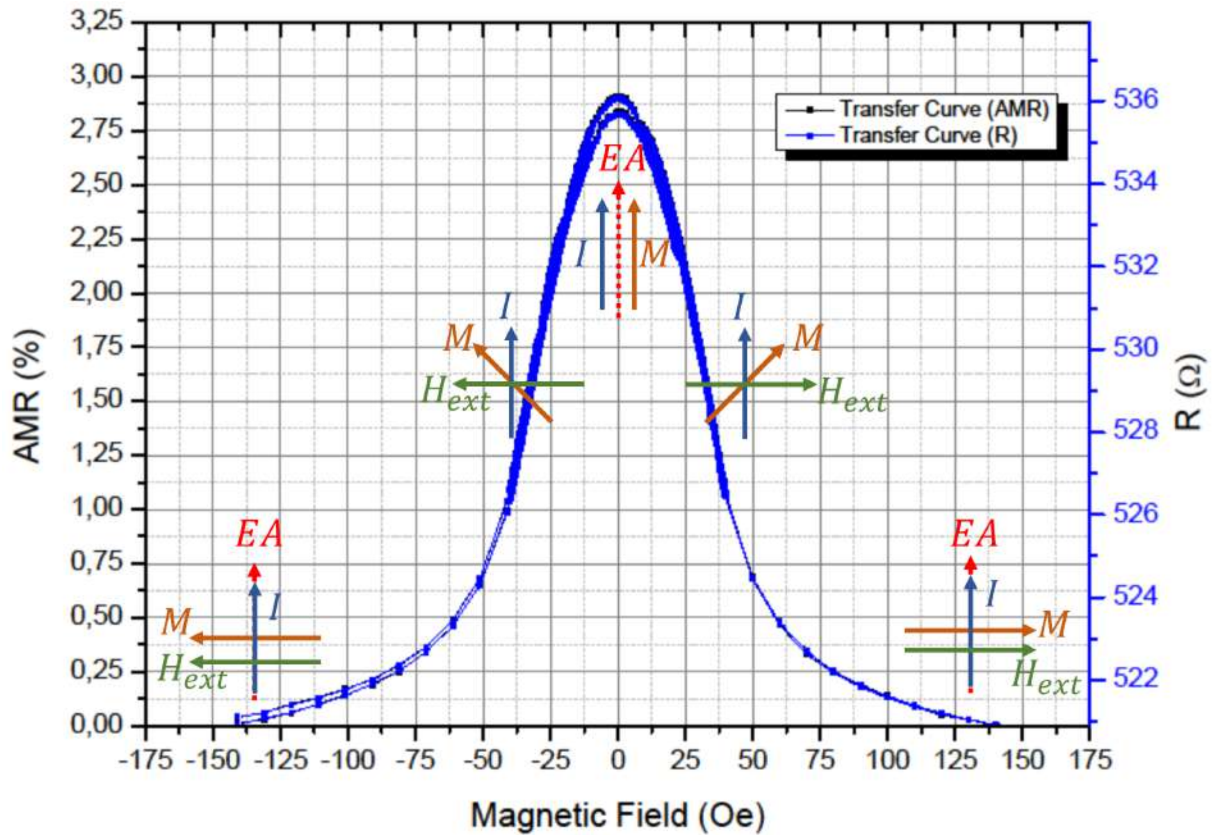

Figure 2.4: Example transfer curves for an AMR sensor. The relation between M and I is present at relevant states of the sensor. The magnetic field was applied perpendicular to the easy axis. The dashed red arrow represents the magnetic easy axis direction.

There are some disadvantages to these sensors, for example, the output of the sensor is independent of the direction of the field, $R(H) = R(-H)$. Furthermore, it is most useful for sensors to have a linear output. In the following sections (2.3,2.4 and 2.5) it is explained how these issues are addressed, in order to obtain a linear output for the positioning system.

2.3 Magnetic scale

A magnetic scale is simply a collection of magnetized pieces of ferromagnetic material with identical sizes. The material chosen for these scales is typically a hard ferromagnetic material. Usual characteristics of hard ferromagnets include high magnetic remanence and low susceptibility, making them suitable to be used in permanent magnets, which is what the magnetic scale requires. Each piece is referred to as a *bit*, since these scales can be interpreted as a binary code. The scales can either be magnetized in plane or out of plane, but in any case the magnetization of each bit will take one of only two directions, one of the directions will correspond to a 1 value for the bit and the other direction a 0. Figure 2.14 has an example of a simple alternating binary code in the form of a magnetic scale magnetized out of plane. The magnetized bits will create a magnetic field in their proximity, and with a magnetic sensor it is then possible to read these fields and obtain information such as the bit code itself or the position along a scale, which is the case in positioning applications.

However, to interpret what the sensor is detecting, an understanding of the magnetic fields created by the scales is required. For that, a fairly simple two dimensional model can be used. Referring to figure 2.14, the three directions are **x: cross-track**, **y: longitudinal direction**, **z: normal** [16].

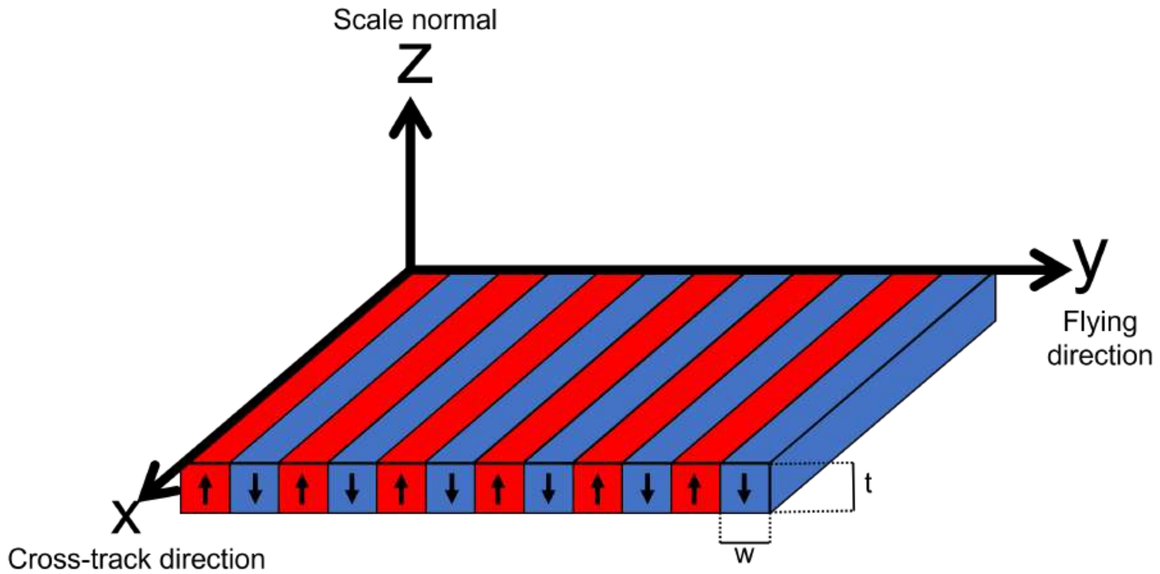

Figure 2.5: Representation of the directions for the two dimensional model. The thickness of the scale is t and the bit width is w.

This model assumes uniformity of the scale in the cross-track direction for each bit, and that the scale is much larger in this direction than the other two. The generated magnetic field will then have only two components, one normal to the scale, $H_n(y,z)$ and one tangential to the scale, $H_t(y,z)$, along the longitudinal direction, both independent of x since this is the cross-track direction. These two components can be calculated using equations (2.7) and (2.8), for each surface. The significance of r_1, r_2 and $\Delta\theta$ is clarified on figure 2.6 and σ is the magnetic remanence of the bit (M_r) [16].

$$H_n = -\frac{\sigma\Delta\theta}{2\pi} \tag{2.7}$$

$$H_t = -\frac{\sigma ln(r_1/r_2)}{2\pi} \tag{2.8}$$

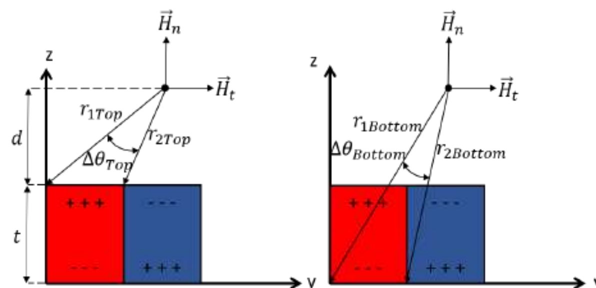

Figure 2.6: Geometry for the calculation of the magnetic field generated by a magnetic scale, using a two dimensional model.

To complete the calculation, the two surfaces contributing to the field of each bit had to be taken into account, the *top* and *bottom* surfaces, and for the whole magnetic scale the contributions of each bit needs to be summed, resulting in equations (2.9) and (2.10), considering the scale has N bits.

$$H_n \equiv H_z(y,z) = \sum_{i=0}^{N-1} -\frac{\sigma^i \Delta\theta^i_{top}}{2\pi} + \frac{\sigma^i \Delta\theta^i_{bottom}}{2\pi} \tag{2.9}$$

$$H_t \equiv H_y(y,z) = \sum_{i=0}^{N-1} -\frac{\sigma^i ln(\frac{r^i_{2top}}{r^i_{1top}})}{2\pi} + \frac{\sigma^i ln(\frac{r^i_{2bottom}}{r^i_{1bottom}})}{2\pi} \tag{2.10}$$

Where $\sigma^i = \pm\sigma$ is the magnetic remanence of the bit, according to the direction of the magnetization. If the magnetization is along z, $\sigma^i = +\sigma$, if it is along $-z$, $\sigma^i = -\sigma$.

Plotting equations 2.9 and 2.10 show the relevant properties of the magnetic field:

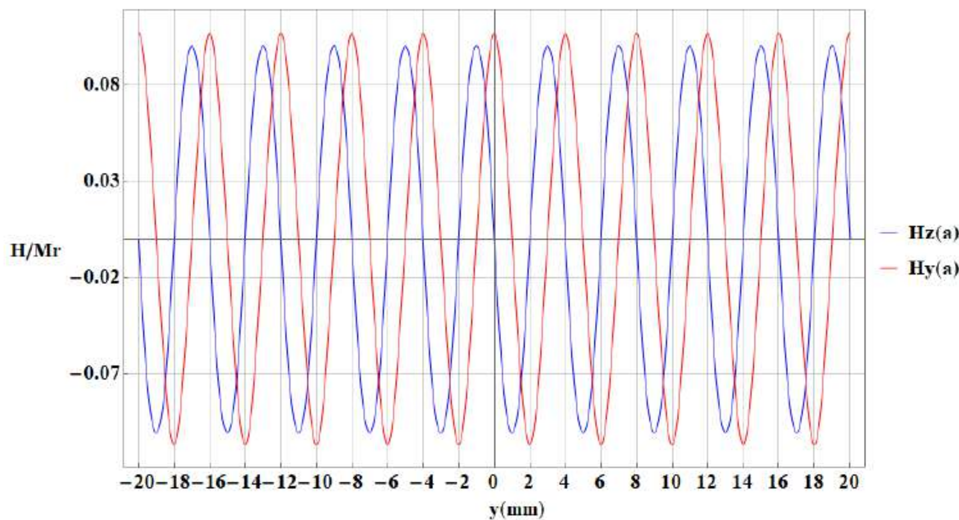

Figure 2.7: Magnetic field components generated by a generic magnetic scale, at $d = 1mm$ distance from the scale surface, using for calculations and bit width of $w = 2mm$ and scale thickness of $t = 1mm$. Origin at the center of the scale for y and surface of the scale for z.

The two components $H_z(y,z)$ and $H_y(y,z)$ are in quadrature, which means the magnetic field is effectively rotating periodically, $360°$. Figure 2.8 shows a plot of the angle of the direction of the magnetic field with the y axis, which can be seen to rotate counterclockwise when moving along the y direction over the scale. Taking the arctangent of $\frac{H_y}{H_z}$ gives the angle of the direction of the field with the y axis, which varies from $360°$ to $0°$, indicating it rotates counterclockwise, and it does so periodically, over two times the bit width, $2w$. Figure 2.9 shows the vectorial plot of the magnetic field, over 4 bits of the scale, where the arrows indicate the direction of the magnetic field along y and z.

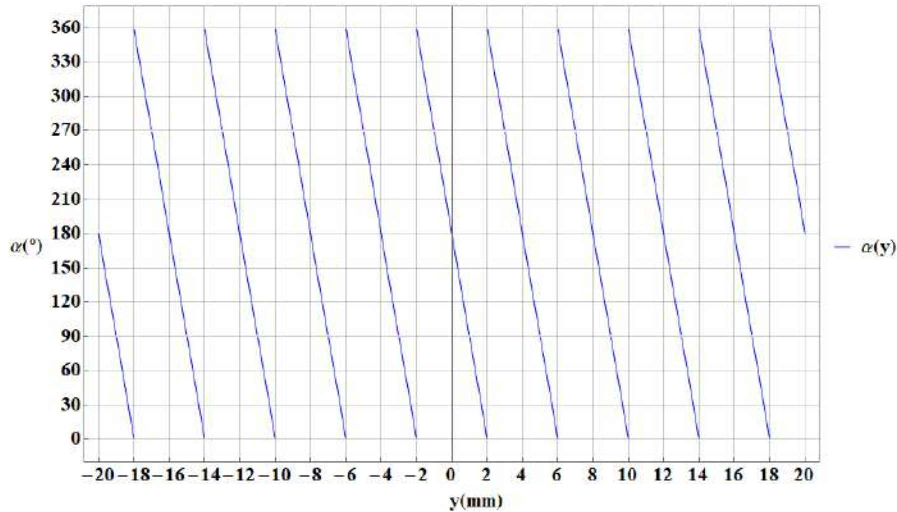

Figure 2.8: Direction of the magnetic field generated by a magnetic scale of $t = 1mm$ and $w = 2mm$, rotating counterclockwise starting from the y axis

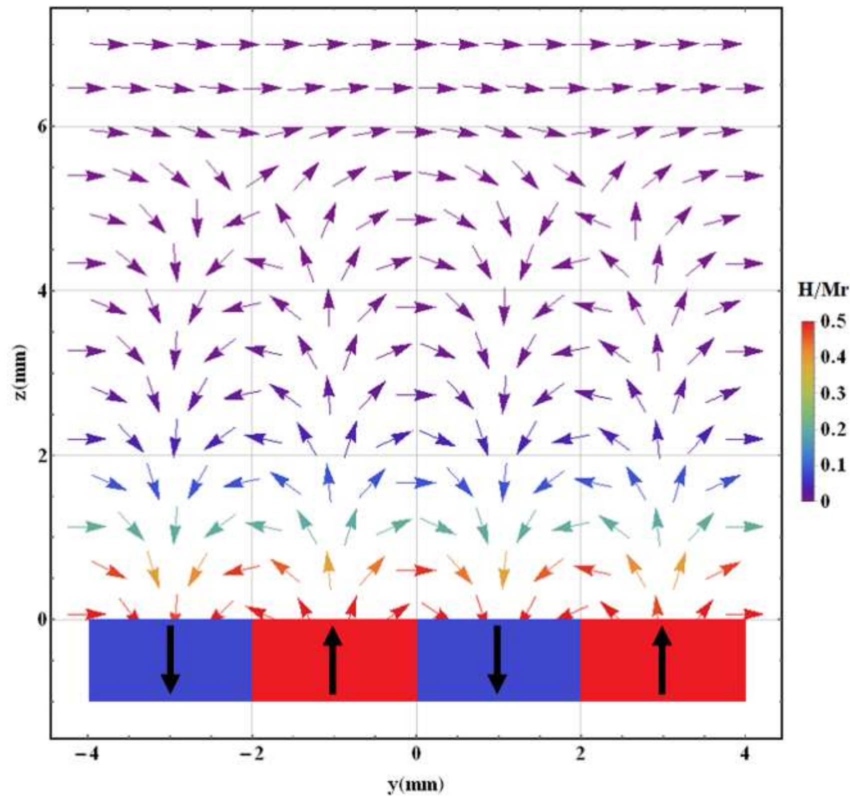

Figure 2.9: Vectorial plot of the magnetic field generated by a magnetic scale. The intensity of the field is given as H/M_r (unitless). In this example the bit width is given as $w = 2mm$ and the thickness of the scale $t = 1mm$.

The period of the rotation is exactly double the bit pitch of the scale. If the magnetic bits are stuck together, the pitch is the same as the bit width, so the spatial period of the direction of the field is given by double the bit width. In other words, the magnetic field rotates $180°$ between each bit, and $360°$ between consecutive bits with the same magnetization. This is the key property that is exploited in order to create the incremental linear encoder, which will be explained in further detail in section 2.5, since

the direction of the field changes linearly along the chosen flying direction. It is also noticeable that this desired shape of the field lines changes after a certain distance from the scale. Although obvious, it is also worth mentioning that the field strength decreases with increasing distance from the scale.

2.4 AMR sensors for positioning

2.4.1 Materials

For AMR sensors, the materials used are typically *soft* magnetic materials. Under this denomination fall materials with low coercivity, high susceptibility and low magnetic remanence. In such materials, the processes through which the magnetization changes (domain wall motion and domain magnetization rotation) occur when applying external magnetic fields of low intensity, meaning very low fields are required to saturate the material[10]. Low coercivity will be very important for positioning applications. One example of such a material is permalloy (Py), an alloy of nickel and iron, $Ni_{0.8}Fe_{0.2}$, which has an anisotropy constant of $K_1 \approx -1kJ.m^{-3}$, a typical value for soft magnetic materials.

2.4.2 Geometry

Geometry is a key factor in AMR sensors. In order to exploit shape anisotropy, the sensors are fabricated according to some rules. As is explained in section 2.1.3, to ensure an in-plane magnetization, the sensor must be a thin film. The easy axis is defined, again, through shape anisotropy: it will lie along the longest direction of the sensor. Therefore, the desired shape is a long and thin strip of material. However, one single strip of material does not provide enough sensing volume and has very low resistance, making it unsuitable for functioning as a sensor. To remedy that, a meander of strips is used, connected at alternate ends, as exemplified in figure 2.10, essentially creating a longer strip in a compact area [15] [17] .

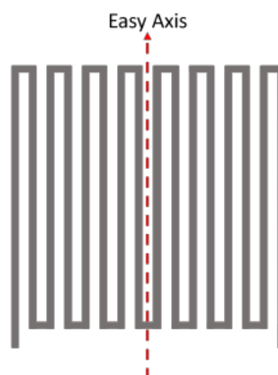

Figure 2.10: Example of meander structure of AMR sensors.

A strip of the meander of AMR sensors follows the rule $a > b \gg c$, where for these dimensions the typical orders of magnitude are μm for a and b, and nm for c, as shown in figure 2.11.

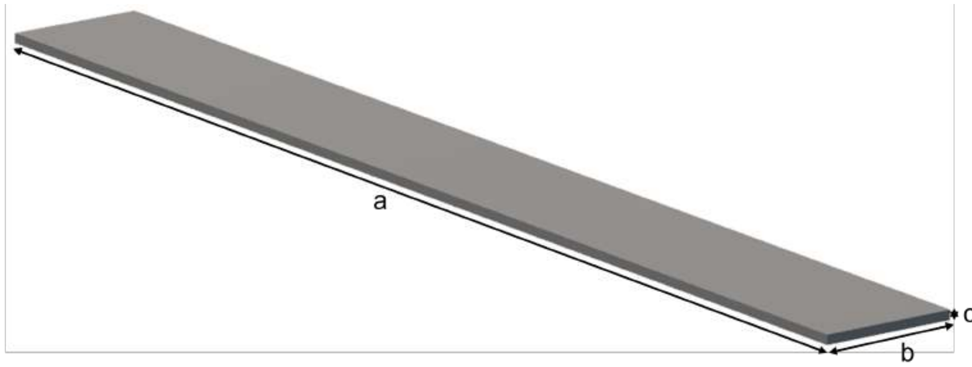

Figure 2.11: Schematic representation of a strip of the AMR meander, where a, b and c correspond to the length, width and thickness of the strip, and where $a > b \gg c$.

2.4.3 Configuration

In positioning applications AMR sensors are connected in full-bridges, which are composed of four varying elements, in this case the AMR sensors, and provide a higher output and a better thermal compensation [15] [18] [19]. The full bridge is biased with voltage, and its output can be calculated using equation 2.11, following the electric schematic of figure 2.12:

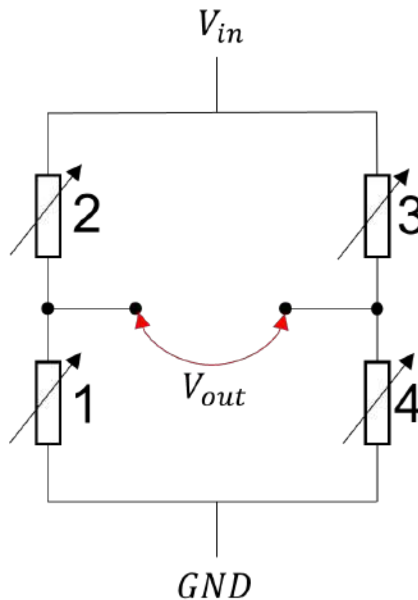

Figure 2.12: Electric schematic of a full bridge with four varying components. Each component is an AMR sensor.

$$V_{out} = \frac{R_2R_4 - R_1R_3}{(R_1 + R_2)(R_3 + R_4)}V_{in} \tag{2.11}$$

For positioning applications, two of these full bridges are used in each device, both biased by the same terminals. The electric schematic is represented in figure 2.13, and the outputs can be calculated using equation 2.11, replacing the indexes for the correct resistances.

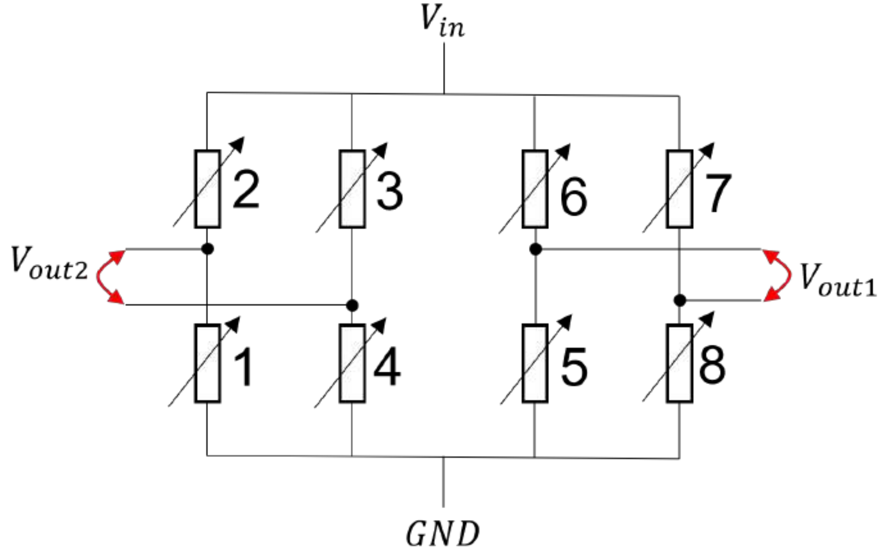

Figure 2.13: Two full bridges with four varying components each, with a shared bias. Each component is an AMR sensor.

In each bridge, opposing sensors must be paired in order to have the same resistance: following figure 2.12, $R_1 = R_3$ and $R_2 = R_4$ must be verified. Also, when the resistance of one pair is maximized, the other is minimized. This is achieved with a specific placement of the sensors along the device and will be clarified in section 2.5. Given this information, as well as already knowing that the AMR sensors' resistance will vary between $R = R_{min}$ and $R = R_{max} = R_{min} + \Delta R$, it is possible to try to obtain some more information about the behaviour of the bridge, mainly its maximum output.
The output will be maximized, in absolute value, when either of the pairs is maximized, meaning the other is minimized. This maximizes the numerator in equation 2.11. Assuming R_2 and R_4 are maximized: $R_2 = R_4 = R_{min} + \Delta R$, $R_1 = R_3 = R_{min}$, and so, replacing in equation 2.11:

$$
\begin{aligned}
\text{Replace} \qquad & V_{out} = \frac{(R_{min} + \Delta R)^2 - R_{min}^2}{(2R_{min} + \Delta R)^2} V_{in} \\
& \Leftrightarrow V_{out} = \frac{R_{min}^2 + 2R_{min}\Delta R + (\Delta R)^2 - R_{min}^2}{4R_{min}^2 + 2R_{min}\Delta R + (\Delta R)^2} V_{in} \\
\text{Divide by } \mathrm{R}_{\mathrm{min}}^2 \qquad & \Leftrightarrow V_{out} = \frac{2\frac{\Delta R}{R_{min}} + \left(\frac{\Delta R}{R_{min}}\right)^2}{4 + 2\frac{\Delta R}{R_{min}} + \left(\frac{\Delta R}{R_{min}}\right)^2} V_{in} \\
\text{Apply eq. 2.3} \qquad & \Leftrightarrow V_{out} = \frac{2MR + MR^2}{4 + 2MR + MR^2} V_{in} \\
& \Leftrightarrow V_{out} = \frac{MR}{2 + MR} V_{in}
\end{aligned}
\tag{2.12}
$$

Finally reaching equation 2.12, it is now obvious that the maximum output of the device will only depend on the MR ratio of the sensors. The actual value of resistance of the sensors will only influence the consumption of the device.
This is, however, a very ideal evaluation, where the four sensors are exactly the same. Imperfections in

the sensors result in a dispersion of resistance and MR ratio, which leads to this output generally being lower.

2.5 Incremental Linear Encoders

The incremental linear encoder uses the combined properties of the magnetic scale with the AMR sensors, although it requires mores elements for the acquisition and processing of the signals. It provides information on displacements from a reference, but is unable to provide an absolute position. Absolute positioning systems require a more complex magnetic scale, which is outside the scope of this dissertation. Reviewing the information from section 2.3, the magnetic scale generates a magnetic field, which direction rotates periodically, along the y direction (flying direction). The AMR sensors will be used to sense this magnetic field and measure its direction, allowing an indirect measurement of a displacement. For this to be possible, the device (and therefore the sensors) needs to placed parallel to the $y0z$ plane, as indicated in figure 2.14:

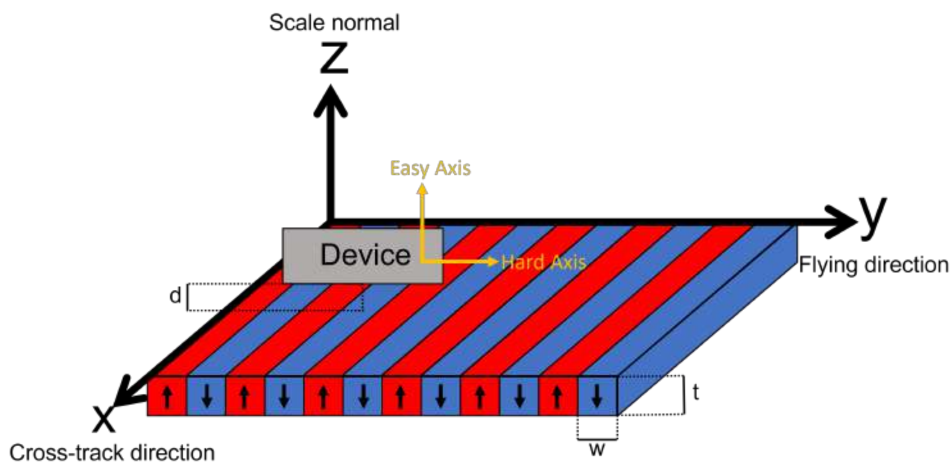

Figure 2.14: Device and sensor placement over a magnetic scale, parallel to the $y0z$ plane. This placement allows the AMR sensors to measure the direction of the field. The device is placed at a distance d from the magnetic scale.

The magnetic field direction is periodic with period equal to double the bit width. However, for AMR sensors, the resistance follows $R = R_{min} + \Delta R \cos^2 \theta$ (eq. 2.5), which means that the resistance of the AMR sensor will have half the period of the magnetic field. In other words, the resistance of an AMR sensor will be periodic with period equal to the bit width. Remembering the conditions imposed in section 2.4.3 for the full bridge, to have a pair of sensors with the same resistance, that pair of sensors needs to be one bit width apart (one period). For the opposing pair the same applies, so what is left is to decide the distance between pairs. Since what is required for maximum output is that when one pair's resistance is maximized, the other is minimized, the sensors from each pair must be separated by half a bit width. An example of a compact arrangement of sensors following these conditions is shown in figure 2.15.

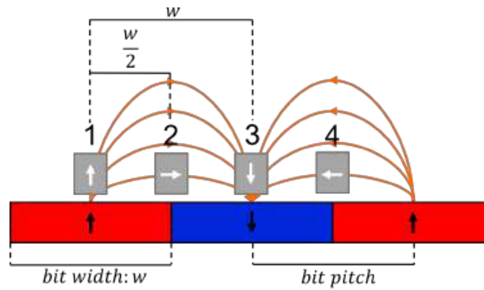

Figure 2.15: Compact arrangement of AMR sensors in a linear positioning device with one full bridge. Arrows in black represent the magnetization of the bits of the magnetic scale, arrows in white represent the magnetization of the AMR sensors. Sensors are numbered according to the numbering in figure 2.12.

.

The transfer curve of the AMR sensor is not linear (see figure 2.4), and so will not be the output of the full bridge. The output is sinusoidal, which is not ideal for a linear positioning application. To achieve a linear output, two full bridges are used, which produce two sinusoidal outputs in quadrature due to the periodic properties of the magnetic scale. The second bridge only needs to be displaced a quarter of the bit width and another example of a compact arrangement of the sensors is presented in figure 2.16.

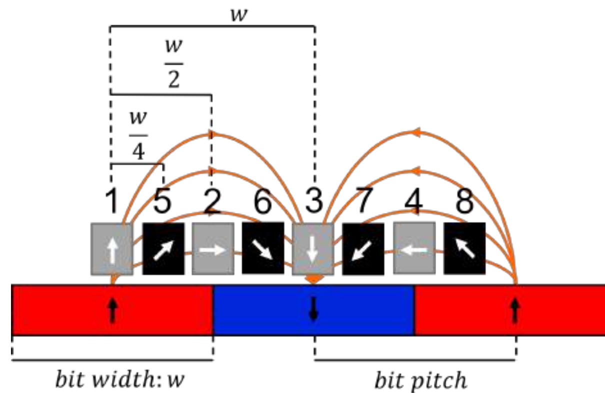

Figure 2.16: Compact arrangement of AMR sensors in a linear positioning device, with two full bridges. Arrows in black represent the magnetization of the bits of the magnetic scale, arrows in white represent the magnetization of the AMR sensors. Sensors are numbered according to the numbering in figure 2.13.

.

Similarly to the magnetic field, two periodic signals in quadrature are generated, which means that taking their arc-tangent gives a linear signal. With a few more terms, as described in equation 2.13, it is then possible to calculate a linear displacement, based on the output of the two full bridges [20]:

$$X = \frac{w}{2\pi} \arctan\left(\frac{Bridge2}{Bridge1}\right) + \frac{w}{2}\,, \tag{2.13}$$

where w is the scale period, or bit width, $Bridge1$ and $Bridge2$ are the outputs of the full bridges with sensors $S5$ to $S8$ and $S1$ to $S4$, respectively. This equation gives a relative position along one bit, from 0 to w.

Chapter 3

Sensor fabrication techniques and characterization methods

This chapter covers the fabrication techniques used to make the sensors used for this dissertation, as well as the characterization methods applied in order to obtain the desired information.

3.1 Fabrication

3.1.1 Ion Beam Deposition and Ion Beam Milling

Starting with Ion Beam Deposition (IBD), this is a widely employed technique, used to deposit thin films of materials on a chosen substrate. IBD equipment generally includes the following: a deposition gun, an assist gun, a target and a substrate table, all inside a vacuum chamber.
The process of IBD starts with the deposition gun. This is the name given to a small chamber where a plasma is formed with a RF power supply, from an inert gas such as Ar or Xe. The ions of this plasma are then accelerated in order to exit the deposition gun using an electric field and collimated into a beam. This ion beam is aimed at the target: a slab of the material that is going to be deposited.
The beam hits the target at an angle, and through momentum transfer it pulls out atoms from the target. The kinetic energy transferred to the atoms is enough to make them traverse the vacuum chamber towards the substrate table, where it then deposits on the substrate. The assist gun has two uses, one of them related to IBD. It is aimed at the substrate table, and during IBD it can be used to accelerate ions towards the substrate to provide further energy to the atoms being deposited. This extra provided energy can be helpful for the atoms to reorganize and reorient during deposition, to ensure a good crystal growth on the film, reducing possible defects, in which case it is called Ion Beam Assisted Deposition (IBAD).
The other use of the assist gun relates to the aforementioned Ion Beam Milling (IBM). This technique is used to remove material, in the same manner as in IBD, but now from the substrate or sample. The process is exactly the same: plasma is formed in the assist gun, accelerated towards the substrate where the ions collide with the atoms from the substrate, removing them through momentum transfer.

This process is purely physical, non selective and anisotropic. The components of an IBD/IBM system are arranged in a Z configuration, which can be observed in figure 3.1:

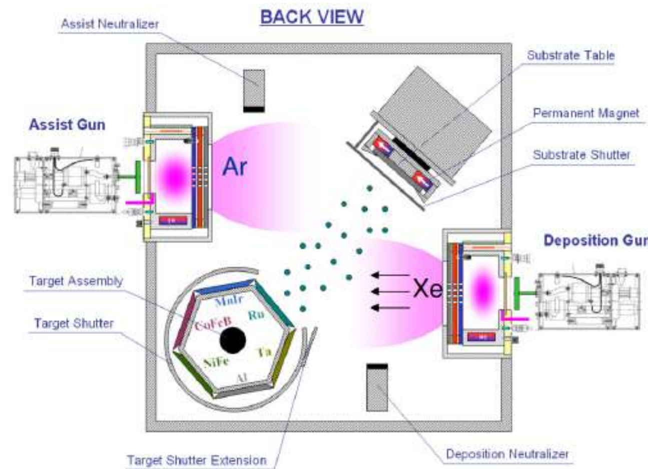

Figure 3.1: Schematic representation of an IBD/IBM system in Z configuration [21].

Some other important aspects about these processes:

- The substrate table can be equipped with an array of magnets that will generate an almost uniform magnetic film across the surface of the substrate. This can be used to define a magnetic easy axis during deposition, as the magnetic moments of the deposited atoms will align with the field
- During both IBD and IBM, the substrate table rotates at constant speed. This promotes the uniformity of the process across the substrate.´
- High vacuum is a priority in both processes, since without it the processes cannot occur. The ions need a clear path from the guns to the target or substrate, as well as the atoms from the target to the substrate. If not for the vacuum, the ions and atoms would collide with other particles on their trajectories. These undesired collisions would drain their kinetic energy, required for the process to work, as well as possibly deviating them from their desired trajectory.

3.1.2 Sputtering Deposition and Etching

Sputtering is a technique also used to deposit thin films of a desired material on a substrate. The process is done in a vacuum chamber for the same reasons as in IBD systems and the process is similar, based on the same principles.
In a sputtering chamber, a plasma is created using an inert gas such as Ar or Xe, but in this case it is created near the target containing the material that will be deposited. An electrical field accelerates the ions of this plasma towards the target. Upon collision with the target, the ions remove atoms from it through momentum transfer. Just like in an IBD system, those atoms then travel towards the substrate table. Usually, the target and the substrate table are opposite to one another, vertically.
A permanent magnet can be placed behind the target, generating a magnetic field that accelerates the electrons in the plasma and traps them in spiral trajectories, electrons that would otherwise hit the

substrate table (due to the electrical field used to accelerate the ions in the plasma towards the target). Those electrons, in turn, collide more with the plasma, ionizing the plasma further, due to their longer trajectories, which leads to higher deposition rates due to the larger ion density. This process is then referred to as Magnetron Sputtering.
The ions in the plasma can be accelerated using a DC or RF field, the first being used to deposit metals and the latter to deposit non conductive materials, such as oxides. In the case of metals, as the ions hit the target, their charge conducts through the metal, which causes no problems. With oxides on the other hand, the charge will accumulate, since the material is not conductive and the charge accumulation will in turn repel future ions, preventing further collisions with the target and thus halting the process. The RF field is then used to avoid this.
Similarly to an IBD/IBM system, a sputtering system can also be used to remove material from the substrate, simply by accelerating the ions towards the substrate instead. The process is also purely physical, non selective and anisotropic.

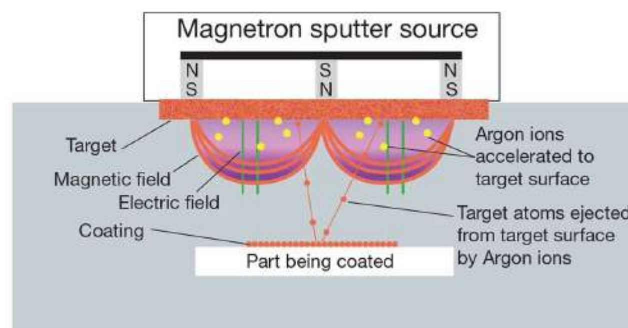

Figure 3.2: Schematic representation of a sputtering system in a vertical configuration [21].

3.1.3 Reactive Ion Etching

Reactive Ion Etching (RIE) is another technique used to remove material from a substrate or sample. The advantage of this technique over IBM or Sputter Etching is its high selectivity. Instead of using inert gases, other gases are used for the plasma, carefully selected in function of the material to be removed based on their reactivity. The accelerated ions remove atoms through momentum transfer as well, because of their kinetic energy, but mostly due to the chemical reaction that follows upon contact. This technique is highly selective it has much faster etch rates and it is isotropic.

3.1.4 Lithography

One of the key aspects of micro fabrication is lithography, since it is this technique that allows the patterning of the sensors. it is only through lithography that the desired shape and dimensions can be applied to the thin films to form the sensors. To define the pattern, two techniques can be used: etching or lift-off. In both cases, the substrate needs to be coated with a layer of photo-resist, which is where the pattern is actually first transferred to.

Photo-Resist Coating and Developing

Photo-resist is a photosensitive polymer, sensitive to specific wavelengths, and it is where the actual pattern is printed. Exposing the photo-resist to the specific wavelength can either reduce its average molecular weight, making it more soluble in certain solutions, or increase its average molecular weight, making it less soluble. The first case corresponds to a positive resist and the second to a negative resist. The solution used to dissolve the exposed or unexposed areas is called the developer. So, by exposing certain areas of a sample coated with this photo-resist, a pattern can be formed on this coating.
To coat a sample, the sample is rotated at high speeds ($3000 - 6000rpm$) and a photo-resist dispenser will drop the resist on top of the sample. As it rotates, the resist spreads across the surface and the excess flies off the borders due to the high speed. The rotation speed is adjusted to the viscosity of the resist, in order to control the resist thickness. The rotation also ensures an almost uniform spread of the resist across the sample.

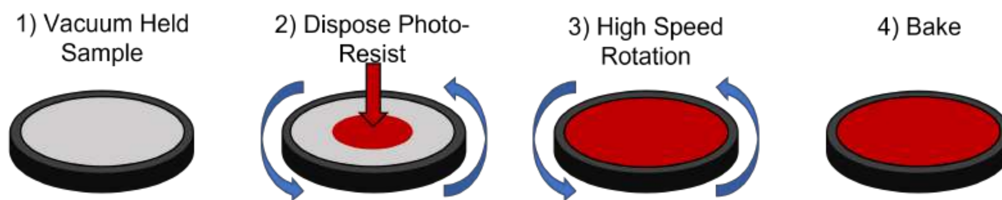

Figure 3.3: Schematic representation of the photo-resist coating process. Adapted from [21].

The sample is then baked to remove the solvents from the resist, so it sets on the substrate, and to eliminate stress due to the high speed rotation. The sample is then ready to receive the pattern, which can occur via Direct Write Laser (DWL) or a Hard Mask. DWL makes use of a laser, with a nanometric spot diameter, to expose the desired locations of the sample. This process can be slow and lead to loss of uniformity, but it compensates for how flexible it is, since the masks can be easily changed as they are software masks. Using a Hard Mask makes the exposure faster and more uniform. A physical, opaque, mask is made, that covers the sample leaving exposed only the desired areas, allowing a one shot exposure. Hard masks are, however, expensive and once made cannot be changed. When producing sensors in a large scale, for a standardized product, uniformity is key, so that all fabricated devices have very similar properties, the main one being resistance, since all the enveloping electronics have to be dimensioned appropriately, according to the device's resistance. A schematic of both processes can be seen in figure 3.4:

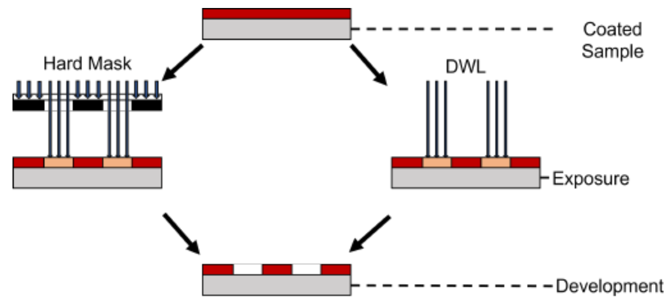

Figure 3.4: Schematic representation of the DWL and Hard mask exposure processes. Adapted from [21].

After exposure, the sample is baked again, to remove stress and stationary waves from the resist due to the exposure. Finally it is developed: it is doused with the solvent that will dissolve the exposed or unexposed area, depending on the type of resist, revealing the pattern.

Etching vs Lift-off

To define a layer's pattern through etching, the layer is first deposited across the whole sample. Followed by coating and exposure, the mask is created. In this case, the resist covers and protects the areas that are going to be kept, an inverted mask (see figure 3.6). The sample is then etched, typically by IBM. Being non selective, this process will etch away both the unprotected layer material as well as the resist at approximately the same rate, so the resist must always be thicker than the layer that is going to be etched. After the etching is complete, the resist can be removed in an ultrasound bath, with the sample immersed in $resist\ strip$, a solution that will dissolve the resist, regardless of its type and state.
When recurring to the Lift-off process, lithography happens first. The sample is coated and pre-developed. Pre-development will improve the profile of the resist after exposure, resulting in cleaner edges of the layer after development. it is then exposed, creating a mask that covers the areas where the next layer should not exist, a non inverted mask (see figure 3.6). The desired material for the next layer is then deposited over the mask, filling in the gaps where there is no resist. The resist is then dissolved in the same $resist\ strip$ solution, and the material deposited on top of it is removed as well, leaving only what was deposited directly on the substrate.
Both processes are summarized in figure 3.5:

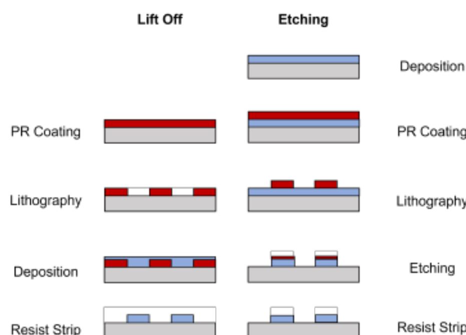

Figure 3.5: Schematic representation of the etching and lift-off lithography processes. Adapted from [21].

(a) Non Inverted mask.

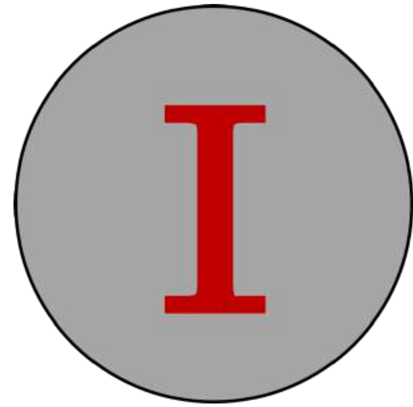

(b) Inverted mask.

Figure 3.6: Representation of the non inverted and inverted masks. The regions highlighted in red contain the resist. Adapted from [21].

3.1.5 Magnetic Annealing

Magnetic annealing can be used to induce magnetic anisotropies in a material. For the case of AMR sensors, it can be used to reinforce the easy axis. Annealing also promotes the re-crystallization of the layers, repairing possible defects in crystallography or even changing the crystalline order of a material entirely. The grain in the material will also grow, promoting larger magnetic domains, and thus a behaviour closer to the single domain. Overall, it can also improve the AMR ratio of the sensor.

This process is also done in vacuum to prevent oxidation. The sample is first heated to high temperatures (typically 200$°C$ to 400$°C$) and then kept at the desired temperature for the desired time. Afterwards, the sample is cooled in the presence of a magnetic field. The field should be aligned with the easy axis in order to reinforce the anisotropy along that direction. Cooling the sample within a magnetic field will force the magnetic moments to align with the field as they lose thermal energy. This promotes grain and domain growth with a preferred magnetic direction. A schematic of the stages of the process is given as example in figure 3.7:

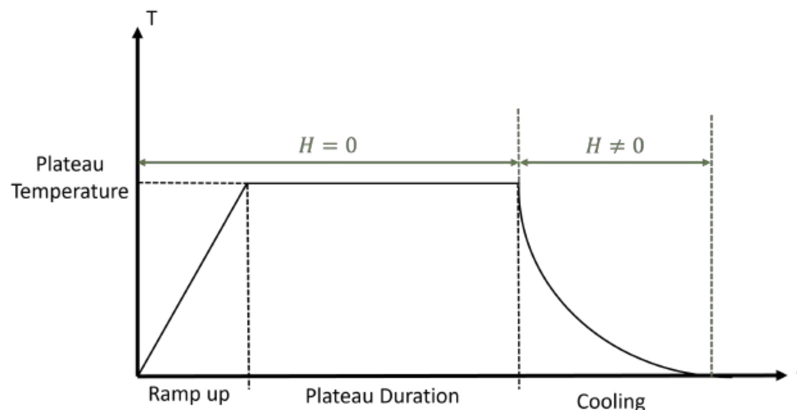

Figure 3.7: Example of a magnetic annealing cycle. Temperature rises during ramp up, up to a plateau temperature that is maintained for a certain time. After that, cooling can be done inside a magnetic field to reinforce the easy axis.

3.2 Characterization

Characterization of the sensors is a crucial step that follows fabrication. Many properties can be studied and measured, though some are more relevant than others depending on the application. Here, the characterization methods used in this dissertation are covered.

3.2.1 X-ray Diffractometry

X-ray diffractometry offers information on the crystallographic structure of materials. It can give insight on the crystalline phase, the interplanar distance and the grain size. An x-ray diffractometer is composed of three elements: an x-ray source, an x-ray detector and a sample holder.
The x-ray source is a cathode ray tube, where an electrical current is imposed on a filament, high enough to lead to thermionic emission of electrons. These electrons are accelerated by an electrical field towards a target, of materials such as Cu or Mo. These accelerated electrons are energetic enough to collide or scatter on electrons from the inner shells of the atoms of these materials. Those collisions lead to emission of radiation that, given the materials chosen for the target, has typical x-ray wavelengths. These emissions can be filtered to obtain a monochromatic x-ray beam.
The emitted x-rays are directed at the sample to be studied at an angle, where diffraction will happen because x-ray wavelength is comparable to inter-planar distance. The x-ray detector is facing opposite to the x-ray source, pointing at the sample at the same angle as the source. Measurements take place at different angles, with the source and detector always at the same angle, θ, with the sample surface (this corresponds to the Bragg-Brentano geometry; see figure 3.8). The x-ray diffractometer records the angles (2θ) and measured counts (N) by the detector at those angles, constructing a diffraction pattern. That diffraction pattern will have peaks with properties (angle at which the peak occurs, FWHM of the peak) varying according to the materials' properties (inter-planar distance, grain size).

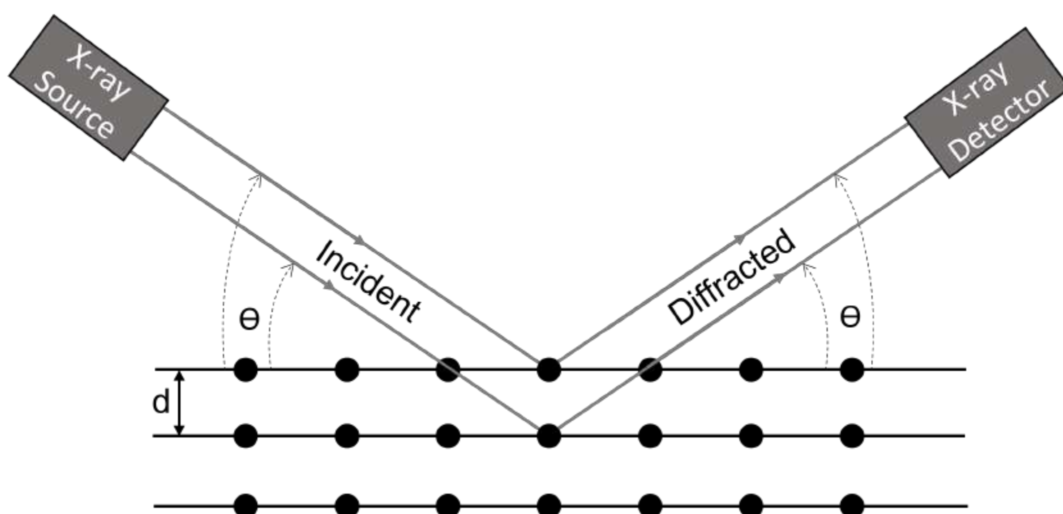

Figure 3.8: X-ray diffraction principle, using the Bragg-Brentano geometry.

For this dissertation this technique was used to study the grain size in the samples, as well as the inter planar distance. The desired properties are calculated using equations 3.1 and 3.2, which correspond

to Bragg's Law and Scherrer's equation:

$$d = \frac{\lambda}{2\sin(\theta)} \tag{3.1}$$

$$\tau = \frac{K\lambda}{FWHM\cos(\theta)}\,, \tag{3.2}$$

where d is the inter-planar distance, λ is the wavelength of the x-rays used, θ is the angle of the peak being used for calculations, τ is the grain size, and $FWHM$ is the Full Width at Half Maximum of the peak used for calculations. K is a material dependent constant.
The x-ray diffractometer at INESC-MN, Diffraktometer D5000, has a Mo target, that produces a collimated x-ray beam of $\lambda = 0.071nm$ and is shown in figure **??**.

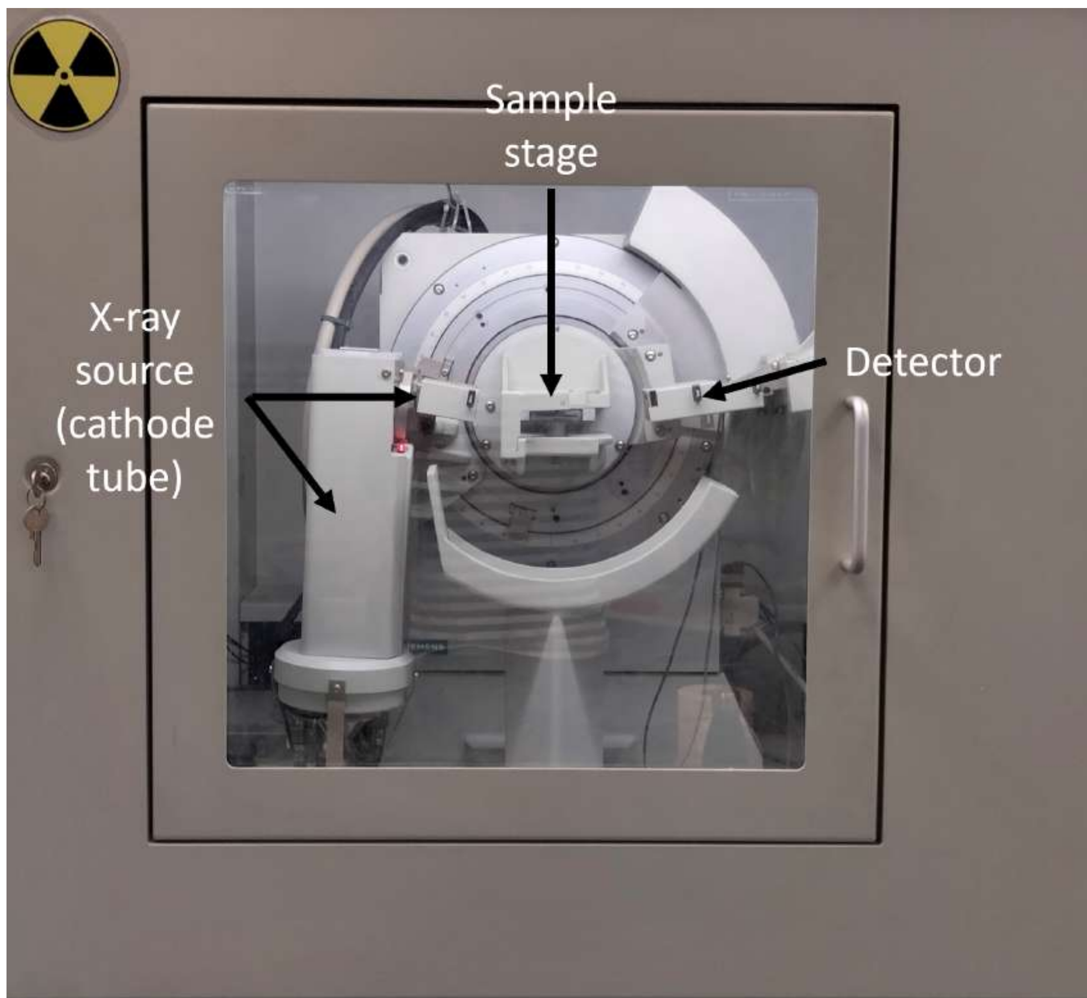

Figure 3.9: Picture of the diffractometer.

3.2.2 Transfer Curve

The transfer curve will be the most important method that will be used to characterize the sensors, since it gives information on the response of the sensor to a magnetic field. This is done by biasing the device with a current, in order to measure a voltage so as to the determine the device's resistance. These measurements are done whilst the sample is inside a magnetic field, sweeping from negative

to positive and back to negative values along one direction. That direction will be the magnetic hard axis of the device, to change the direction of the magnetization. These measurements were done with two probes, placed at the VB and GND terminals represented on figure 2.13. Measuring the transfer curve with these terminals, instead of measuring the sensors one by one, saves time, as the values of resistance would differ from one device to the other if at least one of the sensors is damaged or faulty. The transfer curve gives information on four key properties: maximum and minimum resistance, AMR ratio, coercivity and saturation:

- The maximum resistance is found at zero external magnetic field, $H = 0$, and the minimum resistance is found when the device reaches saturation, when the magnetization takes the direction of the external magnetic field applied in the hard axis direction.

- The AMR ratio is calculated using equation 2.5, using the values of R_{min} and R_{max} obtained in the measurement.

- Coercivity is given by the difference in the x-axis between the two sweeps: negative to positive fields and positive to negative. This is done by calculating external magnetic field at which the resistance is equal, in both curves. Since the same value of resistance occurs four times, this can be done for positive and negative fields. The quantity is represented in the inset plot of figure 3.10.

- To quantify and evaluate saturation, instead of determining the saturation field, which can be quite arbitrary to determine from the transfer curve, this parameter is quantified by the FWHM of the curves, for comparison between samples.

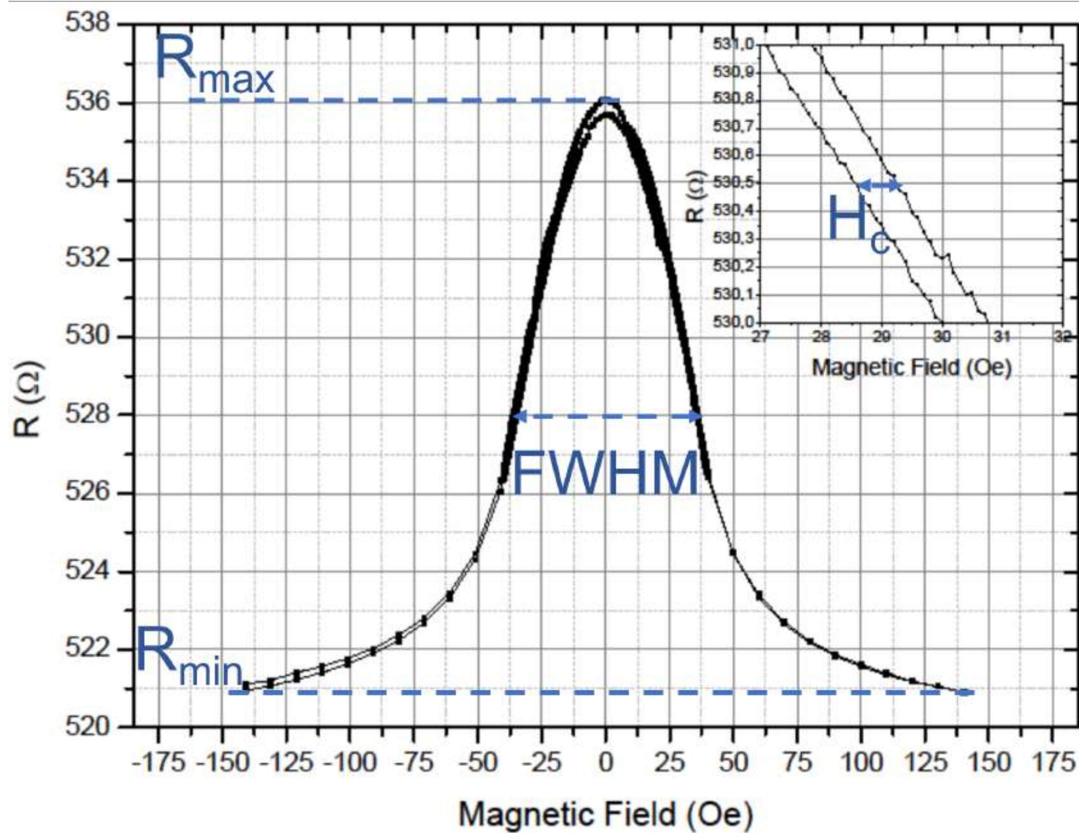

Figure 3.10: Representation of the key properties extracted from the transfer curve. The coercivity is represented in the inset plot, which has a smaller scale focusing on the positive branch, but the same measurement applies to the negative branch.

These parameters will influence the performance of the sensor: The resistance will determine the power consumption, the AMR ratio will influence the output of the device, the coercivity can influence hysteresis of the positioning measurements and saturation will dictate how far from the scale the device can operate correctly.

The transfer curves were measured on two different stations: a manual measuring station and an auto-prober. The measurement procedure is the same, but the manual setup was used to measure transfer curves with a smaller magnetic field step, for measurements with more resolution in order to make the calculation of coercivity possible , whilst the auto-prober was used to measure several sensors across a sample, to provide information on uniformity, mainly of the resistance of the sensors, and using a larger magnetic field step.

The manual setup is composed of four TiW probes, of which only two were used, that establish the electrical contact with the devices. A KEITHLEY 220 Programmable current source is used to bias the devices with constant current, and a KEITHLEY 182 Sensitive Digital Voltmeter then measures the resulting voltage on the devices. The resistance is then calculated with Ohm's Law, knowing the set value of current and having the measured value of the resulting tension. The magnetic field used in these measurements is generated using Helmholtz coils, supplied by a KEPCO Bipolar Power Supply,

and it can go up to 140Oe. The use of Helmholtz coils in the magnetic field generation is crucial for measuring very low coercivity values, as they have no intrinsic coercivity themselves that could influence the measurements. Figure 3.11 shows a picture of the manual measurement setup with proper labelling of the components.

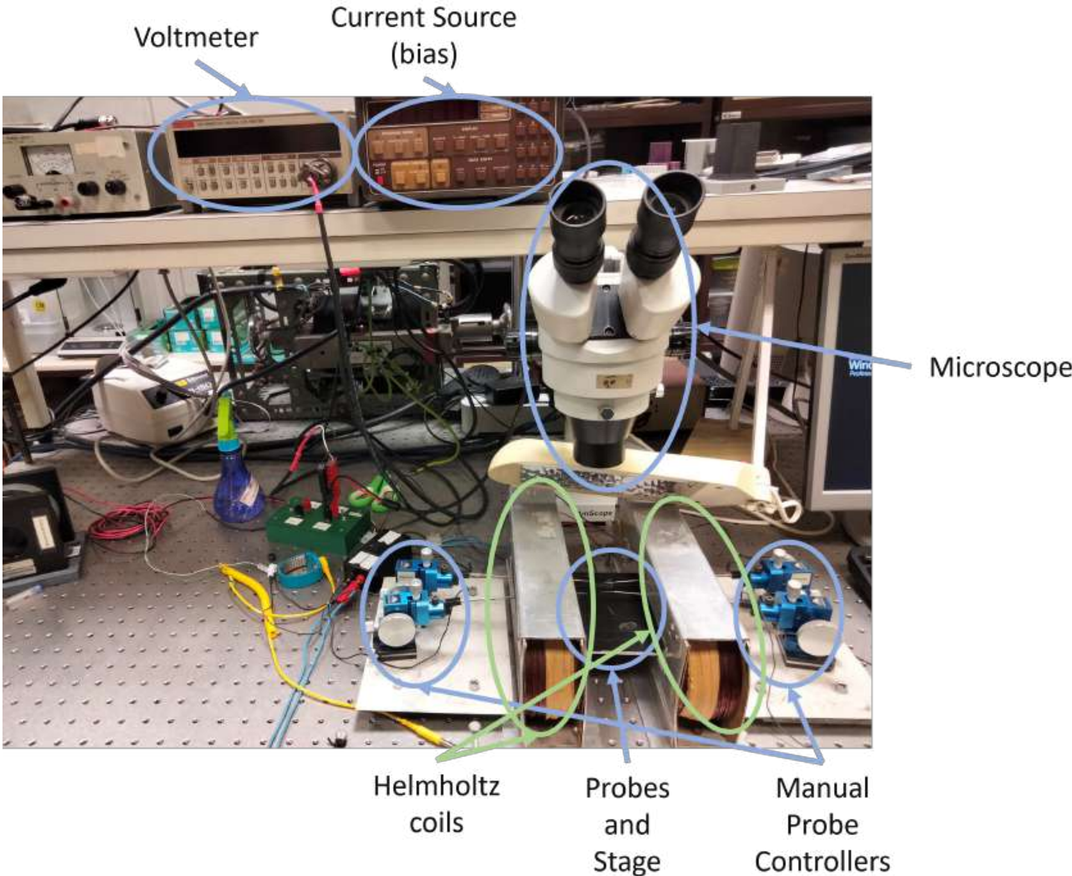

Figure 3.11: Manual measurement setup used to measure transfer curves.

The auto-prober station is very similarly equipped, with four TiW probes out of which only two were used, a current source to supply Hlemholtz coils that generate the magnetic field, a current source to bias the devices and a digital voltmeter to measure the resulting output. The only difference is that the sample is placed on a moving stage. During the measurements across a sample, the probes remain stationary, and the stage is moved, controlled by software, in order to have the probes make contact with different sensors on the sample, and thus map the entire sample. Figure 3.12 shows a picture of the auto-prober setup with proper labelling of the components.

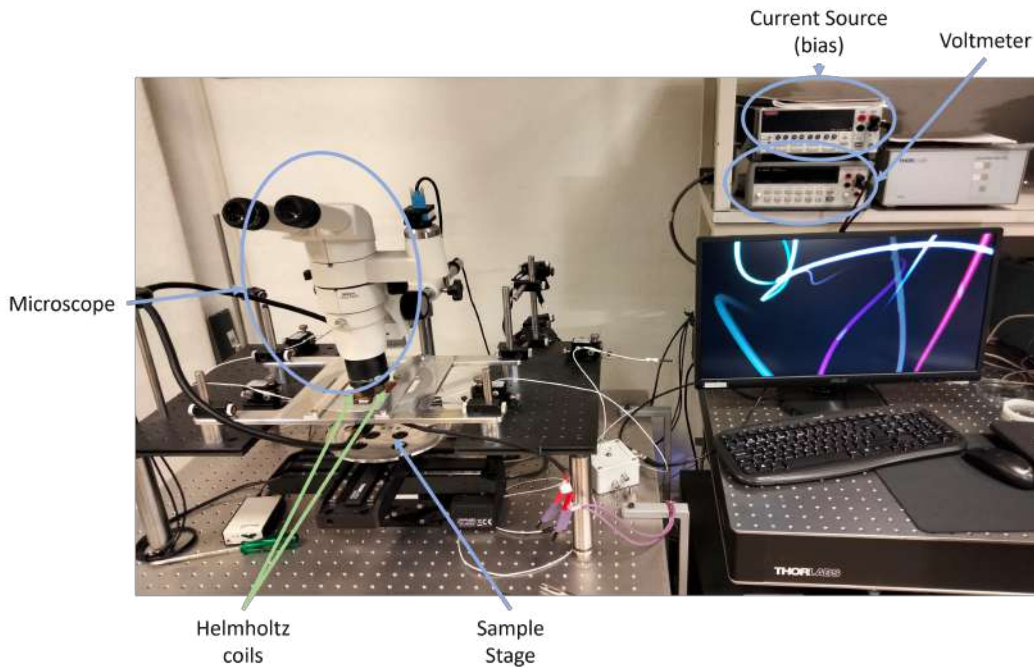

Figure 3.12: Auto-prober setup used to measure transfer curves.

With the two probe configuration, the resistance measured is not only the resistance of the sensors, but also the contact resistance. To improve the MR ratio of a device, this contact resistance should be minimized, since it adds a background resistance, over which the variation of the sensor's resistance will seem smaller, effectively leading to lower MR ratio values. The two probe configuration can be approximated to the electrical circuit shown in figure 3.13:

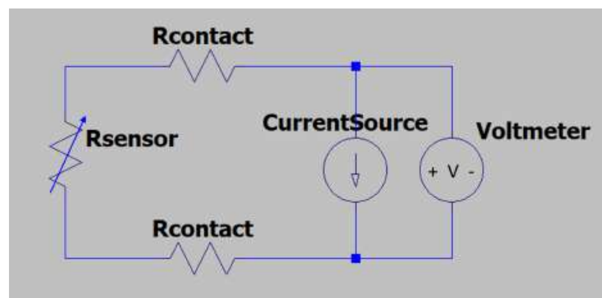

Figure 3.13: Electric circuit equivalent to the two probe measurement.

The contact resistance negatively impacts the MR ratio. The higher it is, the lower the MR ratio will be, so this quantity should always be minimized.

3.2.3 Scanner Performance

The ultimate purpose of the fabricated sensors is to use them in a linear positioning system. With that in mind, the sensors can be tested on such a system, referred here as the scanner. The scanner itself is composed of a moving stage that traverses in the x direction, and two threads that allow the movement of an acquisition board, over the moving stage, in the y and z directions (following the same referential

as in figure 2.14). The acquisition board is responsible for measuring the output of the sensors, through the two bridge outputs. For this particular work, a generic magnetic scale was placed on the moving stage, to scan with the sensors moving in the y direction. For this setup, the sensors have to be cut and assembled onto a PCB that will connect to the acquisition board.

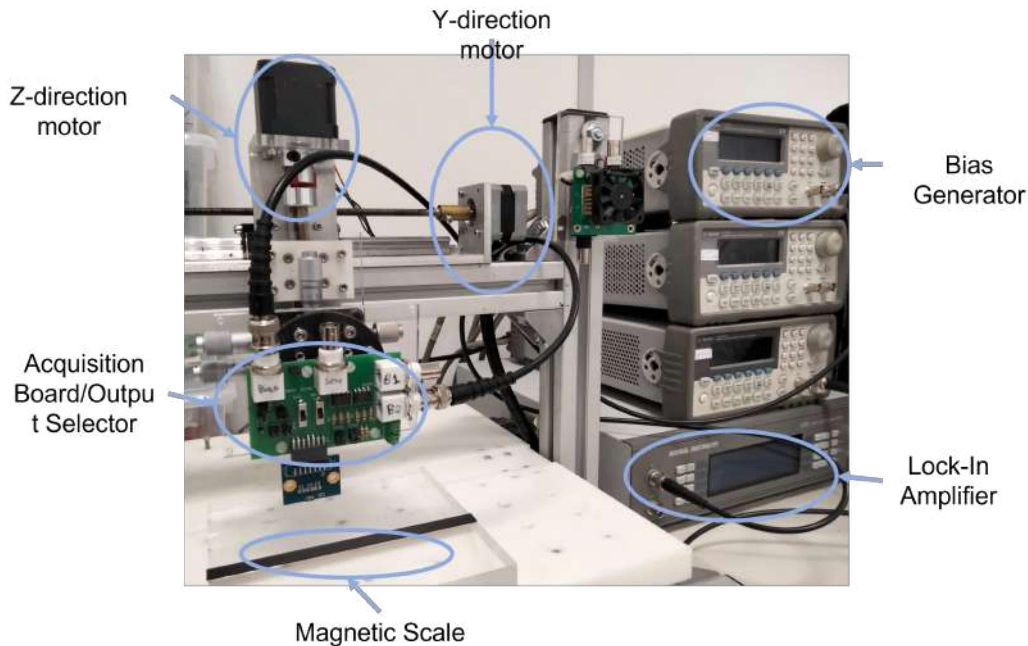

Figure 3.14: Setup for scanner tests at INESC-MN.

The sensors are biased with an AC signal. The desired amplitude and frequency can be selected with the control software, that controls the biasing, the measuring and the stage. On this software, the user can select the desired amplitude and frequency of the bias signal. A reference signal with matching frequency is generated and supplied to the lock-in amplifier. The lock-in amplifier takes this reference signal to make use of phase sensitive detection, to capture only a signal with matching frequency and phase . The value read by the lock-in amplifier is the amplitude of the sine wave, so the frequency of the bias signal is not present in the final measured data, and the phase is used to determine if the output should be considered positive or negative, as the Lock-in amplifier outputs the absolute value only. These measurements are very effective in cancelling noise, providing filtered signal. On the software it is also possible to select the ADC full-scale: adjusting the scale to the expected signal improves the resolution of the measurement.

Sensor assembly onto PCB

To prepare the sensors to be used in the sensor they must first be cut, separating the dies, each containing the eight sensors in two full bridges required. These dies are then glued to a PCB and through wirebonding, the pads on the die are connected to the respective tracks of the PCB and therefore connected to the pin array on the opposite end of the PCB.

Acquisition Board

A first acquisition board was designed and prepared specifically for testing the fabricated AMR sensors in the scope of this dissertation. This first board was planned in order to allow the user the selection of two out of the total six terminals of the die for measuring. This way it is possible to measure the response of each individual AMR meander. However, this first draft was put aside because it was not suitable to measure the output of the full bridges. For that, it would require additional components, to make a differential measurement between the respective terminals that give the bridge output, in order to eliminate the common mode gain present. Although it is possible to calculate the bridge output based on the value of resistance of each meander using equation 2.12, this method would not be accurate as it would require a total of eight scans to calculate the output of the two bridges (one scan per bridge element). Therefore, a second board was designed.
To measure the output of the bridges, additional electronics were added to the board, as the measurement is required to be differential. When measuring the output of a bridge, there is a common mode level, equal to half of the bias tension, that will be present in the measurements [22]. To eliminate the common mode level, a single-op-amp differential amplifier can be used, which has the electric schematic found in figure 3.15 [22].

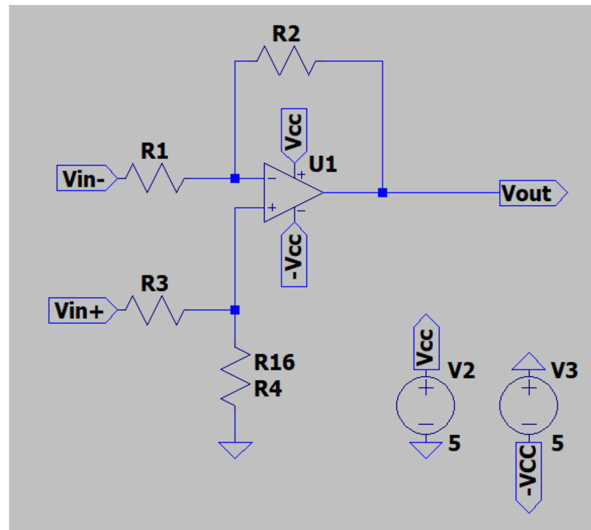

Figure 3.15: Electric circuit of the differential amplifier.

The output of the differential amplifier is given by:

$$V_{out} = A_d V_{In_d} + A_c V_{In_{cm}} \, , \tag{3.3}$$

where A_d is the differential gain, A_c is the common mode gain, V_{In_d} is the differential input ($V_{in+} - V_{in-}$), and $V_{In_{cm}}$ is the common mode level [22]. The single-op-amp differential amplifier should be scaled to follow the condition:

$$\frac{R_4}{R_3} = \frac{R_2}{R_1} \, , \tag{3.4}$$

which then results in a differential gain given by:

$$A_d = \frac{R_2}{R_1} \tag{3.5}$$

With MR ratios of around 2% to 3%, equation 2.12 predicts a maximum output of ≈ 50mV to ≈ 74mV, so amplification is not required. Choosing to use a unity-gain differential amplifier ($A_d = 1$), sets $R_2 = R_1$, which means the signal does not get amplified. Also, respecting the condition present in equation 3.4, the resistances should all be the same for this particular case, $R_1 = R_2 = R_3 = R_4$ [22].

Regarding now the common mode gain, it is given by the following equation:

$$A_{cm} = \frac{R_4}{R_4 + R_3}\left(1 - \frac{R_2}{R_1}\frac{R_3}{R_4}\right), \tag{3.6}$$

which with the resistances all being the same, yields $A_{cm} = 0$. Of course, this is an ideal scenario. There will always be a slight mismatch in resistance values, but A_{cm} will still be low enough to attenuate the common mode level [22]. With the two associated gains to the differential amplifier, the CMRR can be calculated with the following equation:

$$CMRR = 20log\frac{|A_d|}{|A_{cm}|}, \tag{3.7}$$

which is ideally $CMRR = \infty$, if $A_{cm} = 0$.

Another aspect to consider about the single-op-amp differential amplifier is that it requires a large differential input resistance, $R_{Id} = 2R_1$. This would be a problem if the signal required amplification, as R_1 would have to take large values, and R_2 even larger to effectively have any gain. However, since amplification is not required, this circuit serves the purposes well.

To verify the proper functioning of this circuit, a simulation was run in LTSpice, using the circuit present in figure 3.16, with the values of each component present in table 3.1. The resistance values of the bridge were chosen considering the expected resistance values of the fabricated sensors.

Table 3.1: Value of components used in the electrical simulation.

	Bridge					Differential Amp.			
	V_{bias}	$R_1(\Omega)$	$R_2(\Omega)$	$R_3(\Omega)$	$R_4(\Omega)$	$R_9(\Omega)$	$R_10(\Omega)$	$R_11(\Omega)$	$R_12(\Omega)$
Value	5V, 10kHz	1000	1030	1000	1030	100k	100k	100k	100k

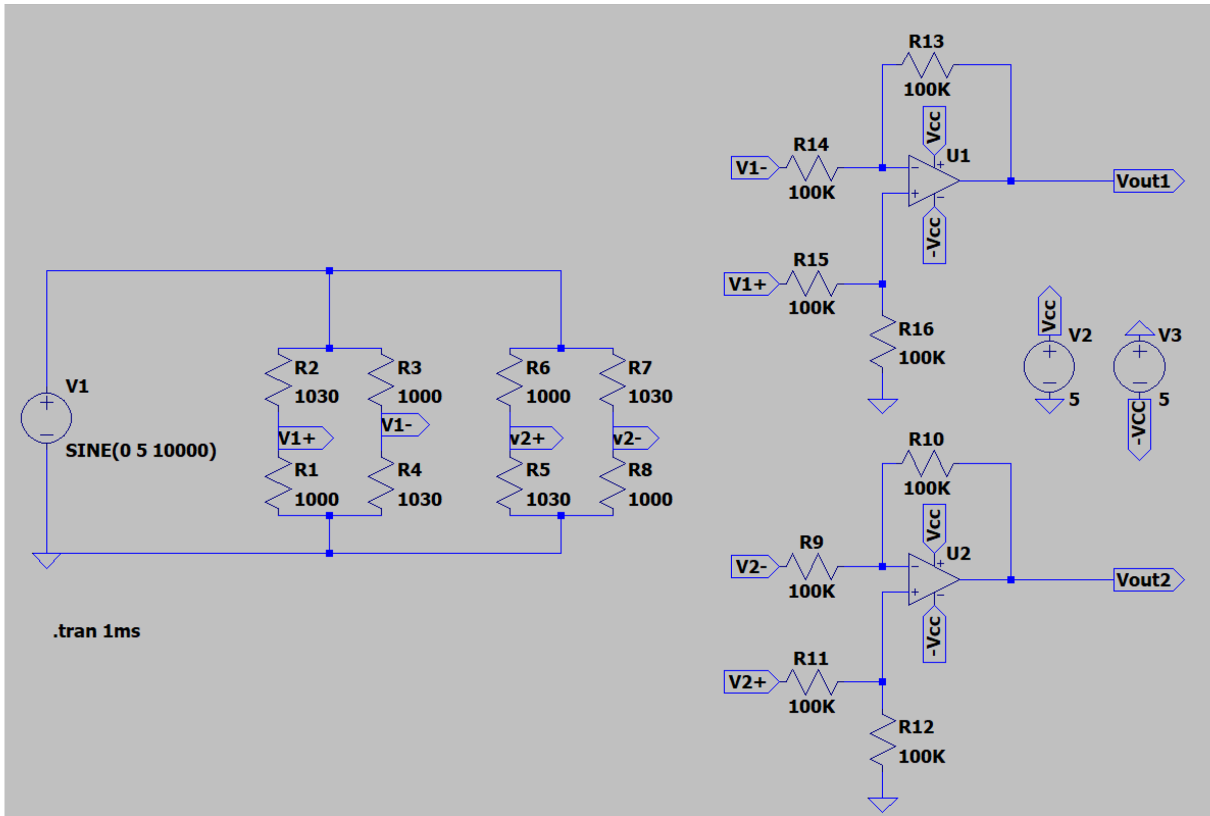

Figure 3.16: Electric circuit used in the simulation. Contains two bridges replicating the response of the AMR sensors, where in one the output is maximized and in the other minimized ($R_2 = R_4 = R_{max}$, $R_1 = R_3 = R_{min}$ and $R_5 = R_7 = R_{max}$, $R_6 = R_8 = R_{min}$). Since the biasing is done with AC, the outputs are expected to be in phase opposition. The output is put through the differential amplifiers to get the desired results.

Figure 3.17 shows the results of the simulation when biasing the bridge with AC 5V, with a signal of 10kHz frequency. Signal V_{outx} is the output of the differential amplifier, and $V_{x+} - V_{x-}$ is the differential tension between the two bridge output terminals, calculated by the simulation. It's possible to see that the two match, so the circuit measures the output correctly and eliminates common mode voltage effectively.

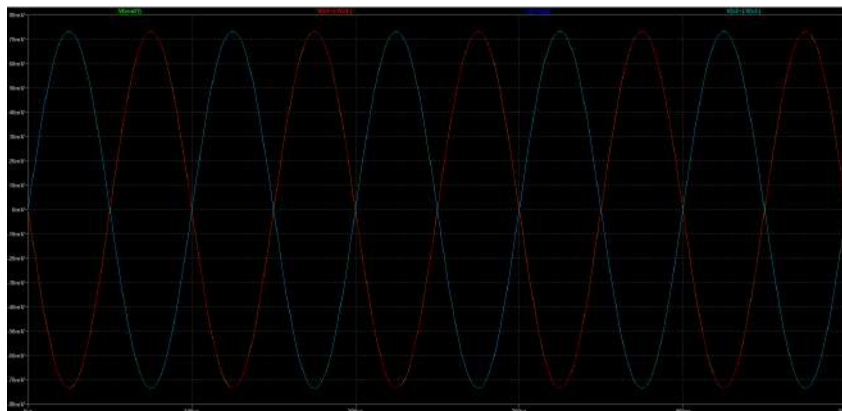

Figure 3.17: Results of the simulation of the differential amplifier circuit applied to the bridge outputs.

As expected, the outputs are in phase opposition since one bridge's output is maximized and the other is minimized, and the biasing is being done with AC. In figure 3.18 it's easier to see that the signals

V_{outx} and $V_{x+} - V_{x-}$ match:

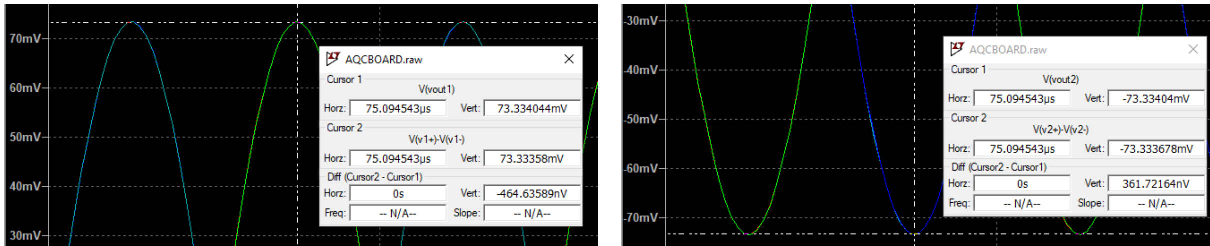

(a) Simulation results for V_{out1}.

(b) Simulation results for V_{out2}.

Figure 3.18: Simulation results evidencing the match between the signals V_{outx} and $V_{x+} - V_{x-}$.

This circuit was then implemented in the acquisition board, using an OPA33PA operational amplifier with $CMRR = 40dB$ at $10kHz$. Figure 3.19 contains a picture of the acquisition board with proper labelling of components.

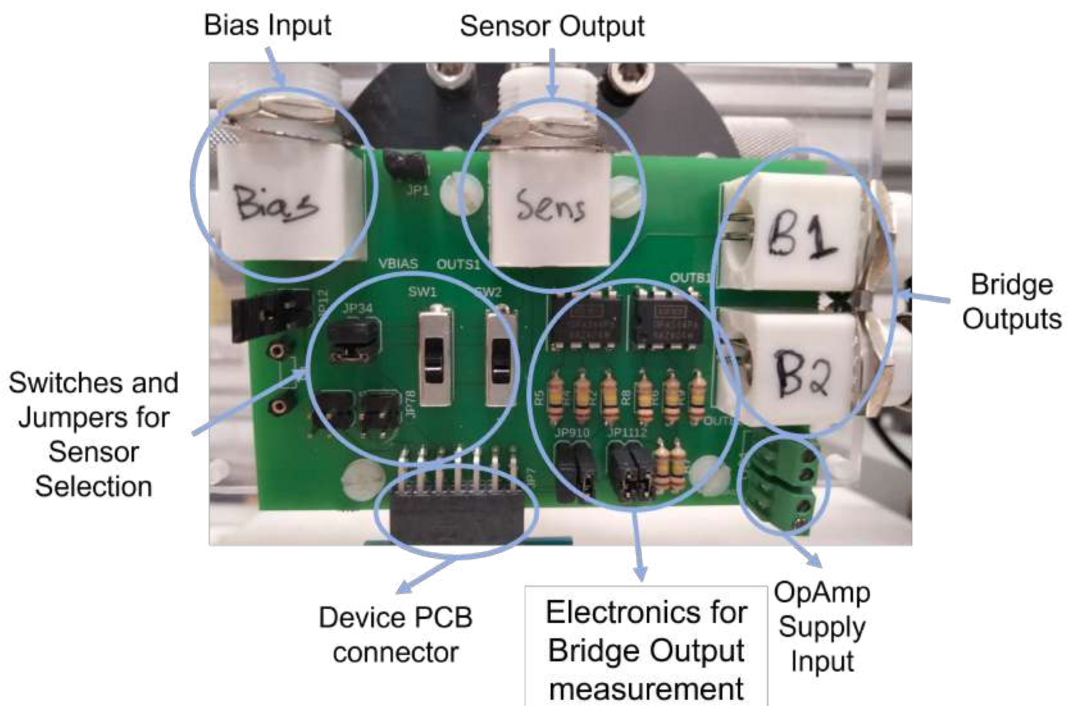

Figure 3.19: Acquisition board used in the scanner setup to measure individual sensor outputs and full bridge outputs.

With this board it is possible to bias the device and measure the output of either the meanders or bridges. The board is connected to a power source, that provides the bias voltage, and a differential amplifier. The bridge outputs are separated for the possibility of measuring both outputs in a single scan. The PCB for this board can be found in appendix B, as well as a table with the combinations of jumpers and switch positions for each output.

Scanner Data

Measurements on the scanner provide data on the performance of the device. Some of the key parameters possible to study with the scanner are accuracy, repeatability, hysteresis and flying height limit. Other important aspects include bridge offset, bridge mismatch, amplitude and phase, which can be analysed with polar plots of the two bridge outputs, considering they should be in quadrature as described in section 2.5, the polar plot should be a perfect circle [23]. The identifiable issues through the polar plot are shown in figure 3.20:

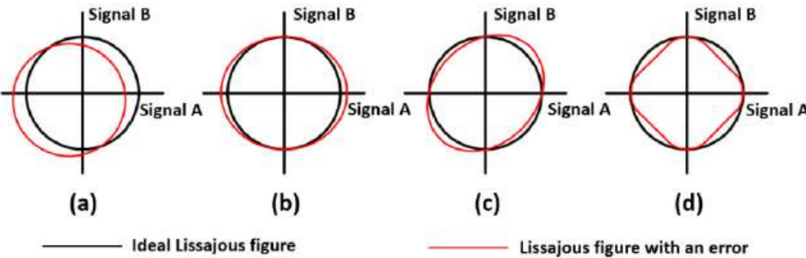

Figure 3.20: Example of polar plots of the bridge outputs and identifiable issues. From [23].

Because the maximum resolution of the scanner motion controller at INESC-MN is $8\mu m$, hysteresis measurements are not possible. This property should have lower values that this resolution, that are therefore unable to be measured with the current setup.

Chapter 4

Implementation

4.1 Fabricated Samples

4.1.1 Unpatterned Samples

Four unpatterned samples were produced to study the effects of annealing time on the crystallographic structure of the material, mainly grain size and inter-planar distance. Table 4.1 summarizes the composition of these test samples. The samples are identified by their buffer layer description.

Table 4.1: Composition different unpatterned test samples. Thickness between brackets given in Å.

Sample	Substrate	Buffer	Sensor	Capping	Passivation 1	Contacts	Passivation
Ta(50)	Glass	Ta (50)	NiFe (400)	Ta (50)	SiO_2 (2000)	Al (6000) + TiW(N) (150)	SiO_2 (1500)
NiFeCr(50)		NiFeCr (50)	NiFe (400)	NiFeCr(50)			
NiFeCr(100)		NiFeCr (100)	NiFe (400)				
NiFeCr(150)		NiFeCr (150)	NiFe (300)				

4.1.2 Patterned Samples

Six samples were produced in total, on 1×1 inch samples, using the same fabrication process between them (see Appendix A for the process Runsheet). Each sample contained a total of eighty four sensors, twelve of each seven different tested designs.

Two were produced with the purpose of testing and comparing two different buffer materials: Ta and NiFeCr, with the same thickness. The other four samples have varying buffer thicknesses of NiFeCr. Table 4.2 summarizes the samples' compositions. The samples are identified by their buffer layer description. The first four samples are identical to the unpatterned samples made.

Table 4.2: Composition different patterned test samples. Thickness between brackets given in Å.

Sample	Substrate	Buffer	Sensor	Capping	Passivation 1	Contacts	Passivation
Ta(50)	$Si + SiO_2$	Ta (50)	NiFe (400)	Ta (50)	SiO_2 (2000)	Al (6000) + TiW(N) (150)	SiO_2 (1500)
NiFeCr(50)		NiFeCr (50)	NiFe (400)	NiFeCr(50)			
NiFeCr(100)		NiFeCr (100)	NiFe (400)				
NiFeCr(150)		NiFeCr (150)	NiFe (300)				
Ta(30)+NiFeCr(300)	$Si + SiO_2$	Ta (30) + NiFeCr (300)	NiFe (400)	NiFeCr(50)	SiO_2 (2000)	Al (6000) + TiW(N) (150)	SiO_2 (1500)
NiFeCr(300)		NiFeCr (300)	NiFe (400)				

NiFeCr(150) sample has a lower thickness sensor layer: 300Å of NiFe instead of 400Å, to maintain a total stack size similar to the samples above it in table 4.3, in order to have similar resistances. The samples were submitted to annealing at 350°C, the first four samples for two hours, and the last two samples for thirty minutes. All the samples cooled down in a magnetic field of $1T$, with their easy axis aligned with the field.

Table 4.3: Composition different test samples. Thickness between brackets given in Å.

Sample	Temperature (°C)	Duration (mins)
Ta(50)	350	120
NiFeCr(50)		
NiFeCr(100)		
NiFeCr(150)		
Ta(30)+NiFeCr(300)		30
NiFeCr(300)		

4.2 Fabrication Process

The fabrication process of the AMR sensors took place at INESC-MN, making use of their facilities and equipment. Several different samples were fabricated and tested, following the same fabrication process, which is described in this section. All samples were fabricated on a Si/SiO(200nm) substrate. In each following subsection, a schematic representation of the sample after each step is presented. The process took place in a class 100 cleanroom, following the runsheet found in appendix A.

4.2.1 Sensor Deposition - Ion Beam Deposition

The first step in creating the AMR sensors was the deposition of the first level, composed of three layers: buffer layer, sensitive layer and capping layer. This step was accomplished at INESC-MN, using the machine N3000 with a Base pressure of $1 \times 10^{-7} Torr$. The thickness of each layer is given in table 4.2, with a total stack thickness of $500 - 750\mathring{A}$. A schematic of this step is shown in figure 4.1.

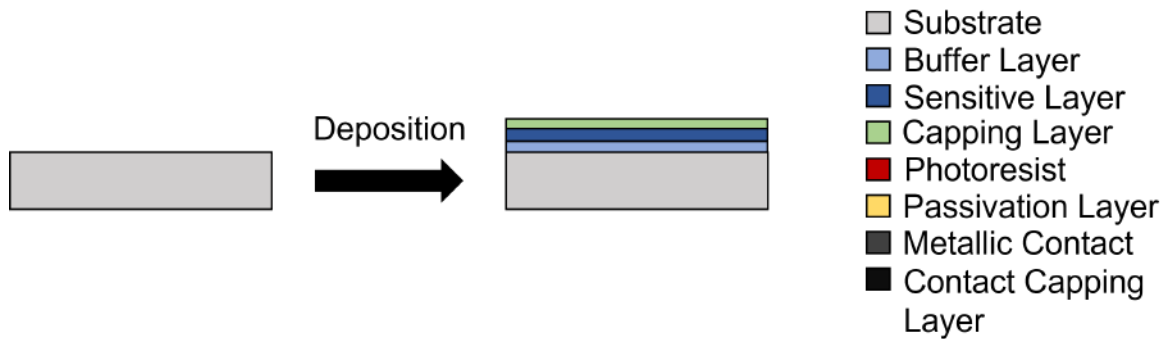

Figure 4.1: Schematic of the fabricated sample after the sensor deposition.

4.2.2 Sensor Definition - Lithography (DWL)

After depositing the three layers on the substrate, lithography follows, to define the shape of the sensors. Since the sensors will be define via etching, in this lithography an inverted mask is used, effectively covering that areas that will become the sensors. In the lithography step, several steps are included: Photo-Resist coating, exposure (DWL) and development. For all lithographies a positive PR was used, and for each one the samples were coated with a layer of $1.5\mu m$ of PR. The smallest features in this lithography are the meander strip width and the gap between strips, with sizes of $16-18\mu m$ and $3-5\mu m$ respectively.

This step was accomplished at INESC-MN using a Heidelberg DWL 2.0 lithography system, with a laser wavelength of $405nm$ and a minimum feature size of $0.8\mu m$. A schematic of this step is shown in figure 4.2.

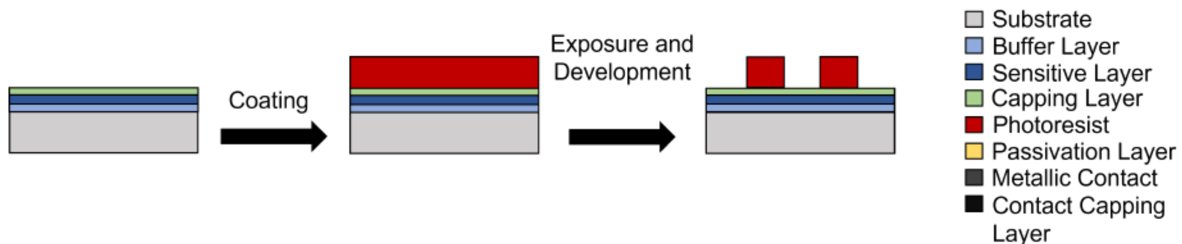

Figure 4.2: Schematic of the fabricated sample after the sensor definition lithography.

Subsequent lithographies require alignment marks, to ensure the masks are properly aligned. Figure 4.3 show an example of the first alignment mark used for the next lithographies.

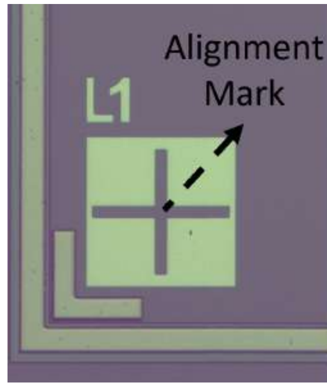

Figure 4.3: Example of an alignment mark used in lithographies after the first.

4.2.3 Material Removal (Sensor) - Ion Beam Milling

After creating the inverted mask the samples are submitted to etching via Ion Beam Milling, which removes all the undesired material, leaving the sensors with their shape well defined. This step was done in N3000 with a base pressure of $1 \times 10^{-7} Torr$. It is very important that in this step the etching is complete all the way down to the substrate, otherwise there could be short circuits in between sensors and even within each sensor, rendering the meander design useless, as parallels would be created, between the meanders and short circuits. To ensure the etching was done fully down to the substrate, electrical contact tests were done after IBM. After the etching is complete, the remaining PR is removed with the microstrip solution, in an ultrasound bath at $65°C$, leaving the sample ready for the next step. A schematic of this step is shown in figure 4.4 and a picture of the sample after milling is shown in figure 4.5.

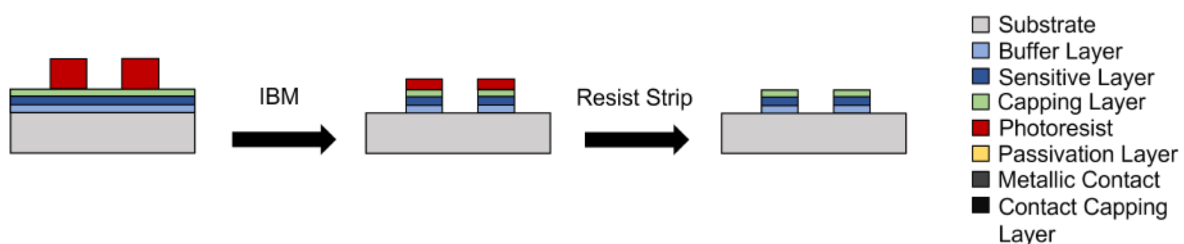

Figure 4.4: Schematic of the fabricated sample after the sensor level etching.

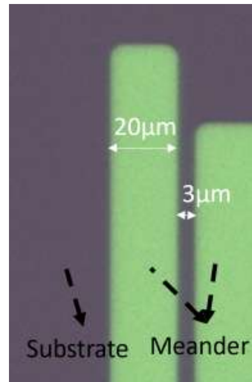

Figure 4.5: Picture of one of the test samples after milling. The picture shows one end of one of the meanders.

4.2.4 Passivation

Passivation refers to the deposition of an oxide over the existing structures. This layer of oxide protects the existing structures from oxidation and physical damage, in this case the sensors, and prevents electrical connections or short circuits where they are not wanted, which could happen when defining the electrical contacts; these electrical contacts should only connect to the edges of the meander structures of the sensors. This first passivation consists of a single layer of $2000\AA$ of SiO_2.
This step was undertaken in the Oxford equipment at INESC-MN. A schematic of this step is shown in figure 4.6.

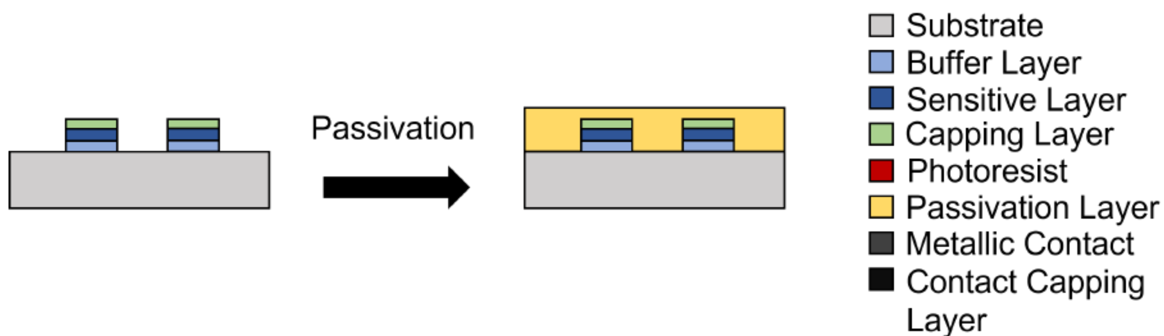

Figure 4.6: Schematic of the fabricated sample after the first passivation.

4.2.5 Vias Definition - Lithography (DWL)

Since there is now an oxide layer covering the sensors, and therefore impeding electrical access, vias have to opened to expose the ends of the meanders. Again with lithography these vias are defined, now with a non inverted mask. The vias typical size is 16-20$\times$16-20μm. A schematic of this step is shown in figure 4.7.

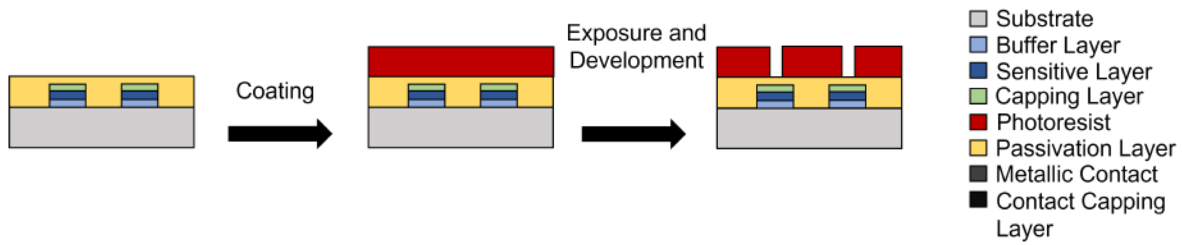

Figure 4.7: Schematic of the fabricated sample after the vias definition lithography.

4.2.6 Vias Opening - Reactive Ion Etching

To etch the passivation layer, Reactive Ion Etching can be recurred to, since SiO_2 reacts with CF_4, which is then the used gas in this process. This is highly advantageous because the passivation layer is quite thick, and RIE has a much higher etch rate than IBM, speeding up this step.
This step was done at INESC-MN using the machine LAM, with a CF_4 flux of $100sccm$, with an etch rate of $9.17\mathring{A}/s$. A schematic of this step is shown in figure 4.8. A picture showing an example of an open vias is show in figure 4.9

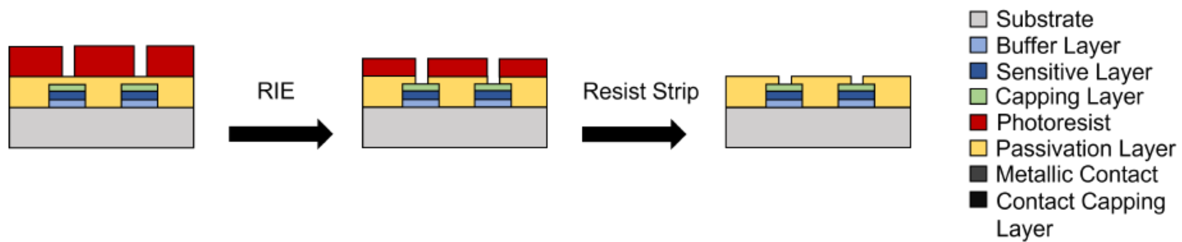

Figure 4.8: Schematic of the fabricated sample after the vias opening by RIE.

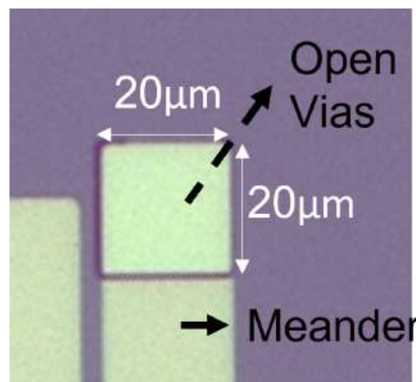

Figure 4.9: Picture of one of the test samples after RIE for vias opening.

4.2.7 Contact Definition - Lithography (DWL)

Since the metallic contacts are defined by lift-off, a lithography is required to create the mask over which the contacts will be deposited. For this step a non inverted mask is used again, leaving exposed the paths of the contacts. These contacts will establish two things: the connections between sensors to

form the two full bridges, and the pads that will be used to wire-bond the die to a PCB later on. For a lift-off, a pre-development is added prior to the exposure: it is the same as the development, but for a shorter duration. The purpose of this is to alter the profile of the PR, which will improve the process of lift-off, giving better edges to the metallic contacts. A schematic of this step is shown in figure 4.10.

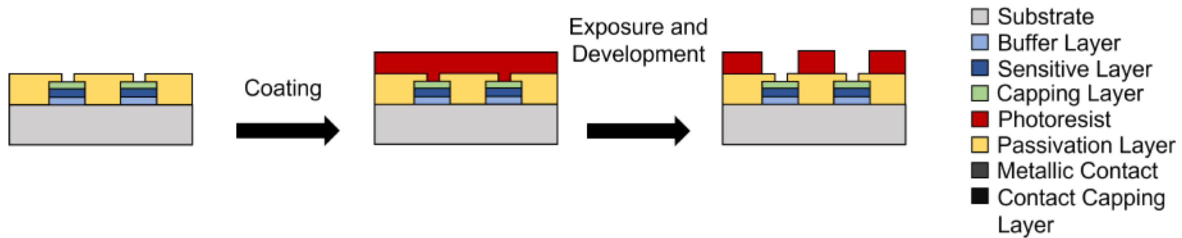

Figure 4.10: Schematic of the fabricated sample after the contact definition lithography.

4.2.8 Contact Deposition - Metallization

Having the mask ready for the lift-off process, the contact materials can now be deposited on the sample. The contacts were deposited through sputtering in the N7000 machine at INESC-MN. This machine has a central transfer chamber, and four modules, out of which three were used. In each module, one step was taken in the following order: soft sputter etch to clean the surface of the sample, deposition of Al, which is the main contact material and finally deposition of TiW(N_2). The layer of TiW(N_2) is very thin, and acts as a capping layer of the metallic contacts. It is a harder material than Al, so more durable, and nitrogen atoms (N) are mixed in this layer to help keep the contact free of oxidation. A total of $6000\AA$ of AlSiCu was deposited, with a cap of $150\AA$ of TiW(N_2). The contacts follow from the meanders in strips with $\approx 16\mu m$ of width, ending in pads with dimensions $\approx 140 \times 260\mu m$. This step was undertaken at INESC-MN using the machin N7000, with a $3mTorr$ working pressure. A schematic of this step is shown in figure 4.11.

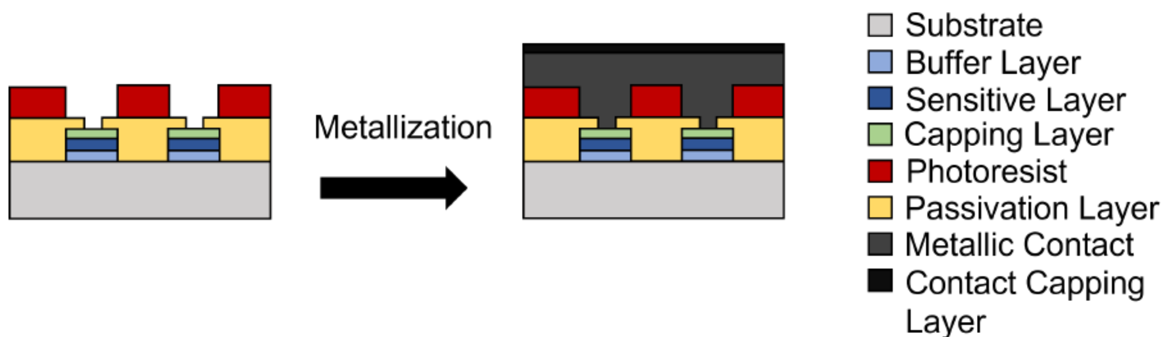

Figure 4.11: Schematic of the fabricated sample after the contact deposition.

4.2.9 Material Removal (Contacts) - Lift-off

To finalize the lift-off process, all that's left to do is remove the PR mask, and thus remove all the material deposited on top of it, leaving the contact material only in the areas of interest. This step is

similar to a regular resist strip, but usually takes more time for all of the PR to be removed. A schematic of this step is shown in figure 4.12. Figure 4.13 shows a picture of one contacts defined after lift-off, and their proper alignment with the vias that were previously opened, in order to establish electrical contact with the meanders.

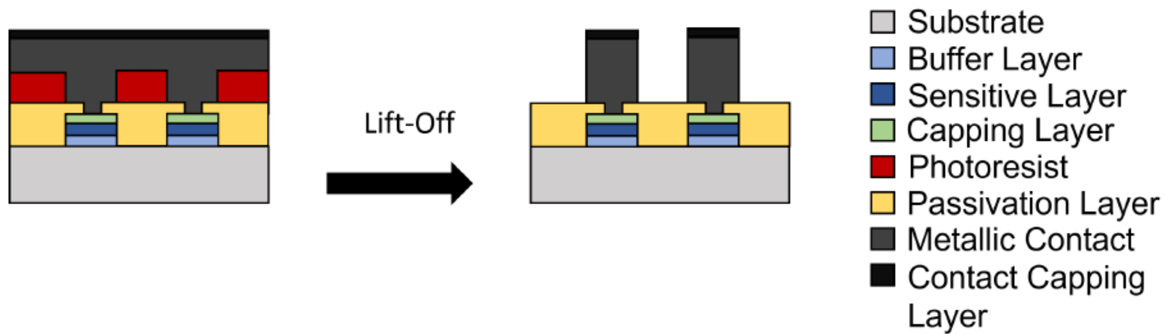

Figure 4.12: Schematic of the fabricated sample after the contact lift-off.

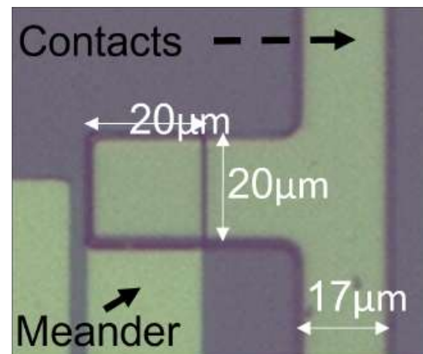

Figure 4.13: Picture of one of the test samples after contact lift-off. Notice how the electrical contacts are aligned with the vias that were previously opened, ensuring there is electrical connection to the meanders.

4.2.10 Passivation

One last passivation is done, now to protect the whole composition of sensors in full bridges and the contacts. Exactly the same as the first passivation, done by sputtering, but now a $1500\AA$ layer. A schematic of this step is shown in figure 4.14. Figure 4.15 shows a picture of one contact pad defined after lift-off, covered with the second passivation layer.

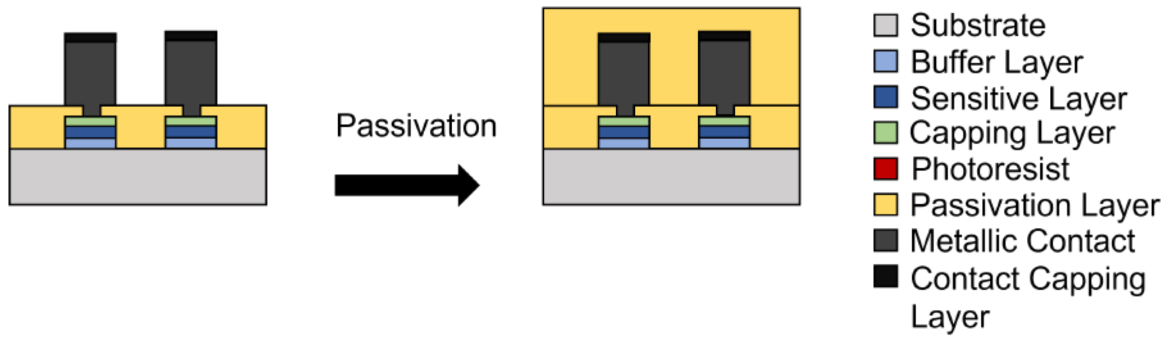

Figure 4.14: Schematic of the fabricated sample after the final passivation.

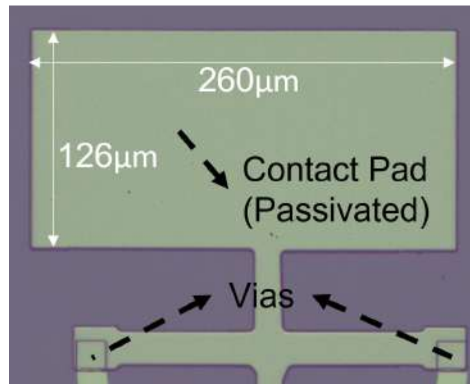

Figure 4.15: Picture of one of the test samples after the second passivation.

4.2.11 Pads Definition - Lithography

The final step of fabrication is exposing the pads used for wire-bonding. it is the same process as opening the vias through the first passivation, down to the ends of the sensors' meanders, starting with the lithography where a non inverted mask is transferred to the PR. The opening to the pads had dimensions $110 \times 240\mu m$.
A schematic of this step is shown in figure 4.16.

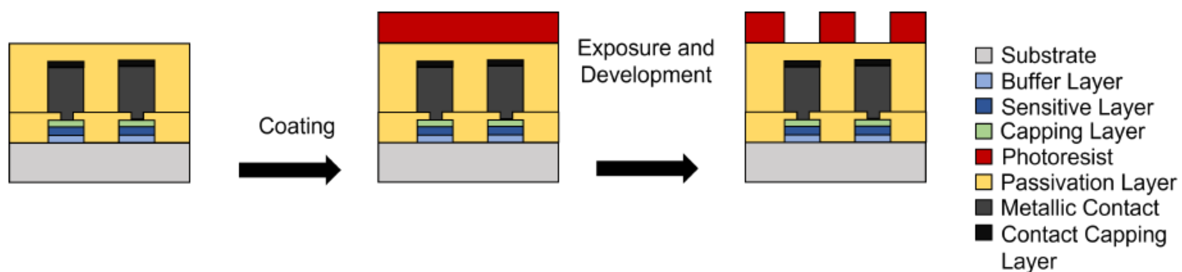

Figure 4.16: Schematic of the fabricated sample after the pads opening lithography.

4.2.12 Pads Opening - Reactive Ion Etching

With the mask created, the sample moves on to RIE. A path to the pads is opened, and after an ultrasound bath in microstrip to remove the remaining PR, the sensors are ready. A schematic of this

step is shown in figure 4.17. Figure 4.18 show a picture of the open pads after RIE.

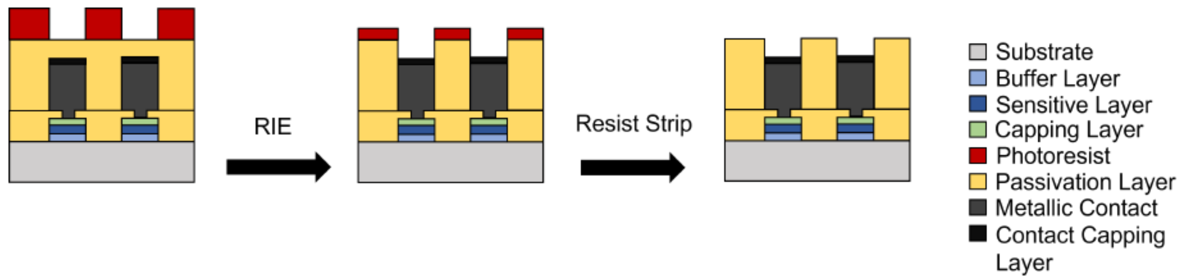

Figure 4.17: Schematic of the fabricated sample after the pads opening RIE.

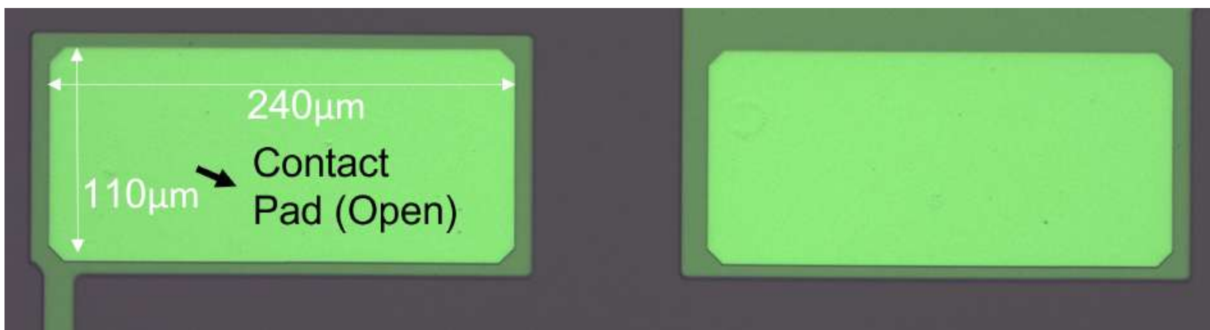

Figure 4.18: Picture of one of the test samples after RIE for pad opening.

4.2.13 Magnetic Annealing - Optional

This step of fabrication is optional, and was a subject of study during this dissertation. The fabricated samples were characterized before and after annealing to verify the effects of this step in the sensor's properties.

4.3 Possible Issues - DWL vs Hard Mask: Uniformity

In parallel with the test samples, full six inch wafers were also being produced at INESC-MN, using the Ta(50) buffer layer. Some wafers were fabricated using the DWL lithography technique in all the required lithographies, while in some other wafers, the first lithography was done using a hard mask. The first lithography is when the sensor design is transferred to the wafer, being the most crucial lithography. With DWL lithography, some flaws can be identified through optical inspection, regarding the sensor design, where it may not maintain a constant width for example. An example of one such found flaw is given in figure 4.19:

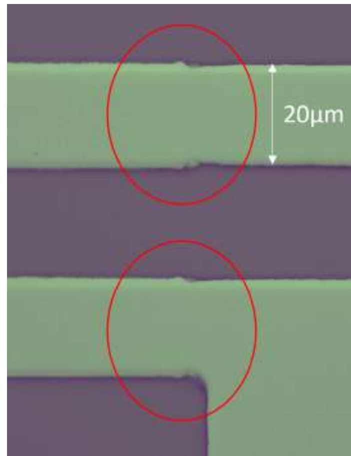

Figure 4.19: Example of a sensor definition flaw resulting from the DWL lithography step, observed on the sample Ta(50) during optical inspection after the contact definition via lift-off.

Since the sensors being studied and the fabrication process will ultimately move into a mass production stage, where uniformity is of great importance, this case study of DWL vs Hard Mask lithography is crucial to understand if it is worth, or not, investing in a hard mask to reach a higher uniformity. For these measurements, the auto-prober is used, since for proper statistics and greater area coverage of the wafer a large number of measurements are required.

Chapter 5

Results and analysis

5.1 X-Ray diffraction

The x-ray diffraction measurements give insight on the crystalline structure of the NiFe layer. It will be possible to evaluate the quality of growth of this film on the different buffers, and then the consequence of annealing. NiFe has a *fcc* structure, and the peak that is studied here corresponds to the diffraction on the [111] plane. The *fcc* structure is represented in figure 5.1, with one of the [111] planes highlighted:

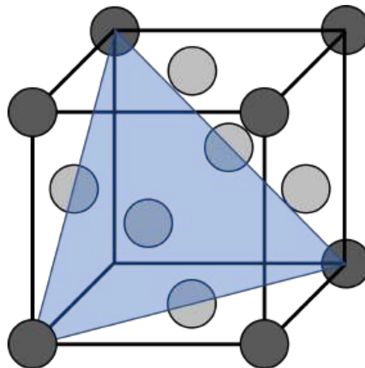

Figure 5.1: Representation of the *fcc* structure, highlighting one of the [111] planes.

As mentioned in chapter 4, four unpatterned samples were processed to be used in the crystallographic study. The objective was to determine the effect of annealing on the grain size and inter-planar distance. For that purpose, the samples were submitted to several annealings, all at the same temperature of $350°C$, for different periods of time. The X-ray diffraction measurements were done between annealings. A total of four annealings were made, two of one hour, one of three hours and another of five hours, totalling up to ten cumulative hours of annealing.

Table 5.1: Step and cumulative duration of the annealings for the unpatterned samples.

Time	Annealing 1	Annealing 2	Annealing 3	Annealing 4
Step (hours)	1	1	3	5
Cumulative (hours)	1	2	5	10

The measurements were taken between $2\theta = 18°$ and $2\theta = 23°$, with a $0.02°$ step and 5 seconds of acquisition per point, since the peak was found between $2\theta = 20°$ and $2\theta = 21°$ in a longer sweep with larger step.

5.1.1 Diffraction peaks

In figures 5.2, 5.3, 5.4 and 5.5, the detected diffraction peaks are plotted for samples Ta(50), NiFeCr(50), NiFeCr(100) and NiFeCr(150), respectively. This peak occurred at the expected angle of the peak generated by a NiFe layer, so the effect of the buffer in this layer can effectively be observed.

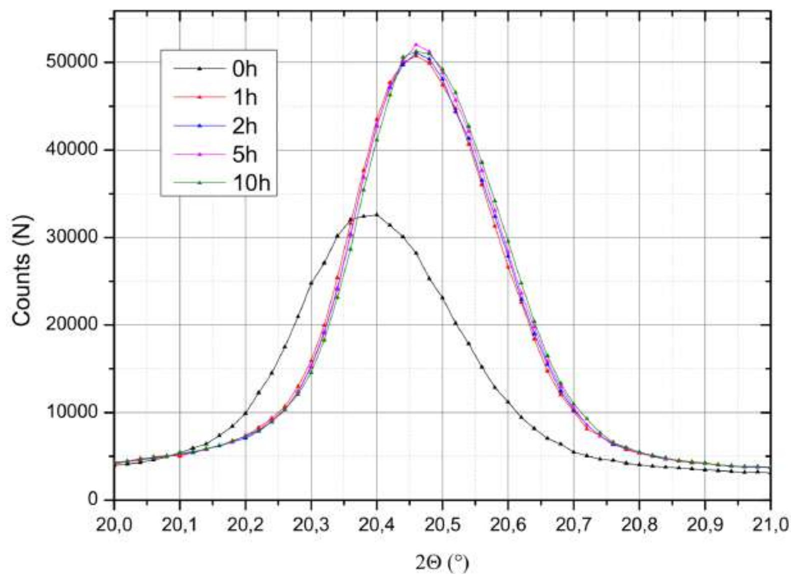

Figure 5.2: Evolution of X-ray diffraction peaks of sample Ta(50) with cumulative annealing time.

On sample Ta(50), even before annealing the NiFe peak can be observed, meaning that the Ta buffer promotes a good crystalline growth on the NiFe film without additional aid from the annealing. After annealing, two things are noticeable: the peak moved, occurring now at a slightly higher angle, and there are no significant differences after the first annealing.

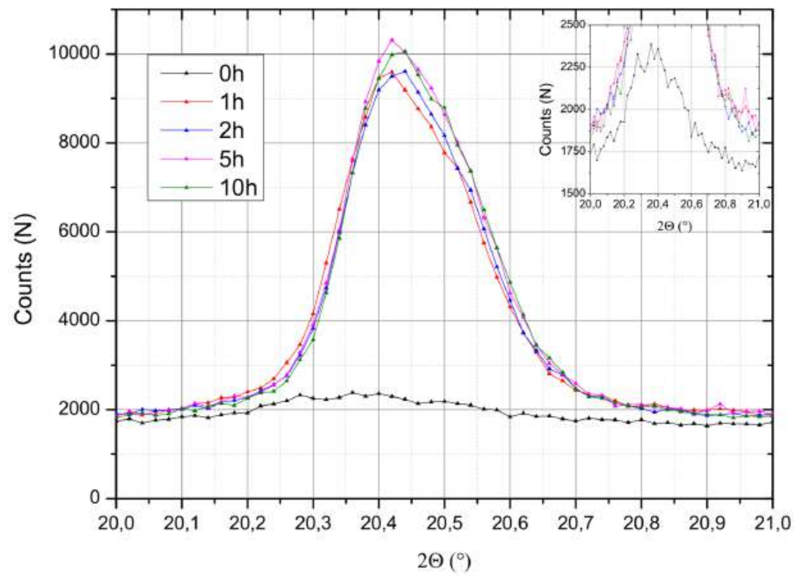

Figure 5.3: Evolution of X-ray diffraction peaks of sample NiFeCr(50) with cumulative annealing time.

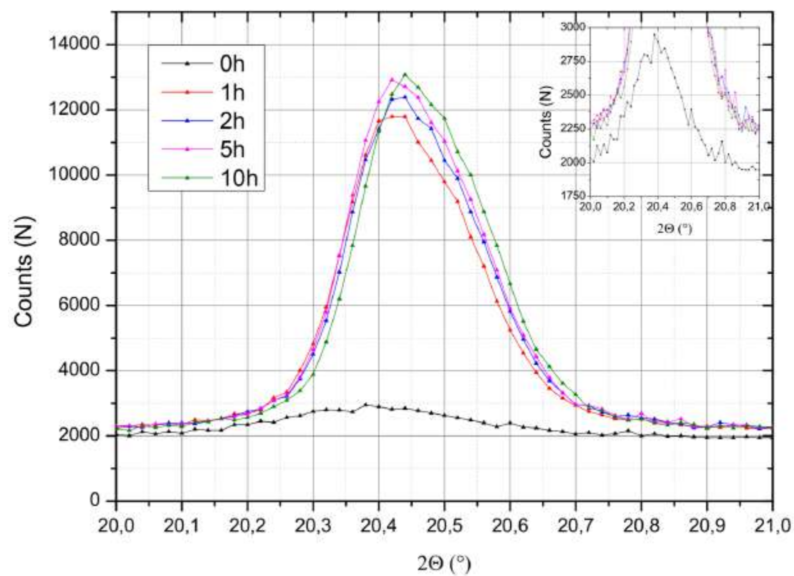

Figure 5.4: Evolution of X-ray diffraction peaks of sample NiFeCr(100) with cumulative annealing time.

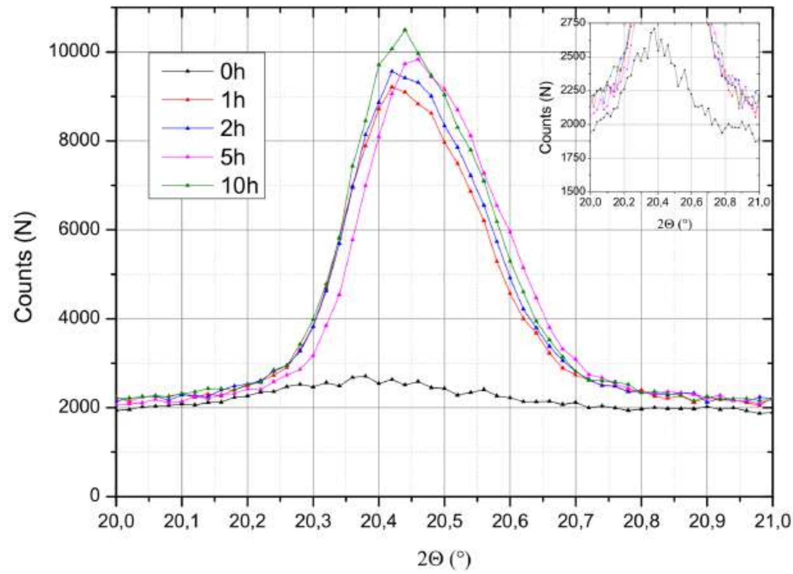

Figure 5.5: Evolution of X-ray diffraction peaks of sample NiFeCr(150) with cumulative annealing time.

The NiFeCr buffer samples show very similar results between them, and similar even to the Ta(50) sample, although a major difference can be seen in the results prior to annealing. The peak prior to annealing for the NiFeCr samples is very poorly defined, which shows that the NiFeCr does not promote a good crystalline growth of the NiFe layer, at least without annealing. However, as verified on the Ta(50) sample, there is a significant improvement, even more so for the samples with the NiFeCr buffer, after annealing. After the first annealing the peak is better defined and it also dislocates to higher angles. Just like the Ta(50) sample as well, there are no significant changes after the first hour of annealing.

The FWHM and angle at which the peak occurs were extracted from the curve by fitting a Gaussian curve to the data, from which the peak position and the FWHM of the curves was extracted. Figure 5.6 summarizes those results as a function of cumulative annealing time.

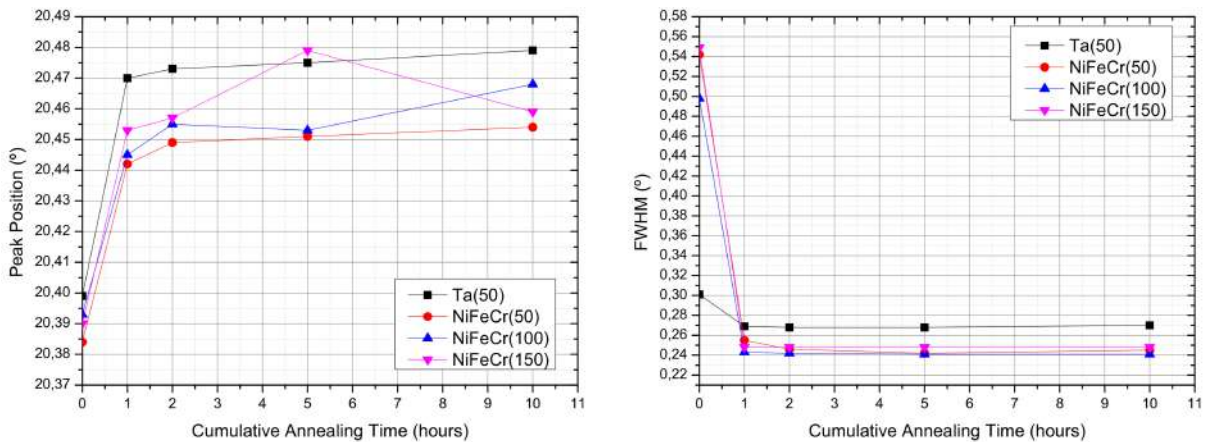

(a) Evolution of X-ray diffraction peak position of all samples with cumulative annealing time.

(b) Evolution of X-ray diffraction peak FWHM of all samples with cumulative annealing time.

Figure 5.6: Evolution of the peaks' positions and FWHM with cumulative annealing time, for all samples.

As expected, both properties change after one hour of annealing, but remain relatively similar throughout the remainder of the annealing time. The peak moved to a slightly higher angle, a difference of less than $0.1°$, however. The behaviour was the same across all samples.
The FWHM of the peaks also only changed after the first hour of annealing, after the next annealings no change was verified. The Ta(50) exhibits a slight decrease from $\approx 0.3°$ to $\approx 0.27°$, which indicates the peak is slightly better defined. On the NiFeCr buffer samples on the other hand, the change in FWHM is flagrant: a much bigger change, decreasing from $\approx 0.50 - 0.54°$ to $\approx 0.24°$, a larger variation than that observed on the Ta(50) sample, which was nonetheless expected from observation of the plotted peaks in figures 5.3, 5.4 and 5.5. The final values of FWHM of the NiFeCr samples are even below than the value of the Ta(50) sample, the NiFeCr samples benefit more from annealing. Across the different NiFeCr samples the results are very similar, therefore independent of the buffer thickness.

5.1.2 Grain size

Grain size was calculated using 3.2, with the relevant parameters extracted from the diffraction peaks. Figure 5.7 shows the evolution of the grain size.

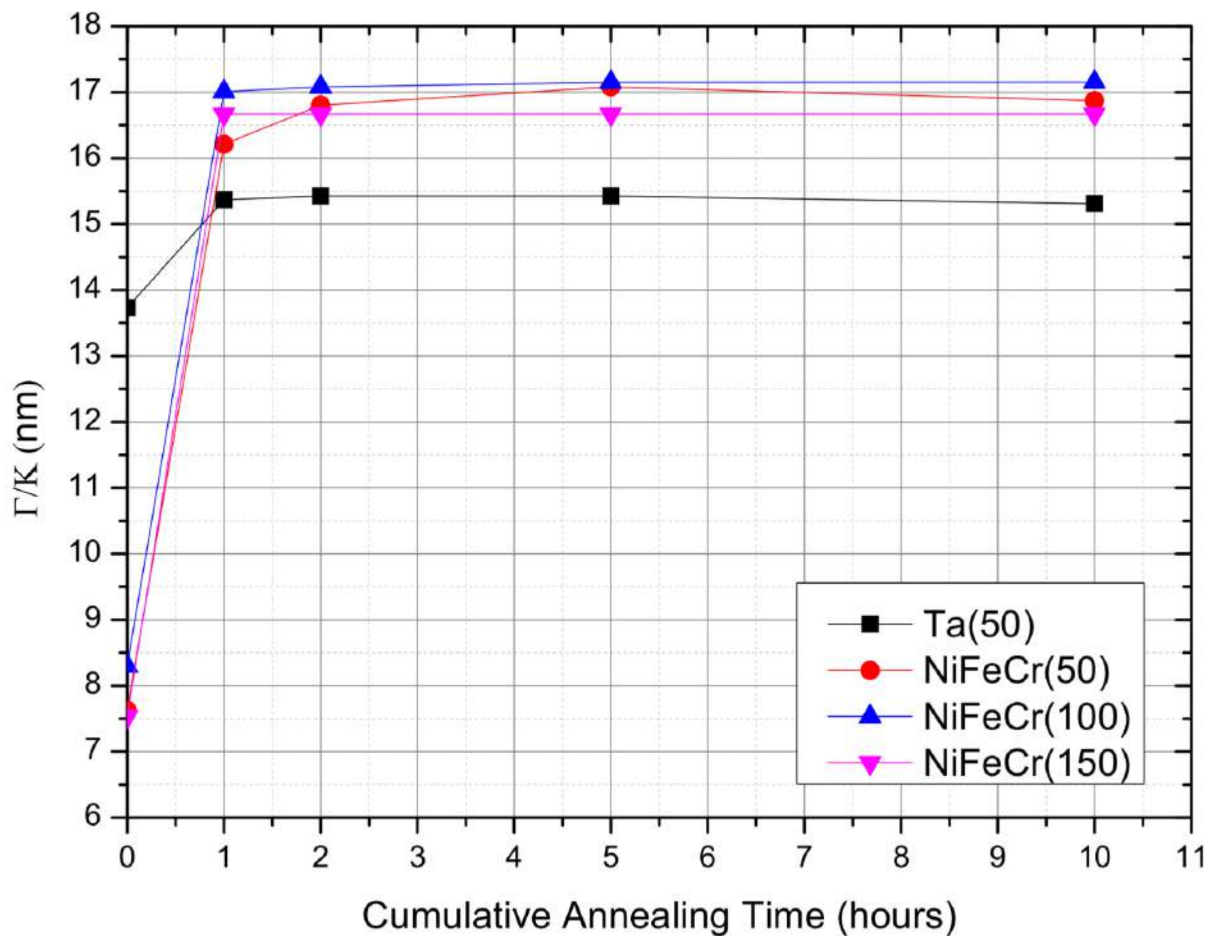

Figure 5.7: Evolution of the grain size of all samples with cumulative annealing time.

Given that a decrease in the FWHM of the peaks was detected, an increase in grain size was already

expected. It was, nonetheless, expected even prior to the measurements given the nature of the annealing process. What is important to note here is that, despite all samples displaying the same behaviour, the grain size increase is much larger in the NiFeCr samples, approximately doubling grain size after one hour of annealing, surpassing the Ta(50) sample in this parameter. The result is independent of the buffer layer thickness, as all NiFeCr samples have similar results. Because the interest here is to evaluate the evolution of the grain size, and not necessarily its actual size, the results presented were calculated without the material dependent constant K.

5.1.3 Inter-planar distance

From the displacement of the peaks' position we can also discern some information about the evolution of the inter-planar distance, d. However, the variation of this quantity was very small, so the annealing had in fact little impact on the inter-planar distance, resulting in a variation of the order of the tenth of the pm. Figure 5.8 shows the evolution of the inter-planar distance.

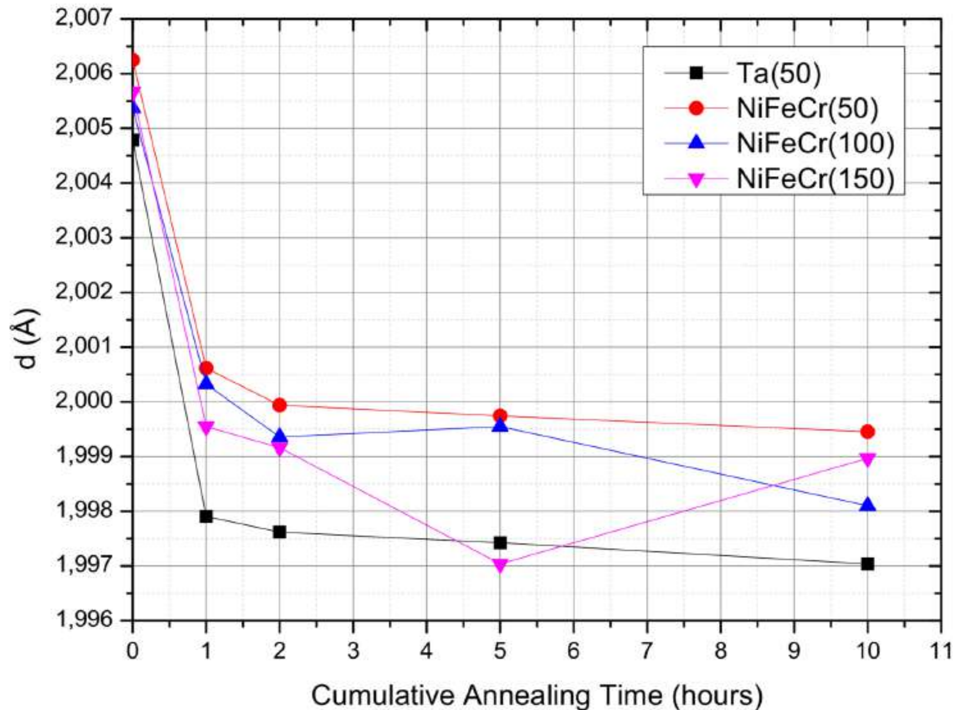

Figure 5.8: Evolution of the inter-planar distance of all samples with cumulative annealing time.

5.1.4 Summary

Overall, all samples show the same behaviour, with improvements in their crystal structure as a consequence of the magnetic annealing. Ta(50) sample shows the smallest improvements, while the NiFeCr show large improvements in peak definition and consequently in grain size, effectively doubling grain size. The inter-planar distance decreased ever so slightly on all samples.

Also worth noting is that one hour of annealing at $350°$C is enough to produce these results, longer annealing times show no benefit. The data is summarized on table 5.2:

Table 5.2: X-Ray diffraction results of samples Ta(50), NiFeCr(50), NiFeCr(100) and NiFeCr(150).

Cumulative annealing time (hours)	Sample							
	Ta(50)		NiFeCr(50)		NiFeCr(100)		NiFeCr(150)	
	$\frac{\tau}{K}$ (nm)	d (Å)	$\frac{\tau}{K}$ (nm)	d (Å)	$\frac{\tau}{K}$ (nm)	d (Å)	$\frac{\tau}{K}$ (nm)	d (Å)
0	13.73	0.2004	7.63	0.2006	8.30	0.2005	7.53	0.2001
1	15.37	0.1998	16.21	0.2001	17.01	0.2000	16.67	0.2000
2	15.42	0.1998	16.80	0.2000	17.08	0.1999	16.67	0.1999
5	15.42	0.1997	17.08	0.2000	17.15	0.1999	16.67	0.1997
10	15.31	0.1997	16.87	0.1999	17.15	0.1998	16.67	0.1999

5.2 Transfer Curves

The masks used in fabrication contained seven different designs, and those seven different designs ended up being measured. However, there were no differences between designs when it comes to the effect of buffer layer composition and thickness, as well as the annealing. So, the scope is narrowed here to a single design, which is enough to take the desired conclusions regarding the sensor stack.

5.2.1 Manual Measurement Setup

The Manual Measurement Setup was used to study the response of the device to a magnetic field applied in the direction of the magnetic hard axis. The conditions used for the measurements are summarized in table 5.3.

Table 5.3: Parameters used for the 140Oe Setup transfer curve measurements for samples Ta(50), NiFeCr(50), NiFeCr(100), NiFeCr(150).

Setup	I_{bias} (μA)	Magnetic Field Interval (Oe)	Magnetic Field Step (Oe)
140Oe	10	[-141;-25]	10
		[-25;-5]	0.1
		[-5;5]	1
		[5;25]	0.1
		[25;141]	10

The small step in the magnetic field intervals [-25;-5](Oe) and [5;25](Oe) is required for the measurement to be precise enough to allow the calculation of the coercivity, since the expected values fall below 1Oe. The coercivity was calculated in several points within this range, in both the negative and positive branches and then averaged. It is important to note that the MR ratio comes mostly from the NiFe layer, not the buffer or cap layers. With the transfer curves of the different samples, what is being measured is

the behaviour of the NiFe layer and the effects the different buffer layers have on it.

The transfer curves of samples Ta(50), NiFeCr(50), NiFeCr(100) and NiFeCr(150) were taken before and after annealing, in order to determine the effects of this process. Due to the results from the x-ray diffraction analysis (see section 5.1), the samples were annealed for two hours, which is enough time for the annealing to have its full effect, structurally, on the samples; the effects of annealing on the magnetic response remain unknown at this point. But a first comparison between samples should be drawn, even before annealing. Figure 5.9 shows the plotted data of the MR transfer curves of the four mentioned samples, with no annealing. The results of this measurement are presented on table 5.4.

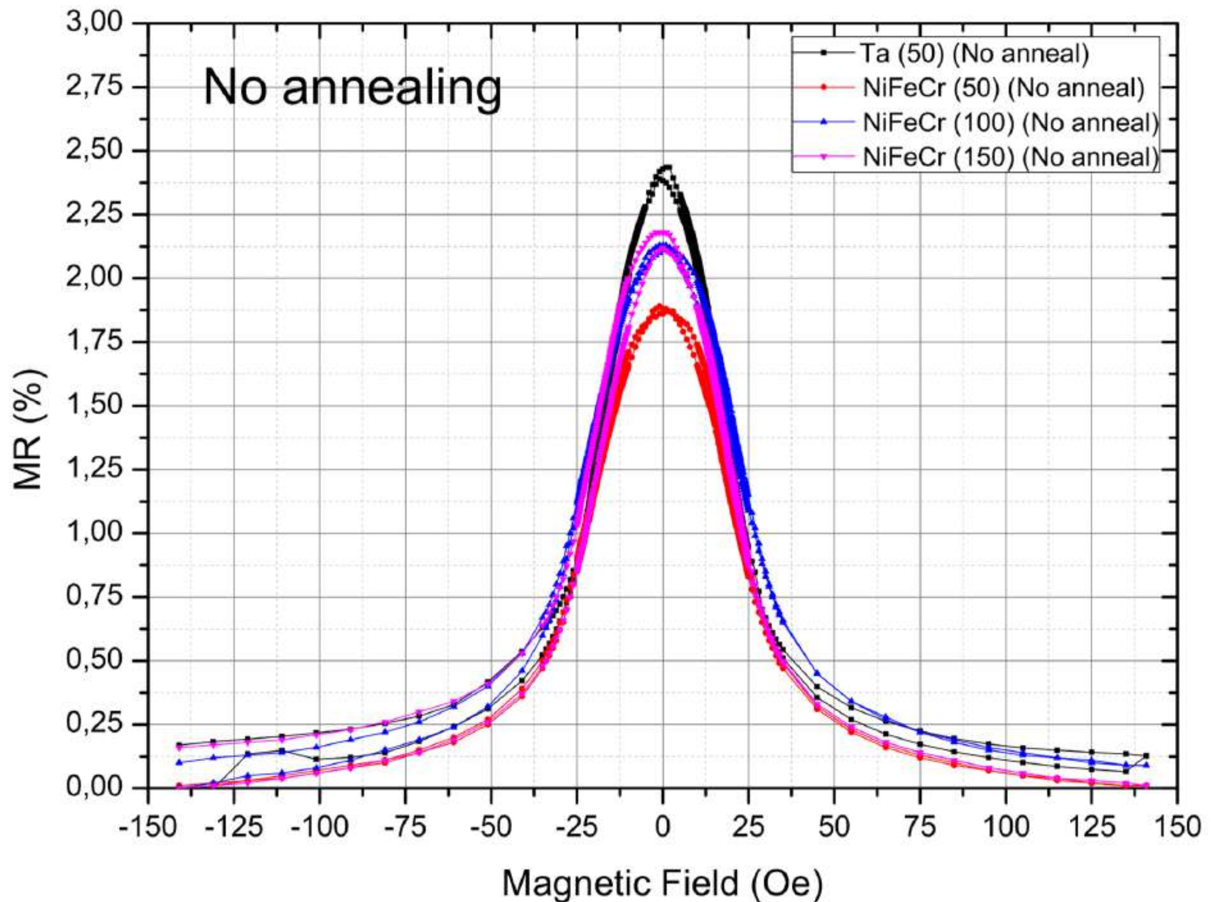

Figure 5.9: Transfer curves of samples Ta(50), NiFeCr(50), NiFeCr(100) and NiFeCr(150) with no annealing.

Table 5.4: Transfer curve results of samples Ta(50), NiFeCr(50), NiFeCr(100) and NiFeCr(150).

Sample	MR(%)	$R_{min}(\Omega)$	H_c(Oe)	FWHM(Oe)
Ta(50)	2.65	1044.92	0.60	43.68
NiFeCr(50)	1.89	1053.00	1.02	47.00
NiFeCr(100)	2.13	899.36	0.94	49.00
NiFeCr(150)	2.18	973.95	1.55	44.63

These results show that without annealing, Ta seems to be the best buffer material, exhibiting the highest MR and lowest coercivity. The differences in resistance come mostly from the total stack thickness, since Ta and NiFeCr have similar resistivity, hence the lower resistance in sample NiFeCr(100), where the buffer, sensor and capping layer comprise a stack of 550Å instead of the 500Å of the other samples. The FWHM of the curves, parameter used here to analyse the saturation of the devices, shows little difference between samples. These results are the baseline to determine the effects of annealing. After annealing the samples were measured again using the same parameters. Figure 5.10 shows the transfer curves of each sample before and after annealing, table 5.5 shows the results of the measurements and figure 5.11 shows the transfer curves of annealed samples .

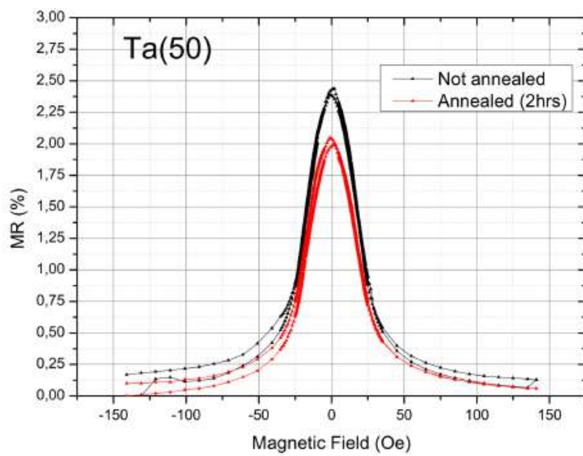

(a) Transfer curve of sample Ta(50) before and after annealing.

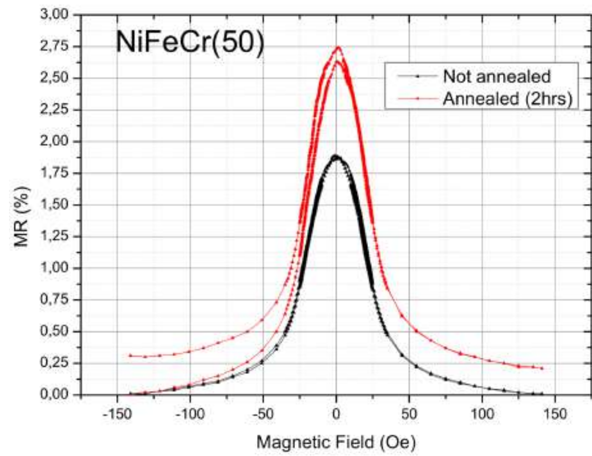

(b) Transfer curve of sample NiFeCr(50) before and after annealing.

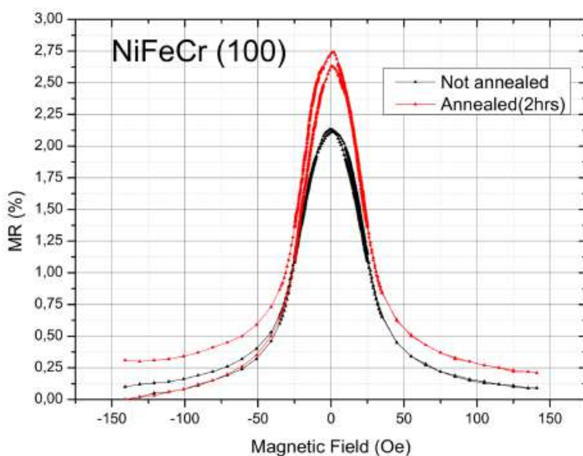

(c) Transfer curve of sample NiFeCr(100) before and after annealing.

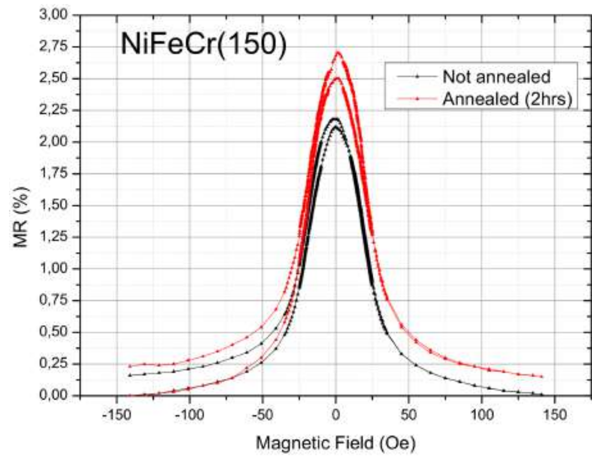

(d) Transfer curve of sample NiFeCr(150) before and after annealing.

Figure 5.10: Transfer curves of the four samples before and after annealing at 350°C for 2 hours.

Table 5.5: Transfer curve results of samples Ta(50), NiFeCr(50), NiFeCr(100) and NiFeCr(150).

Sample	MR(%)	$R_{min}(\Omega)$	H_c(Oe)	FWHM(Oe)
Ta(50)	2.05	1229.32	0.56	39.98
NiFeCr(50)	2.74	872.61	0.36	47.2
NiFeCr(100)	2.69	768.62	0.66	48.8
NiFeCr(150)	2.69	769.92	0.91	44.00

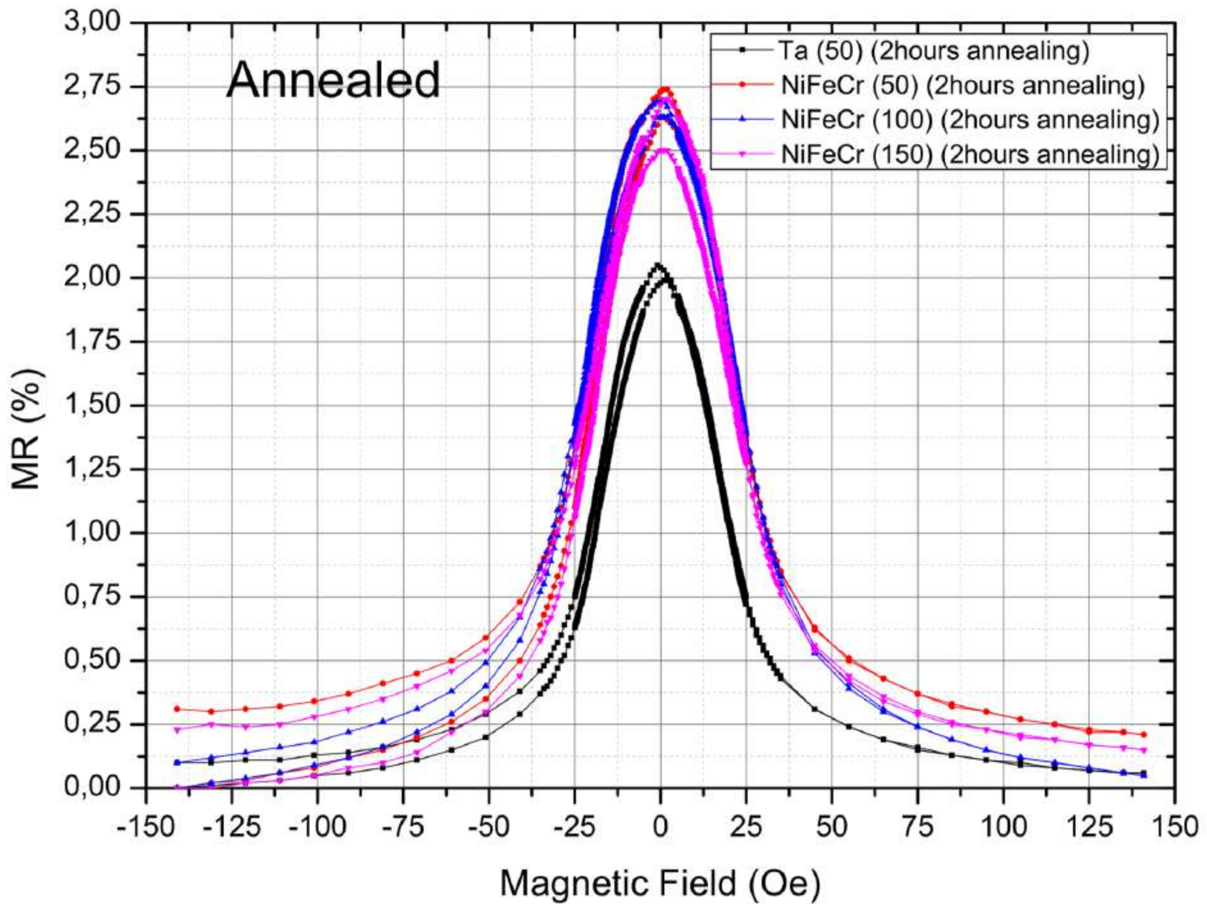

Figure 5.11: Transfer curves of samples Ta(50), NiFeCr(50), NiFeCr(100) and NiFeCr(150) with no annealing at 350°C for two hours.

The consequence of annealing (under the specified conditions) on the sensors is very interesting, as it is completely opposite on the two different buffer materials, concerning MR ratios. The Ta(50) sample suffers a reduction of MR, down to 2%, where as the NiFeCr have their MR ratios increase up to around 2.75% in all three samples. In terms of resistance, the same opposition of behaviours can be found: on the Ta(50) there is an increase in the resistance, while in the NiFeCr the resistance is lowered. In terms of coercivity, all samples improve with annealing, with the best result being obtained on the NiFeCr(50) sample, with $H_c = 0.36Oe$. The FWHM exhibits no significant change.

The other two fabricated samples mentioned in section 4.1.2, Ta(30)+NiFeCr(300) and NiFeCr(300),

were also tested, but only after annealing and with a duration of thirty minutes. These samples can be compared with the first samples, with their transfer curves on figure 5.12 and results on table 5.6.

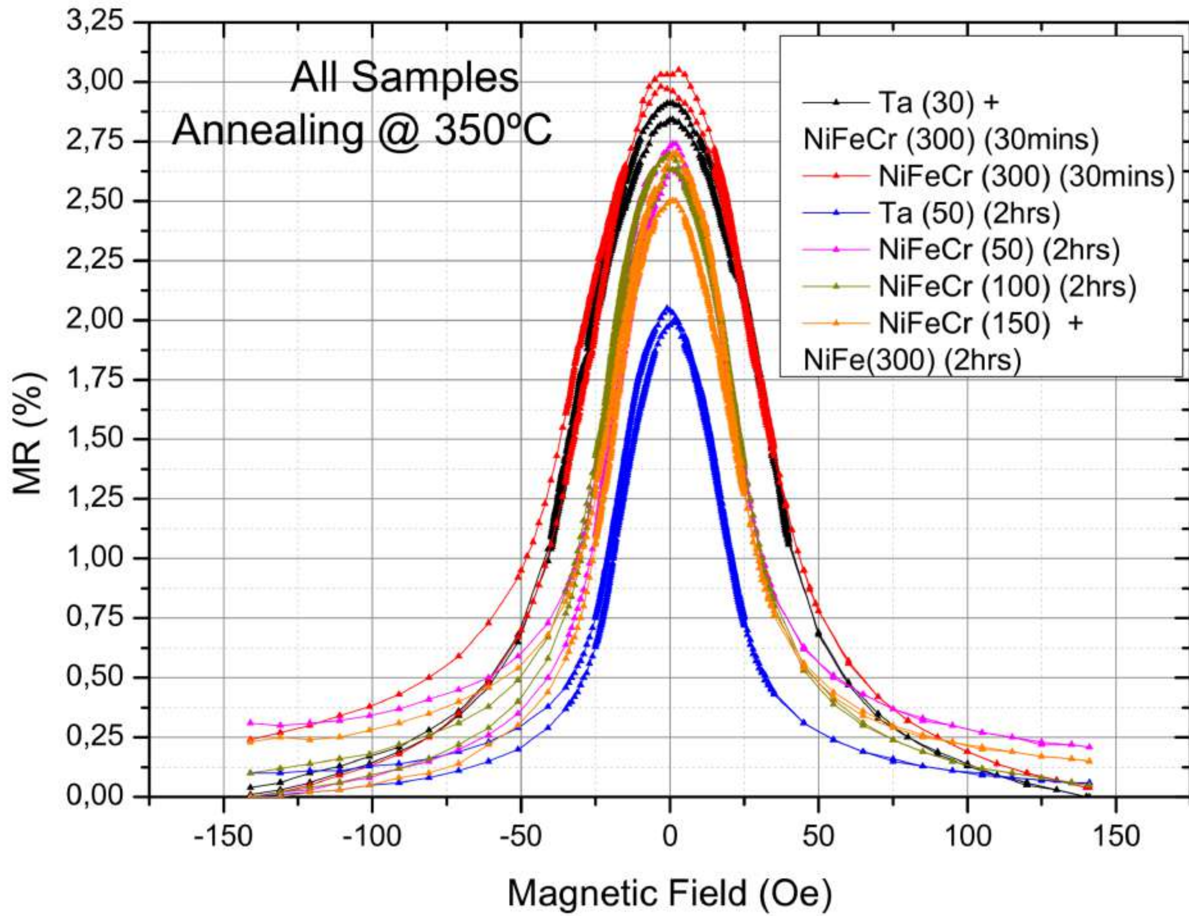

Figure 5.12: Transfer curves of samples Ta(50), NiFeCr(50), NiFeCr(100) and NiFeCr(150) with annealing at 350°C for two hours and of samples Ta(30)+NiFeCr(300) and NiFeCr(300) with annealing at 350°C for thrity minutes.

Table 5.6: Transfer curve results of samples Ta(50), NiFeCr(50), NiFeCr(100) and NiFeCr(150).

Sample	MR(%)	$R_{min}(\Omega)$	H_c(Oe)	FWHM(Oe)
Ta(50)	2.05	1229.32	0.56	39.98
NiFeCr(50)	2.74	872.61	0.36	47.20
NiFeCr(100)	2.69	768.62	0.66	48.8
NiFeCr(150)	2.67	769.92	0.91	44.00
Ta(30) + NiFeCr(300)	2.88	520.90	0.55	68.40
NiFeCr(300)	3.04	511.80	0.66	65.90

Since these last two samples are much thicker, approximately 250Å thicker, it is already expected that they have lower resistances, which was verified in the measurements. In terms of MR, there is

a significant increase, with sample NiFeCr(300) surpassing a 3% MR ratio. The coercivity remains low, around the desired $0.5Oe$ value. However, the main difference regarding the previous samples is the increase of the FWHM of the transfer curves. This parameter, relating to the saturation of the device, indicates that an higher field is required to saturate the devices. Ta as a buffer material seems to reduce this quantity, presenting the lowest value at $39.98Oe$. When examining the NiFeCr samples, there is an increase from sample NiFeCr(50) to sample NiFeCr(100), due to the increased thickness. In sample NiFeCr(150), FWHM decreases because this sample has a thinner NiFe layer (100Å thinner). With the big increase in buffer thickness in samples Ta(30)+NiFeCr(300) and NiFeCr(300), it becomes again clear that the thickness is the reason for the FWHM increase. The impact of this change will be discussed in section 5.4, as it will have direct consequences on the performance of the sensors in the linear positioning system. These results are summarized in figures 5.13 to 5.16.

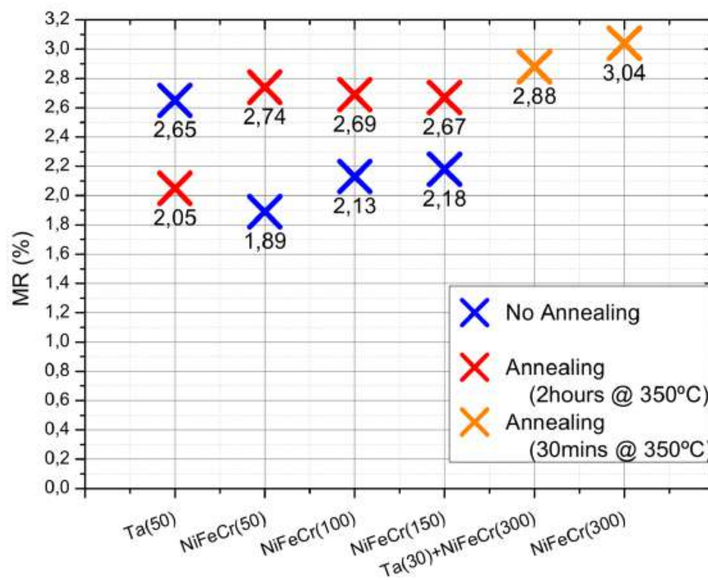

Figure 5.13: MR measurement results.

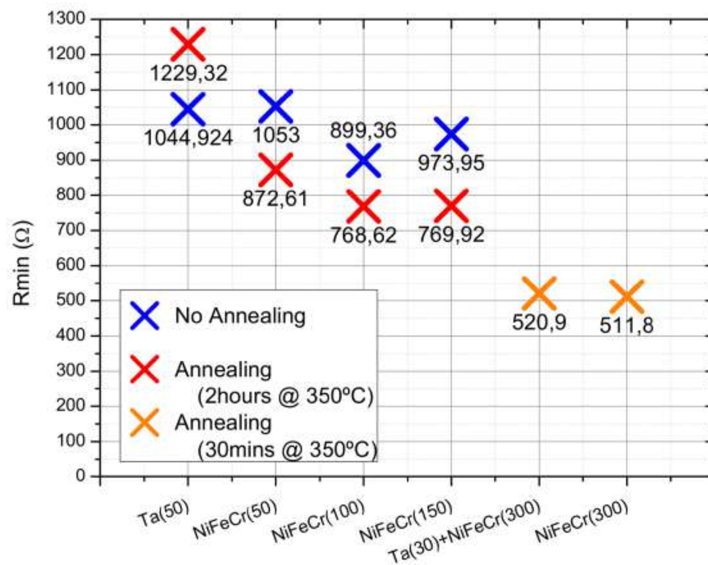

Figure 5.14: R_{min} measurement results.

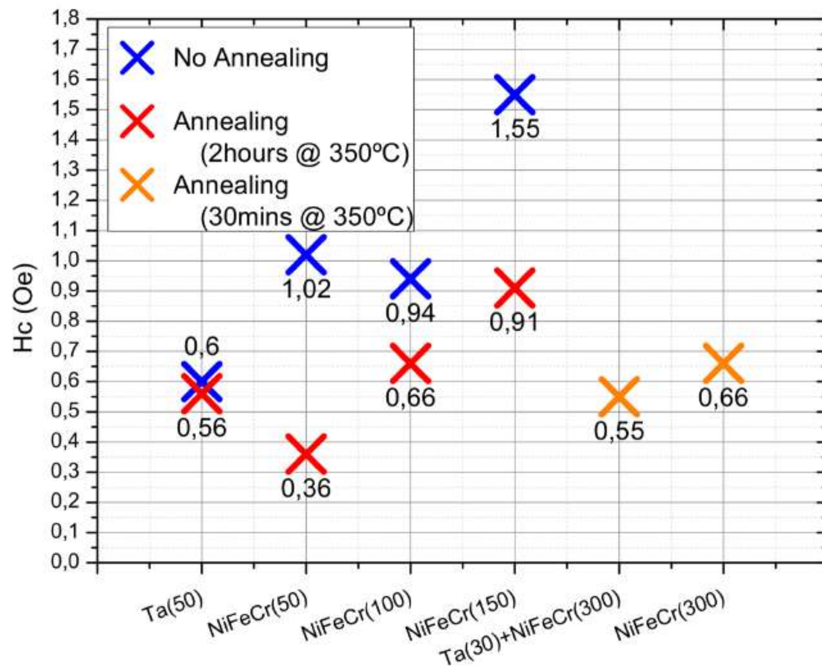

Figure 5.15: H_c measurement results.

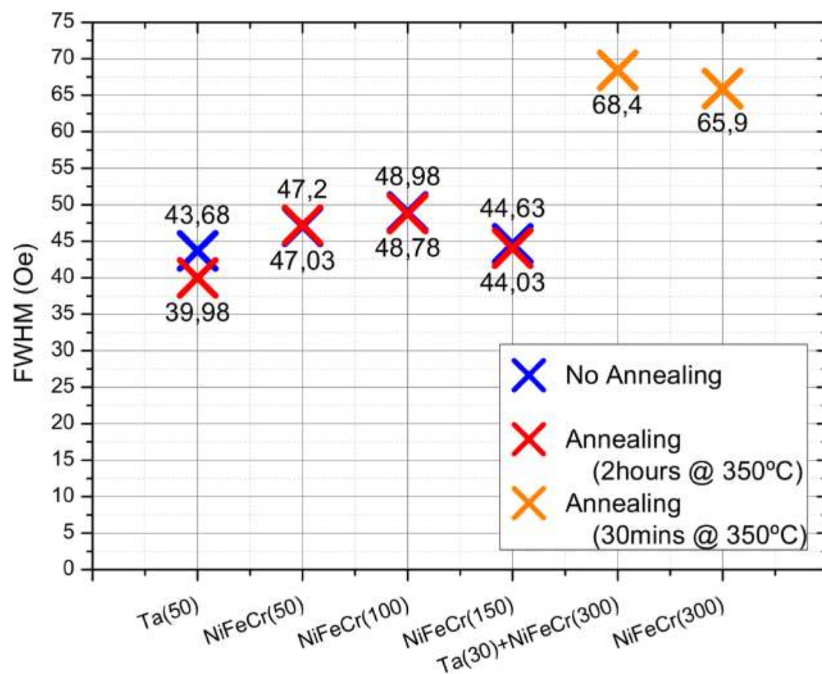

Figure 5.16: FWHM measurement results.

5.3 DWL vs Hard Mask - Uniformity

Two six inch wafers were produced with the Ta(50) sample composition, where the sensor definition lithography was done with DWL in one of the wafers, and with a hard mask in the other. The transfer curves on both samples were measured on the auto-prober, using the conditions given on table 5.7:

Table 5.7: Parameters used in the auto-prober setup transfer curve measurements for the 6 inch wafers.

Setup	I_{bias} (μA)	Magnetic Field Interval (Oe)	Magnetic Field Step (Oe)
Auto-prober	10	[-120;-45]	37.5
		[-45;45]	15
		[45;120]	37.5

A much larger step for the magnetic field was used due to the large number of measurements taken, so as to save time, and because the parameter being studied is the resistance of the sensors. The large 15Oe step in the interval [-45;45]Oe might be too large to extract a precise value of MR. However, these measurements aim only to study the uniformity, and since the same conditions are used for all measurements, conclusions about uniformity can still be taken. Again, for scope narrowing, although there are several different designs present in the used masks, the results refer to a single design, same as in previous sections. Some conditions were applied to the data to exclude non functional devices from the statistics, as well as isolated cases of functional devices of which the resistance values differed too much from the average, indicating that they had some form of defect:

- Transfer curve crosses half maximum value four times. This is the main condition for a device to be functional;
- 1000 $< R_{min} <$ 1200 (Ω). This condition removes isolated cases of devices with parameters too different from the expected, but still considered functional by the previous condition.
- The percentage of devices that fall under these restrictions is the yield.

The statistics on minimum resistance and MR ratio are presented on table 5.8, and histograms of the measured R_{min} and MR ratio are present in figure 5.17.

Table 5.8: Parameters used in the auto-prober setup transfer curve measurements for the 6 inch wafers.

				MR(%)		$R_{min}(\Omega)$	
Wafer Size	Sensor Lithography	Total measurements	Yield(%)	Mean	σ	Mean	σ
6”	DWL	34	97.06	2.27	0.02	1120.26	18.57
6”	Hard Mask	132	96.97	2.35	0.04	1061.97	12.84

Even though the total number of measurements is quite different, the yield is very similar, so the number of isolated cases of functional sensors with resistance very far from the average is expected to scale with the number of measurements. The fabrication process using the hard mask for the first lithography shows a significant improvement in the resistance dispersion. The standard deviation is reduced from 18.57Ω, using DWL lithography, to 12.84Ω, using the hard mask. However, the MR ratio shows a greater dispersion, the standard deviation is doubled. it is also curious to note that despite the samples having the same composition, the average MR ratio and average minimum resistance are different.

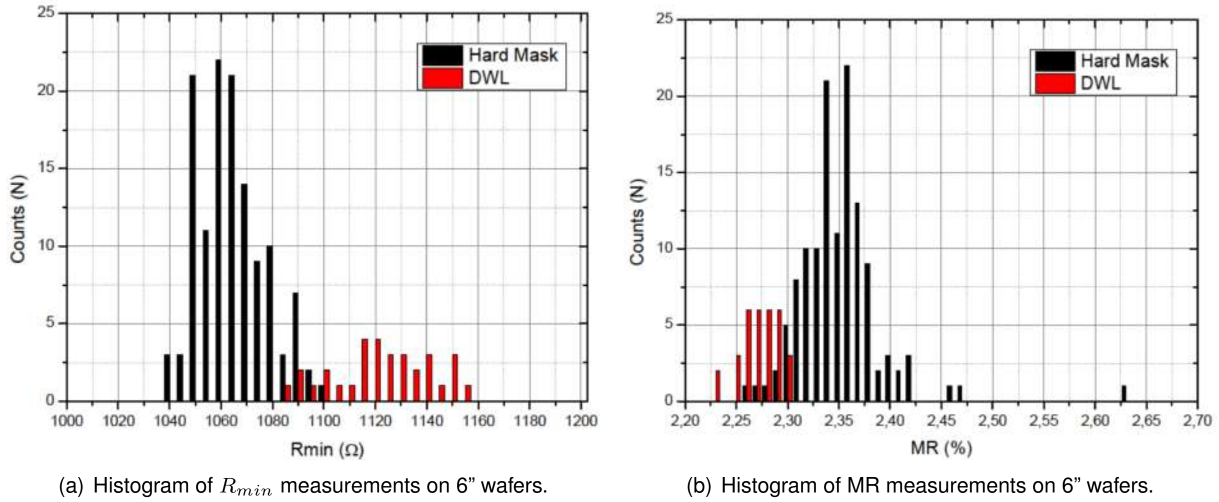

(a) Histogram of R_{min} measurements on 6” wafers.

(b) Histogram of MR measurements on 6” wafers.

Figure 5.17: Histograms of R_{min} and MR measurements on 6” wafers, using two different lithography techniques for the definition of the sensor level.

5.4 Positioning

Since some samples exhibited very similar properties, only three out of the six samples were selected to be tested on the scanner, so as to evidence the effect of these properties more effectively. The Ta(50) was chosen, as it was the baseline stack for testing, and because it has the lowest AMR ratio. Also the sample NiFeCr(50) for a direct comparison with the Ta(50) sample, and lastly the sample Ta(30)+NiFeCr(300), because it had the highest FWHM. Since the coercivity was very similar between the samples, it is not possible to find a correlation between this property and the scanner test results. So, these tests will show the effect of AMR ratio and the FWHM or saturation on the performance of the sensors when applied in positioning systems. This was also, in itself, a test to the scanner system and acquisition board, to ascertain its proper functioning.

In terms of designs, two were used due to the reduced number of samples available. The two designs used are very similar: the meanders are exactly the same, only the electrical contacts are arranged differently.

Each sensor was submitted to several different scans at increasing distance from the magnetic scale. The scans were done over a $6mm$ span with a $10\mu m$ step and the flying heights were $d = 0.2mm$, $d = 0.4mm$, $d = 0.6mm$, $d = 0.8mm$, $d = 1.0mm$, $d = 1.2mm$, $d = 1.4mm$, $d = 1.6mm$, $d = 1.8mm$ and $d = 2.0mm$, measuring at each height the output of both bridges. The sensors were biased with 5V AC. After the measurements, a sinusoidal wave was fit to each set of data, to provide information on the offset (which was later used to correct the signal), the amplitude, period and phase of the signals. In a fully functional positioning system, the offset would be corrected with electronics, however, the purpose here is also to measure the offset, so no further electronics were implemented to correct it. The correction was done after the sinusoidal function fit, by subtracting the offset, and it is then possible to use equation 2.13 to calculate the position of the sensor. Since the step used in the scans was $10\mu m$, this information will be used to evaluate the accuracy of the sensors, by comparing the increment in position with the step used.

By first analysing the polar plots ($Bridge2\,vs\,Bridge1$, with the offsets already corrected; the offset values will be discussed further), it is possible to observe already some valuable information. These plots are shown in figures 5.18, 5.19 and 5.20, for samples Ta(50), NiFeCr(50) and Ta(30)+NiFeCr(300), respectively, for the different flying heights.

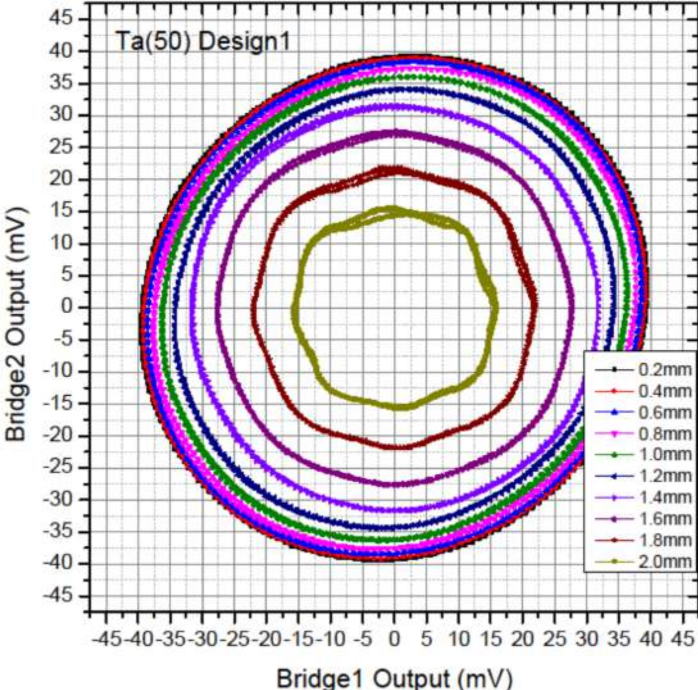

Figure 5.18: Polar plots ($Bridge2\,vs\,Bridge1$) of sample Ta(50) at different flying heights.

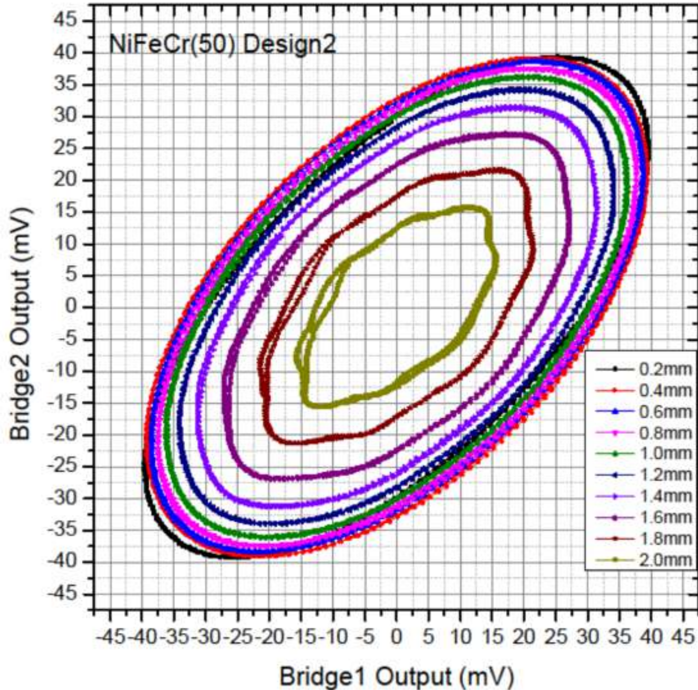

Figure 5.19: Polar plots ($Bridge2\,vs\,Bridge1$) of sample NiFeCr(50) at different flying heights.

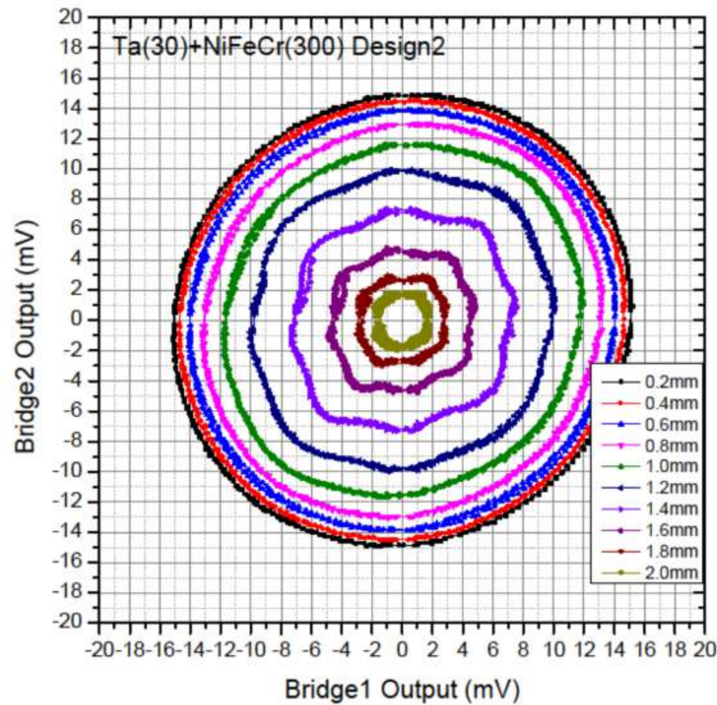

Figure 5.20: Polar plots ($Bridge2\,vs\,Bridge1$) of sample Ta(30)+NiFeCr(300) at different flying heights.

Immediately, from all the plots it is possible to see that with increasing flying height, the amplitude of the bridge outputs decreases. Also noticeable is the fact that after a certain flying height, the polar plot loses its ideal circumference shape. This happens the earliest for sample Ta(30)+NiFeCr(300), evident at a flying height of $d = 1.2mm$, and latest for sample Ta(50), at a flying height of $d = 1.8mm$. There is also clear evidence of phase mismatch in sample NiFeCr(50), which is known to be present if there is an elongation of the circumference in the direction of the $y = x$ or $y = -x$ lines. These results will be explored further, in the following order: Bridge offsets, Bridge mismatch, positioning errors and performance with increasing height.

Bridge Offsets

By removing the 2.5V common mode level, resulting from the 5V bias, it is ensured that the offset of the signals is due to imbalances of the bridges. These offsets can result from the paired sensors having different resistance values, or different magnetic responses. The offsets are expected to be in the order of a few mV. The results regarding the offsets for the three tested samples are shown in figure **??**:

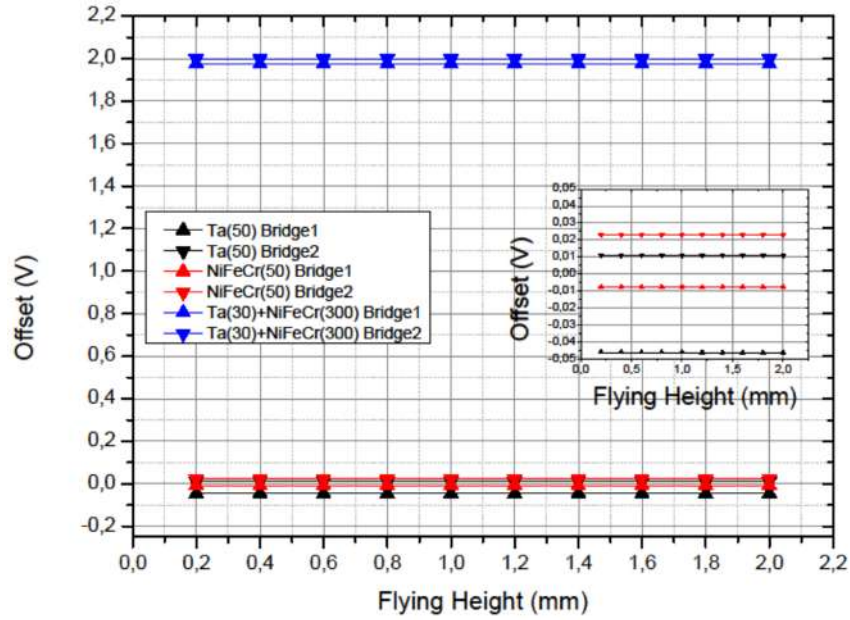

Figure 5.21: Evolution of the offset of both bridges of each device with increasing flying height.

Clearly, sample Ta(30)+NiFeCr(300) exhibits a very abnormal behaviour, with a large offset of almost $2V$. This is a clear indication that something is wrong with the device. The other two samples, Ta(50) and NiFeCr(50), have offsets within more reasonable values, although still high, $\approx -46mV$ and $\approx +11mV$ for sample Ta(50) and $\approx -7mV$ and $\approx +22mV$ for sample Ta(50), for bridges 1 and 2 respectively. To verify the cause of these offsets, the maximum resistance between all terminals was measured (without any external field), using the test pads on the PCB. The resistance measured corresponds to the equivalent resistance shown in figure 5.22:

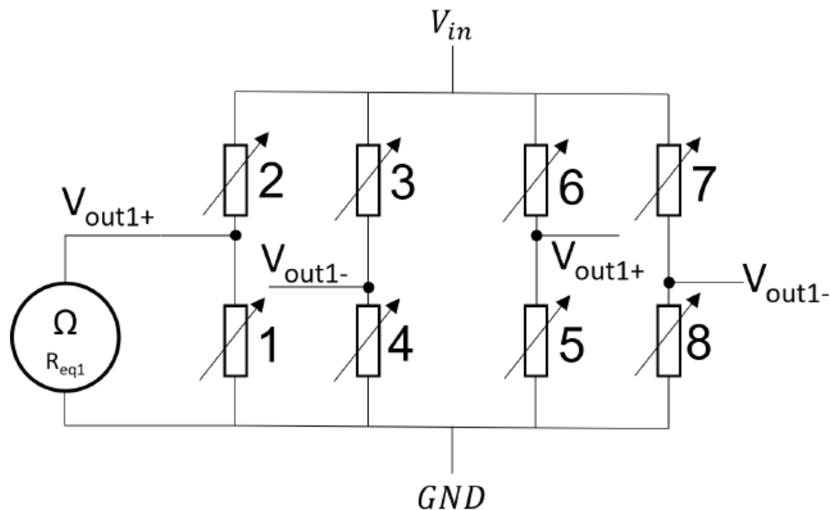

Figure 5.22: Equivalent resistance measured between V_{out1+} and GND. For the other equivalent resistances the procedure is the same, using the appropriate terminals.

The values of the equivalent resistances are shown in table 5.9:

Table 5.9: Equivalent resistance values, for the devices from samples Ta(50), NiFeCr(50), Ta(30)+NiFeCr(300).

Sample	$R_{eq1}(\Omega)$	$R_{eq2}(\Omega)$	$R_{eq3}(\Omega)$	$R_{eq4}(\Omega)$	$R_{eq5}(\Omega)$	$R_{eq6}(\Omega)$	$R_{eq7}(\Omega)$	$R_{eq8}(\Omega)$
Ta(50)	1569	1566	1563	1565	1567	1566	1549	1567
NiFeCr(50)	628	628	1039	1036	630	631	1039	1037
Ta(30) + NiFeCr(300)	2041	1024	767	766	2047	1027	768	766

It becomes clear why sample Ta(30)+NiFeCr(300) exhibits such a large bridge offset, as there is a clear imbalance of the both bridges. Sensors 1 and 5 have a much larger resistance, and are thus not paired with sensors 3 and 7 respectively. Also, it is possible to see one difference between designs: in design 1 (sample Ta(50)) the sensors all have very similar maximum resistances, whilst in design 2 (sample NiFeCr(50)) the sensors have different maximum resistances, but are always paired. So, it is possible to have different resistance values, as long as the pairing is respected, to obtain small offsets. Another important aspect of these measurements is that the offset of the bridges is unaffected by the increasing flying height. This property is intrinsic to the bridge, and thus remains constant. This quantity should also not depend on the stack, only on the resistance imbalance. The variation of the paired resistances could possibly be minimized by the use of Hard Mask Lithography.

Bridge Mismatches

Starting with the phase mismatch, a clear example occurred with sample NiFeCr(50). The phase difference between the two bridges, of the three samples, as a function of the flying height is shown in a plot in figure 5.23:

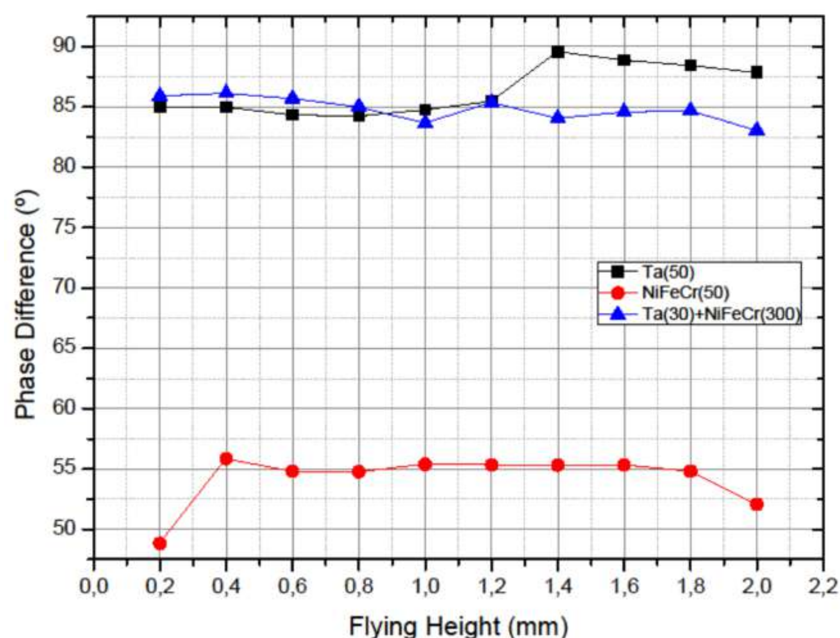

Figure 5.23: Evolution of the phase difference with increasing flying height for the three tested samples.

Samples Ta(50) and Ta(30)+NiFeCr(300) show the values closest to the expected $90°$ phase difference. There is still phase mismatch however, as the phase difference is $\approx 85°$ for both. Sample NiFeCr(50) exhibits the largest phase mismatch, with a phase difference of $\approx 55°$ for the majority of the scans at different heights. The phase difference remains similar throughout the different scans, so it is also unrelated to the flying height, and is again intrinsic to the sensor. The large phase difference in sample NiFeCr(50) could perhaps be explained by the sensors' resistance imbalance. This quantity should also be independent from the stack. The consequence of phase mismatch will be made clear in the position errors.
Now concerning amplitude mismatch, the results are plotted in figure 5.24:

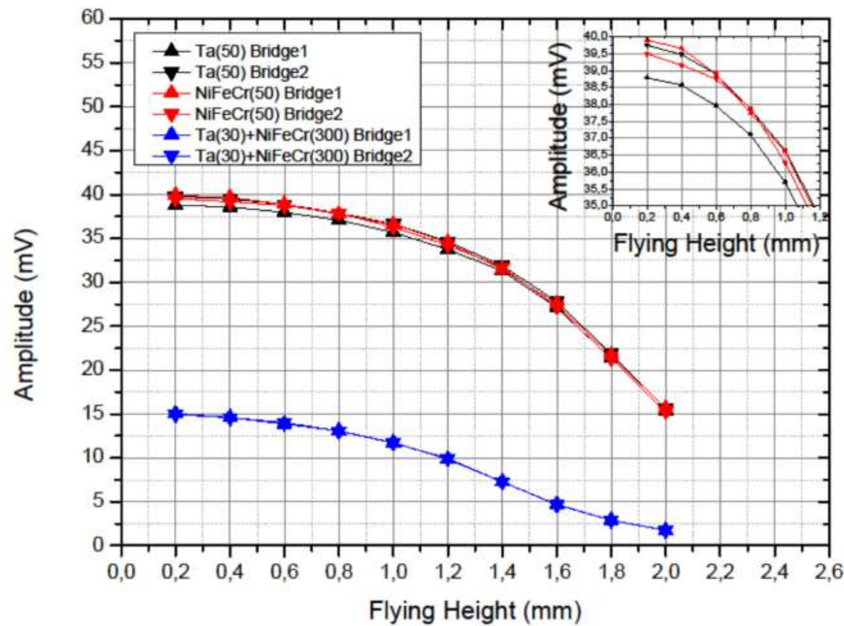

Figure 5.24: Amplitudes of both bridges of the each device, as function of the flying height.

Something that was already visible in the polar plots (figures 5.18, 5.19 and 5.20) is that the amplitude of the bridge outputs decreases with increasing flying height. This behaviour is present in all the three samples. Sample Ta(30)+NiFeCr(300) exhibits the lowest amplitudes, despite having the largest MR of the three samples. Samples Ta(50) and NiFeCr(50) have very similar output amplitudes, despite sample Ta(50) having a lower MR ratio. On this aspect, the results are inconclusive and would require more tests with more samples. The sensors used from sample Ta(30)+NiFeCr(300) appear to have some defect, mainly in sensors $S1$ and $S5$, which with higher resistance that expected have a lower MR ratio, thus producing a lower amplitude.
Also, in the inset in figure 5.24 it is possible to observe that the sample Ta(50) has a slightly larger amplitude mismatch, with a maximum difference of $0.97mV$ at lowest flying height. In all three samples this mismatch seems to decrease slightly with increasing flying height. The absolute values of the amplitude difference (—A_{B1}-A_{B2}—) are plotted in figure 5.25:

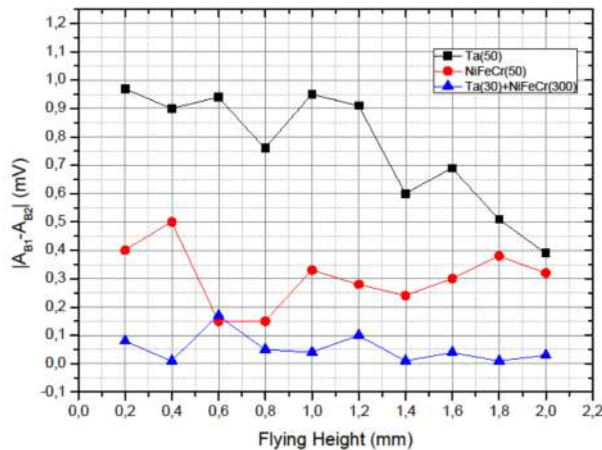

Figure 5.25: Amplitude difference between bridges of the same device, as function of the flying height.

Positioning Error

After correcting the output of the bridges by subtracting the offset, the data was used to calculate the position of the sensor, relative to each bit, using equation 2.13. Since there is no reference position, these values on their own serve little purpose, and since this system is an incremental positioning system, not an absolute positioning system, the performance was evaluated by comparing the increments in position, with the step used. If the devices are accurate, the increment in position should match the $10\mu m$ step used. The error was then computed as well, by subtracting the $10\mu m$ step to the increment value obtained. The results for samples Ta(50) and NiFeCr(50) are shown in figure 5.26, for the first three flying heights, $d = 0.2mm$, $d = 0.4mm$ and $d = 0.6mm$. These two samples were chosen to be examined under the positioning error parameter because they exhibited an amplitude mismatch and a phase mismatch, respectively sample Ta(50) and sample NiFeCr(50). It will be possible to examine the impact of these mismatches in the accuracy.

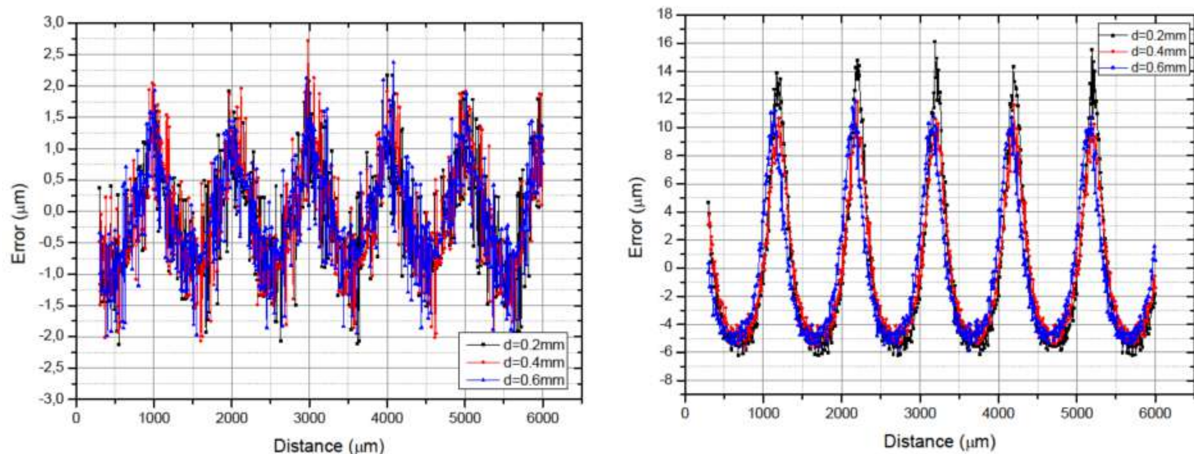

(a) Positioning error using devices from sample Ta50) at the first three flying heights.

(b) Positioning error using devices from sample NiFeCr(50) at the first three flying heights.

Figure 5.26: Positioning error using devices from sample Ta(50) at the first three flying heights, $d = 0.2mm$, $d = 0.4mm$, $d = 0.6mm$.

Starting with the error value, sample the device from sample Ta(50) was the most accurate, with a maximum error of $\approx 2\mu m$, while sample NiFeCr(50) has a maximum error of $-15\mu m$. Another difference is that the positive and negative error are symmetric for sample Ta(50), $\approx \pm 2\mu m$, while for sample NiFeCr(50) this is not the case. The positive error has a maximum of $\approx +15\mu m$ and the negative error a maximum of $\approx -5\mu m$.
With the error values plotted, it is also clear that they have a semblance of periodicity. To evaluate this, a sinusoidal wave was again fitted to the data, to extract the period. This was done for the first three flying heights already mentioned, and the results were averaged and are presented in table 5.10:

Table 5.10: Average values of period, phase and phase difference of the positioning error, for the devices from samples Ta(50) and NiFeCr(50).

	Ta(50)	NiFeCr(50)	Difference
Period	502.58 $\pm$1.75 (μm)	503.30 $\pm$0.85 (μm)	
Phase	-45.18 $\pm$ 2.38 (°)	-16.50 $\pm$ 1.11(°)	28.68 $\pm$ 3.49 (°)

Regarding the period first, the error has a period of approximately half the signal period, so the maximum positive and negative errors occur periodically, twice per period of the bridge outputs. In other words, on one revolution around the polar plot, there will be two general areas, for positive and negative errors each, where the errors are maximized. Figure 5.27 shows the polar plots of samples Ta(50) and NiFeCr(50), at $d = 0.2mm$, with the points where the error is close to the maximum positive error (within 10% to 20% of the maximum value) marked in red, and where it is close to the maximum negative error marked in blue:

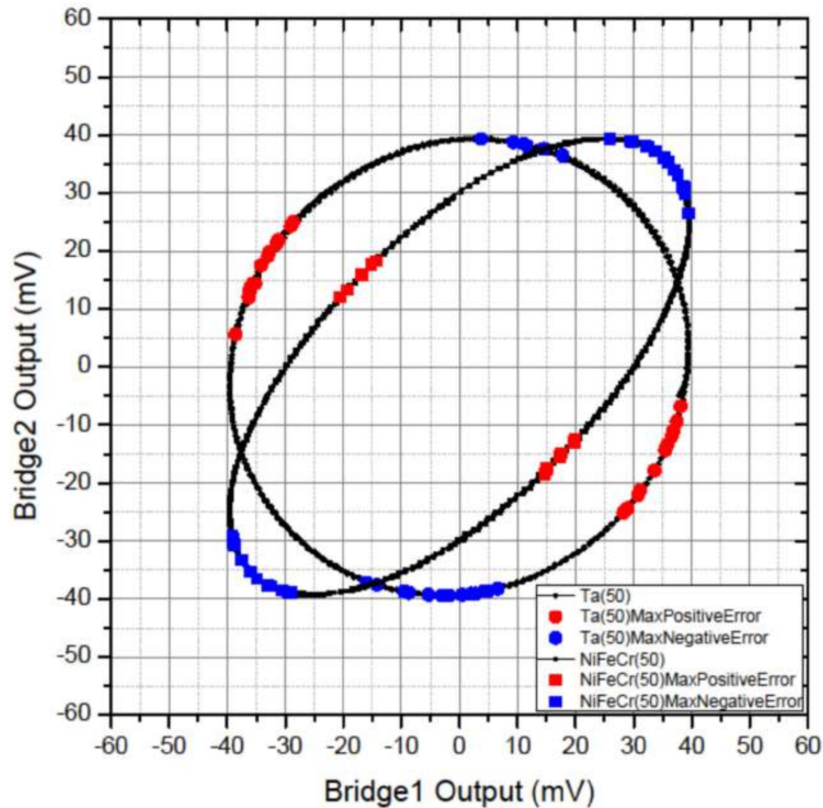

Figure 5.27: Polar plot of measurements with the devices from samples Ta(50) and NiFeCr(50) with maximum positive and negative error zones highlighted.

The amplitude and phase mismatch are clear sources of error, as evidenced by these results. The elongation of the polar plot, from the perfect circumference to an ellipse, leads to an increased error in positioning. Also, it is possible to relate the sign of the error with the shape of the ellipse: points near the major axis have a default error and points near the minor axis have an excess error. In the case of the device from sample NiFeCr(50) this is very pronounced, since the phase shift is very large. In the device from sample Ta(50) there is a slight amplitude mismatch, higher amplitude on $Bridge2$, and the phase difference of the two bridges is not exactly $90°$, so the circumference is slightly elongated in a direction near the y axis.

Also worth noting, and finalizing this correlation between positioning errors and bridge mismatch, is the phase difference between sets of error, already presented in table 5.10. The error phase difference, $28.81 \pm 3.07°$, corresponds quite closely to the difference between the phases of both samples, within the error margin, averaging over the same lying heights. For sample Ta(50), the bridge outputs have an average phase difference of $84.78 \pm 0.26°$, and for sample NiFeCr(50) a phase difference of $53.15 \pm 0.19°$, and the difference between these two values is $31.63 \pm 0.45°$, approximately the same as the phase difference between the error of both samples. So, everything regarding the periodicity and phase of the signals and errors is undoubtedly correlated.

Lastly, a plot of the calculated position, referent to one bit (from $0\mu m$ to $2000\mu m$) at flying height $d = 0.2mm$ is presented in figure 5.28, as an example:

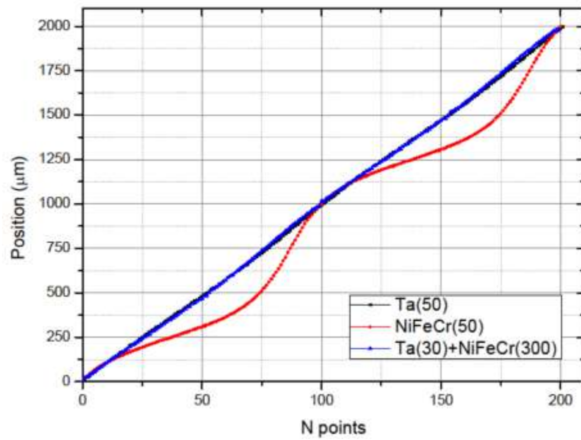

(a) Position calculated using equation 2.13 and the bridges' outputs, for the three tested samples, at $d = 0.2mm$.

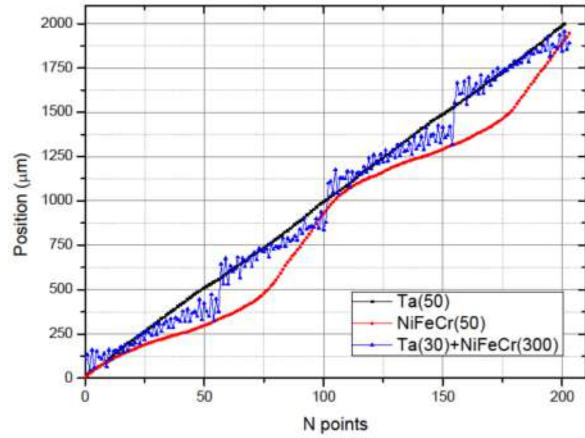

(b) Position calculated using equation 2.13 and the bridges' outputs, for the three tested samples, at $d = 2.0mm$.

Figure 5.28: Position calculated using equation 2.13 and the bridges' outputs, for the three tested samples, at flying heights $d = 0.2mm$ (a) and $d = 0.2mm$ (b).

Samples Ta(50) and Ta(30)+NiFeCr(300) produced an almost linear output at flying height $d = 0.2mm$, which is intended to be linear, while sample NiFeCr(50) produced an output far from linear. However, it is been established that the issues with the device from sample NiFeCr(50) are not stack related, but due to some defect in the device that lead to the phase mismatch of the bridge outputs. When the devices are moved further away from the scale, at flying height $d = 2.0mm$, it is possible to observe that the output of the device from sample Ta(30)+NiFeCr(300) is now deteriorated drastically, and the position is no longer recoverable as a linear output. Samples Ta(50) and NiFeCr(50) on the other hand, practically maintain the same output, albeit with increased error.

Performance vs Flying Height

Previously it was evidenced that the flying height has no consequence on the bridge offsets and on the phase difference between the bridges. These are intrinsic properties of the devices. However, it was also evidenced that for all samples the amplitude dropped with increasing height, as well a signal-shape error started to appear in the polar plots. This is where some conclusion can be drawn regarding the material stack. By normalizing the amplitudes, it is possible to compare their evolution as function of flying height, directly across the three samples. The results are plotted in figure 5.29:

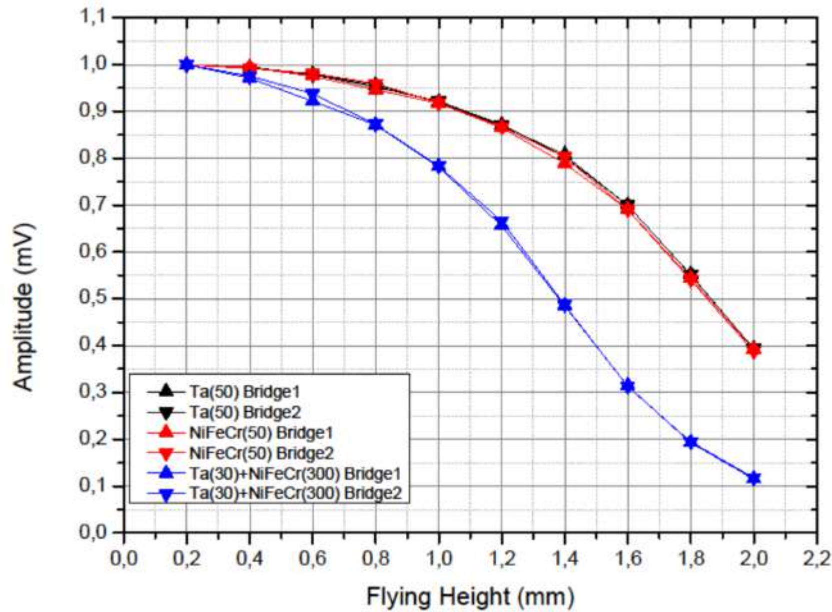

Figure 5.29: Evolution of the normalized amplitude with increasing flying height.

It is visible that the amplitude of the bridges from the device of sample Ta(30)+NiFeCr(300) drops much faster than that of the other samples. This is stack related. Since Ta(30)+NiFeCr(300) displayed the highest FWHM of the transfer curve, it requires a stronger magnetic field to saturate. The AMR sensors in this particular application are required to saturate, otherwise they do not function correctly. And such is the case with the Ta(30)+NiFeCr(300): as the device is moved further from the scale, the amplitude drops significantly faster when compared with the other two samples. It was also possible to see a signal-shape error appear in the polar plots of sample Ta(30)+NiFeCr(300) much sooner than for the other two samples. So, the saturation of the device, quantified here with the FWHM, is directly related with its performance at increasing flying height: the lower the saturation, the further away from the scale it can function properly.

Regarding the other properties of the signals, period, phase and offset, no changes were verified when increasing the flying height. They are intrinsic to the geometry and bridge balance.

Plotting the maximum positive and negative positioning errors shows that for sample Ta(30)+NiFeCr(300) there is a clear dependence of the error with the flying height: the further away from the scale, the higher the error is. The devices from the other two samples have maximum errors approximately constant throughout the different flying heights, nonetheless it shows a tendency to increase towards the largest flying heights, $d = 1.8mm$ and $2.0mm$, as can be seen on the inset plots in figure 5.30, as well as the remainder of the information on the main plots:

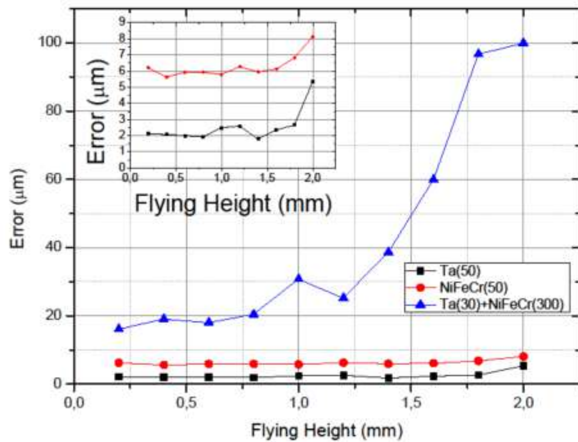

(a) Evolution of the maximum positive positioning error with increasing flying height.

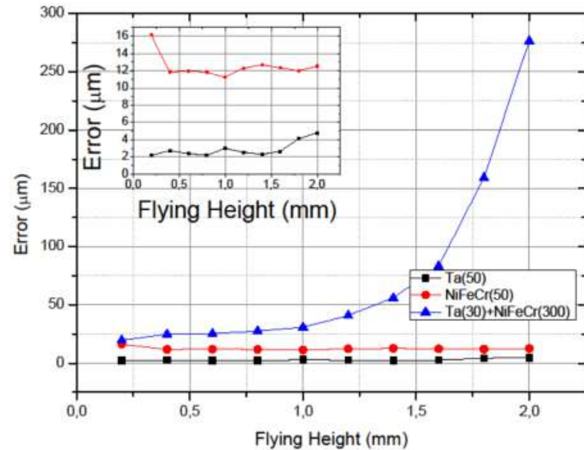

(b) Evolution of the maximum negative positioning error with increasing flying height.

Figure 5.30: Evolution of the maximum positive and negative positioning errors with increasing flying height.

The trend of increasing error with increasing flying height was observed in all cases, except for the maximum negative error in the device from sample NiFeCr(50), which actually had the largest error closest to the scale. More tests would be required to verify if this is an anomaly, or it would be verified consistently. The plotted values being the maximum errors, they are sometimes larger than the actual step used, indicating that the flaws found, the amplitude and phase mismatches, are critical, and must be addressed and minimized, so that the error is in turn also minimized.

Chapter 6

Conclusions

6.1 Achievements

With the analysis of the test samples with x-ray diffractometry it is possible to conclude that the magnetic annealing step is crucial when using NiFeCr as the buffer material. In these samples, a doubling of the grain size can be observed after one hour of annealing at 350°C. The process of annealing also shows improvements in the magnetic response, as a significant improvement in the MR ratio was also observed in these samples. The largest improvement was observed in the sample NiFeCr(50), from 1.89% to 2.74%. Overall, the MR ratio seems to increase with buffer thickness as well, as the highest MR ratio measured was 3.04% in sample NiFeCr(300). Resistance is in general lowered by annealing in NiFeCr samples, and as expected it also decreases with increasing total thickness. However, in Ta samples the annealing process has the opposite response: MR ratio decrease, while resistance increases.
In all samples, annealing provided improvements in the coercivity, regardless of the total thickness. Whilst the saturation seems to not be influenced greatly by annealing, it seems to increase with increasing layer thickness.
So, annealing is favourable for stacks with a NiFeCr buffer, showing improvements both in MR ratio and coercivity. On stacks with Ta buffer, the MR decreases with annealing, but the coercivity is improved still. The coercivity shows no obvious correlation with the thickness of the buffer layer, but the saturation does, increasing with increasing total thickness.
With the comparison between the two lithography methods, DWL and hard mask, it is possible to discern a slight improvement in the dispersion of values of resistance, from a 18.57Ω standard deviation, to 12.84Ω. In theory, if the DWL lithography occurs with the same parameters (focus, energy) across the whole wafer, it should be as uniform as the hard mask lithography, which is also only uniform if the hard mask is equally distant from the wafer at every point. However, going forward into a production stage, this dispersion should still be lowered, so the process still needs to be improved.
The tests done with the scanner show that the setup, with the required adaptions to these sensors having been made, is suitable for detecting issues with the devices. It was possible to measure effectively the offsets of the bridges' outputs, by removing the common mode level, as well as amplitude and phase

mismatches. The positioning error was also evaluated, and the source of this error was successfully identified, as a relationship between mismatches and the positioning error was able to be drawn, from the tests on devices from samples Ta(50) and NiFeCr(50).

In conclusion, with this dissertation it was possible to identify NiFeCr as a suitable candidate for the material of the buffer layer of AMR sensors, showing promising results in terms of magnetic properties. To evaluate the performance of the devices using different stacks, in order to draw conclusions as to which stack is best, a larger number of tests is required. Devices can be defective for reasons unrelated to the stack, which is the present case, thus masking whatever conclusions could be drawn as for a relationship between the performance on the scanner and the magnetic properties of the stack. Nonetheless, a setup for these tests is now in place, by adaption of a previous setup to the AMR sensors studied during this dissertation. With the tests done regarding scanning it was possible to ensure that the setup is appropriate and running successfully, as it still provided valuable information regarding the devices' performance, and it can be used to identify issues such as offset and bridge mismatches.

6.2 Future Work

More information can be collected regarding the annealing step. The only annealing temperature used was 350°C, but there is no guarantee the behaviour observed in the tested samples would remain the same when annealing at different temperatures. It would be advantageous to find if there is an optimal annealing temperature, and not just duration at a single temperature. Also, a wider range of buffer thicknesses can be tested using NiFeCr, to obtain a more complete profile on the dependence of thickness of certain properties.

Improvements can also be done to the scanner setup, to have better resolution. Since these sensors are expected to work with great accuracy, in the order of the μm, and very low hysteresis as well, of just a few μm, the current setup does not possess enough resolution to measure these quantities. Also, an optical encoder can be added as a reference, instead of trusting the values dictated by the scanner stage controller software. The mechanical motion of the stage controller can cause loss of accuracy, and whilst the user can choose a given scanning step, there is no guarantee that the actual step with which the devices move will be that accurate and precise. With a reference encoder, that uncertainty would be resolved, as the devices being tested should match the optical encoder, and the uncertainty of the control software would be eliminated.

With the testing setup now in place and properly working, what remains to do is further tests, with more devices from the same sample, and start to evaluate the effect of the stack on the several parameters that dictate the devices' performance for linear positioning.

Further characterization can be made, regarding other important properties such as noise and thermal stability, for example, to provide a more complete picture on the quality of the sensors.

Bibliography

[1] D. Collins. How do magnetic linear encoders differ from optical versions?, Jul 2018. URL `https://www.linearmotiontips.com/how-do-magnetic-linear-encoders-differ-from-optical-versions/`.

[2] J. M. D. Coey. *Magnetism and Magnetic Materials*. Cambridge University Press, 2010. doi: 10.1017/CBO9780511845000.

[3] M. Hott, P. A. Hoeher, and S. F. Reinecke. Magnetic communication using high-sensitivity magnetic field detectors. *Sensors*, 19(15):3415, 2019.

[4] Q. Huang, A. H. Khawaja, Y. Chen, and J. Li. *2 State of the Art Magnetoresistance Based Magnetic Field Measurement Technologies*. John Wiley & Sons Ltd., 2020.

[5] T. McGuire and R. Potter. Anisotropic magnetoresistance in ferromagnetic 3d alloys. *IEEE Transactions on Magnetics*, 11(4):1018–1038, 1975.

[6] T. Costa. Advanced magnetoresistive sensors for industrial applications. Master's thesis, Instituto Superior Técnico, 11 2017.

[7] Magnetic encoders rls. URL `https://www.rls.si/eng/`.

[8] Magnetic encoders balluff. URL `https://www.balluff.com/`.

[9] Magnetic linear encoders - magnetic tape for linear measurement applications. URL `http://www.electronicaems.com/Magnetic-Tape.php`.

[10] R. C. OHandley. *Modern magnetic materials: principles and applications*. Wiley, 2000.

[11] K. M. Krishnan. *Fundamentals and Applications of Magnetic Materials*. Oxford University Press, 2016.

[12] G. A. Passos. *Principles of nanomagnetism*. Springer, 2018.

[13] W. Thomson. Xix. on the electro-dynamic qualities of metals:—effects of magnetization on the electric conductivity of nickel and of iron. *Proceedings of the Royal Society of London*, (8):546–550, 1857.

[14] A. V. Silva, D. C. Leitao, J. Valadeiro, J. Amaral, P. P. Freitas, and S. Cardoso. Linearization strategies for high sensitivity magnetoresistive sensors. *The European Physical Journal Applied Physics*, 72(1):10601, 2015.

[15] L. Jogschies, D. Klaas, R. Kruppe, J. Rittinger, P. Taptimthong, A. Wienecke, L. Rissing, and M. C. Wurz. Recent developments of magnetoresistive sensors for industrial applications. *Sensors*, 15 (11):28665–28689, 2015.

[16] H. N. Bertram. *Theory of magnetic recording*. Cambridge University Press, 1994.

[17] L. Quynh, B. Tu, N. Thuy, D. Viet, N. Duc, A. Phung, and D. H. Giang. Meander anisotropic magnetoresistance bridge geomagnetic sensors. *Journal of Science: Advanced Materials and Devices*, 4(2):327–332, 2019. doi: 10.1016/j.jsamd.2019.04.007.

[18] R. Moghimi. Bridge-type sensor measurements are enhanced by autozeroed instrumentation amplifiers with digitally programmable gain and output offset. 2004.

[19] Wheatstone bridge circuit: Strain gauge, Dec 2020. URL `https://www.hbm.com/en/7163/wheatstone-bridge-circuit/`.

[20] A. Voss, A. Meisenberg, and A. Bartos. Sacle based magnetoresistive sensor systems. *TE Connectivity Sensor Solutions*.

[21] S. Cardoso, D. C. Leitão, and V. Silvério. Lecture notes and slides on micro and nanofabrication techniques, ist course, 2019.

[22] A. S. Sedra and K. C. Smith. *Microelectronic circuits*. Oxford University Press, sixth edition.

[23] D. Gurauskis, A. Kilikevičius, and S. Borodinas. Experimental investigation of linear encoder's subdivisional errors under different scanning speeds. *Applied Sciences*, 10(5):1766, 2020. doi: 10.3390/app10051766.

Appendix A

Process Runsheet

A.1 Runsheet

Responsible:____________________

Process start: ____ /_____ /________ Process Finish: ____ /_____ /________

Die size (approx.)	X : 13000 ; Y : 13000 (µm)
Map	AMSION_C
Designs	7
L1	[100, 100] +
L2	[100, 250] +
L3	[100, 400] +
L4	[100, 550] +

Step 1: AMR Stack Deposition ____ /_____ /________

Operator:_________________

Machine: N3000

Materials:

A: Si/SiO_2 500 / Ta 50 / NiFe 400 / Ta 50 (Å)

B: Si/SiO_2 500 / NiFeCr 50 / NiFe 400 / NiFeCr 50 (Å)

C: Si/SiO_2 500 / NiFeCr 100 / NiFe 400 / NiFeCr 50 (Å)

D: Si/SiO_2 500 / NiFeCr 150 / NiFe 300 / NiFeCr 50 (Å)

Conditions:

	Power (W)	V+ (V)	I+ (mA)	V- (V)	I- (mA)	Ar Flux (sccm)	Rotation (rpm)	W.P. (Torr)
Set Point								
Read Values								

Optical inspection | Comments:

Step 2: First Lithography: Sensor ____ /_____

Operator:_________________ Machine: DWL

1.1 Coat 1.5µm Photoresist (recipe 6/2)
1.2 Lithography

Map: AMSION

Mask (inverted):____________

Layer name (autocad):______________

Energy:________ Focus:_________ Power:__________

Total time:_____________

Die Dimensions: [X : 13000 ; Y : 13000] (µm)

1.3 Develop (recipe 6/2)

Optical Inspection | Comments:

Step 3: Sensor Definition by Ion Beam Milling (IBM) ____ /_____ /________

Operator:________________ Machine: N3000

Total stack thickness (to be etched):________

Etch rate: Ta:________ | “Normal metals”:___________

$Time_{max}$:________s @ pan =_______

Batch:_________

Wafer:________

Steps:_______

Base Pressure:__________________

	Power (W)	V+ (V)	I+ (mA)	V- (V)	I- (mA)	Ar Flux (sccm)	Rotation (rpm)	W.P. (Torr)
Set Point								
Read Values								

Neutralizer: 0mA / 3sccm

Optical Inspection | Comments:

Runsheet – 1 inch stack optimization Run #__

Step 4: Resist Strip ____ /_____ /________

Operator:____________________ Machine: Wetbench

Conditions: Microtrip + Ultrasound bath @ 65ºC

Total time:___________

Inspection | Comments:

Step 5: Passivation – SiO_2 Deposition ____ /_____ /________

Operator:____________________ Machine: Oxford

Conditions:__________________

Base Pressure:___________________

	Total time (min)	Gas Flow (sccm)			Temperature (ºC)	Source Power (W)
		N_2O	SiH_4	N_2		
Set Point						
Read Values						

Inspection | Comments:

Step 6: Second Lithography - Vias ____/_____/________

Operator:_________________ Machine: DWL

1.1 Coat 1.5µm Photoresist (recipe 6/2)
1.2 Lithography

Map: AMSION

Mask (non-inverted):____________

Layer name (autocad):______________

Energy:________ Focus:_________ Power:__________

Total time:_____________

Die Dimensions: [X : 13000 ; Y : 13000] (µm)

Alignment mark: L1: [100, 100] +

1.3 Develop (recipe 6/2)

Optical Inspection | Comments:

Step 7: Vias opening by RIE ____/_____/________

Operator:_________________ Machine: LAM

Recipe: Low_power_no_O2_3steps

Total time:______________

Pressure	RF Power	Gap	He (clamp)	T_{bottom}	T_{top}	Ar(sccm)	CF_4 (sccm)	Etch rate: SiO_2

Inspections | Comments:

Step 8: Resist Strip ____/_____/________

Operator:___________________ Machine: Wetbench

Conditions: Microtrip + Ultrasound bath @ 65ºC

Total time:___________

Inspection | Comments:

Step 9: Third Lithography – Contacts definition ____/_____/________

Operator:_________________ Machine: DWL

1.1 Coat 1.5µm Photoresist (recipe 6/2)
1.1.1 Pre-Development 20s
1.2 Lithography

Map: AMSION

Mask (non-inverted):____________

Layer name (autocad):______________

Energy:________ Focus:_________ Power:__________

Total time:_____________

Die Dimensions: [X : 13000 ; Y : 13000] (µm)

Alignment mark: L1: [100, 250] +

1.3 Develop (recipe 6/2)

Optical Inspection | Comments:

Step 10: Metallization (Contact Deposition) ____/_____/________

Operator:_________________ Machine: N7000

Sequence: Metallization Run #__

- Mod.2 f.3: 60s etch 40w/60w
- Mod.4 f.1: 2000 AlSiCu 2kW (x3)
- Mod.3 f.19: 150Å TiW(N_2)

Module Function		Time (s)	Substrate Table			Plasma Source		Target DC			Ar Flux (sccm)	N2 Flux (sccm)	Pressure (mTorr)
			RF Forward (W)	RF Reflected (W)	DC Bias (V)	RF Forward (W)	RF Reflected (W)	Power (kW)	Voltage (V)	Current (A)			
Mod.2	Set Point		40	-	-	60	-	-	-	-	50	-	3
	Read Values							-	-	-		-	
Mod.4	Set Point		-	-	-	-	-	2	-	-	50	-	3
	Read Values		-	-	-	-	-					-	
Mod.3	Set Point		-	-	-	-	-	0.5	-	-	50	10	3
	Read Values		-	-	-	-	-						

Inspection | Comments:

Step 11: Metal Lift-Off ____/_____/________

Operator:___________________ Machine: Wetbench

Conditions: Microtrip + Ultrasound bath @ 65ºC

Total time:___________

Inspection | Comments:

Step 12: Passivation – SiO_2 Deposition ____/_____/________

Operator:___________________ Machine: Oxford

Conditions:_________________

Base Pressure:__________________

	Total time (min)	Gas Flow (sccm)			Temperature (ºC)	Source Power (W)
		N_2O	SiH_4	N_2		
Set Point						
Read Values						

Inspection | Comments:

Step 13: Fourth Lithography – Pads Opening ____/_____/________

Operator:_________________ Machine: DWL

1.1 Coat 1.5µm Photoresist (recipe 6/2)
1.2 Lithography

Map: AMSION

Mask (non-inverted):____________

Layer name (autocad):______________

Energy:________ Focus:_________ Power:__________

Total time:_____________

Die Dimensions: [X : 13000 ; Y : 13000] (µm)

Alignment mark: L1: [100, 100] +

1.3 Develop (recipe 6/2)

Optical Inspection | Comments:

Step 14: Pads Opening by RIE	____ /_____ /________

Operator:_________________ Machine: LAM

Recipe: Low_power_no_O2_3steps

Total time:______________

Pressure	RF Power	Gap	He (clamp)	T_{bottom}	T_{top}	Ar(sccm)	CF_4 (sccm)	Etch rate: SiO_2

Inspections | Comments:

Step 15: Resist Strip	____ /_____ /________

Operator:___________________ Machine: Wetbench

Conditions: Microtrip + Ultrasound bath @ 65ºC

Total time:___________

Inspection | Comments:

Step 16: Magnetic Annealing	____ /_____ /________

Operator:___________________ Machine: Tube Annealing

Conditions: 2 hours @ 350ºC + Cooling in Magnetic Field 1T

Inspection | Comments:

Appendix B

Acquisition Board

B.1 PCB and switch/jumper combination table

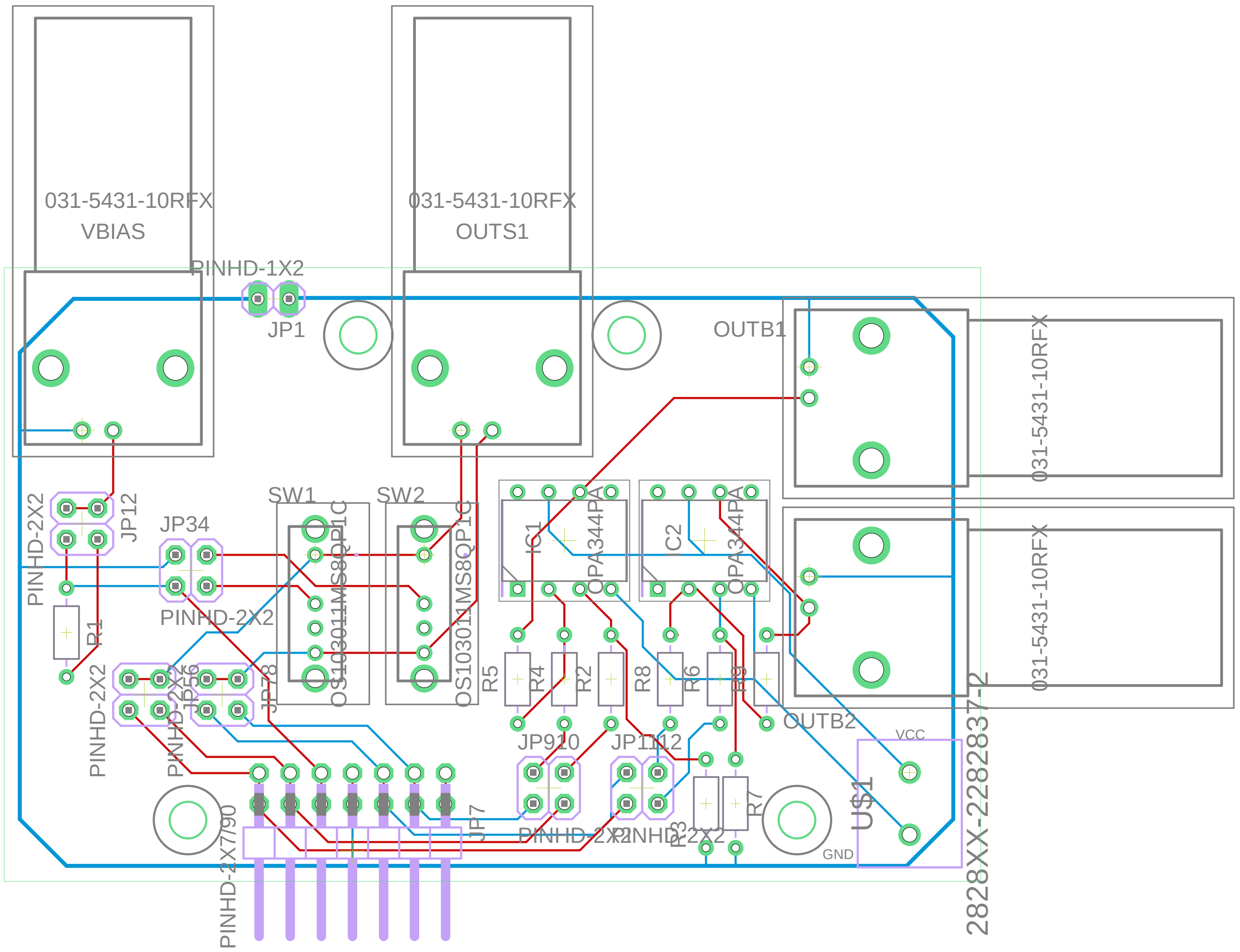

03-08-2021 09:45 f=1.70 C:\Users\brite\AppData\Local\Temp\Neutron\ElectronFileOutput\8556\brd-d69d407f-a831-416c-bf02-9

	In		Out		J1	J2	J3	J4	J5	J6	J7	J8	J9	J10	J11	J12	SW1	SW2
S1	VB	GND	PSIN	GND		**x**	**x**	**x**	**x**								**m**	**b**
S2	VB	GND	VB	PSIN		**x**	**x**	**x**	**x**								**b**	**m**
S3	VB	GND	VB	NSIN		**x**	**x**	**x**			**x**						**t**	**m**
S4	VB	GND	NSIN	GND		**x**	**x**	**x**			**x**						**m**	**t**
S5	VB	GND	PCOS	GND		**x**	**x**	**x**		**x**							**m**	**b**
S6	VB	GND	VB	PCOS		**x**	**x**	**x**		**x**							**b**	**m**
S7	VB	GND	VB	NCOS		**x**	**x**	**x**				**x**					**t**	**m**
S8	VB	GND	NCOS	GND		**x**	**x**	**x**				**x**					**m**	**t**
Bridge1	VB	GND	PSIN	NSIN	**x**								**x**	**x**	**x**	**x**	**m**	**m**
Brdge2	VB	GND	PCOS	NCOS	**x**								**x**	**x**	**x**	**x**	**m**	**m**

SW1, SW2 - SP3T sliding switches:
t - top, m - middle, b - bottom